Load distribution of CLT under in-plane concentrated compression loading

by

Hossein Farboodi

A thesis submitted in partial fulfillment of the requirements for the degree of

Master of Science

in

STRUCTURAL ENGINEERING

Department of Civil and Environmental Engineering

University of Alberta

Abstract

CLT panels are widely used in mid- and high-rise timber building structures, but the application of in-plane compression loads to its edges presents a significant challenge. The Canadian Standard Association (CSA O86) assumes that the load is uniformly distributed across the entire panel, but there is no guidance for cases where the load is concentrated on a small panel section, such as a CLT wall. As a result, the loads tend to dissipate as they move towards the underlying supporting structure, leading to lower stress levels than those experienced at the contact surface. Despite the limited number of studies on the in-plane load spread angle for CLT, no appropriate design procedures are currently available. This study aims to investigate the load distribution behaviour of CLT panels under in-plane compression loading and develop a reliable model to estimate the load spread angle in CLT structures.

After validating the finite element models simulated by ABAQUS software through 18 laboratory tests and the digital image correlation (DIC) method, the project examined the load spread angle of CLT panels under in-plane concentrated compressive loads. The study investigated this angle based on three parameters: the aspect ratio of CLT, the loading area width to panel width ratio, and the transverse layer percentage under two load application scenarios: the load applied at the middle and the edge of the CLT panel.

The results indicate that the transverse layer percentage is the most influential factor affecting the load spread angle. Increasing this parameter from 13% to 50% resulted in the angle increasing from 10° to 18° for an aspect ratio of 0.59, 12° to 17° for an aspect ratio of 0.88, and 12° to 14° for an aspect ratio of 1.25. Moreover, this study recommends two empirical load spread angle and K-factor equations for each loading case through multiple regression analyses to predict the load

spread angle and the maximum stress value of CLT panels under in-plane concentrated compressive loads.

Acknowledgement

I want to express my deepest gratitude to the exceptional individuals whose unwavering support and invaluable contributions have made this thesis possible.

I would like to express my sincere gratitude to my supervisor, Dr. Ying Hei Chui, for his invaluable guidance, constant support, and continuous encouragement throughout my thesis journey. His insights, expertise, and dedication have shaped my research and enhanced my academic abilities.

I want to acknowledge and thank my committee examiners, Dr. Hossein Daneshvar and Dr. Qipei Mei, for agreeing to examine my thesis.

I also extend my heartfelt appreciation to the previous ARTS group's Postdoctoral researcher, Jan Niederwestberg, for his insightful comments, constructive feedback, and valuable suggestions.

I am grateful to the University of Alberta structural lab technicians Greg Miller and Cameron West for providing test equipment and assistance in conducting my laboratory tests.

Finally, I am deeply indebted to my loving family for their unwavering support, understanding, and patience. In addition, I am grateful to my dear friends, Fardad Mokhtari, Reza Mousapour, and Sara Khademi, and Rouzbeh Akbari for their invaluable suggestions, constant support, and kind words, which have been a great source of motivation and focus throughout my academic journey.

Thank you all for your invaluable contributions and unwavering support.

Table of Contents

Abstract ii

Acknowledgement iv

List of Tables viii

List of Figures ix

Chapter 1: Introduction 1

1.1 Background 1

1.2 Research objectives 5

1.3 Thesis structure 7

Chapter 2: Literature Review 9

2.1 CLT Background 9

2.2 Compression perpendicular to grain and bearing capacity 11

2.3 Behaviour of CLT panel under in-plane uniform compressive load 15

2.4 Behaviour of CLT panel under in-plane compressive concentrated loading 16

Chapter 3: In -plane compression test of CLT panel 20

3.1 Introduction 20

3.2 Compression Test 20

3.2.1 Materials 20

3.2.2 Test set-up 21

3.2.3 Test Procedure 25

3.3 Test Results 26
3.3.1 Failure Modes 31
Chapter 4: Numerical Simulation 34
4.1 Introduction 34
4.2 FE model development 34
4.2.1 Selection of element types 34
4.2.2 Material property of components 36
4.2.3 Interaction and constraints 38
4.2.4 Loading and boundary conditions 38
4.2.5 Meshing 40
4.3 Validation of FE model 42
Chapter 5: Parametric Study 50
5.1 Introduction 50
5.2 Studied parameters 50
5.2.1 Ratio of loading area width to CLT panel width (a/w) 50
5.2.2 Aspect ratio of CLT panel (h/w) 51
5.2.3 Percentage of transverse layers 51
5.3 Load spread angle and effective length calculation 52
5.4 Results and Discussion 54
5.4.1 Load spread angle 54

5.4.1.1 Influence of the ratio of load area width to the width of the CLT panel 54

5.4.1.2 Influence of the aspect ratio of CLT panel 56

5.4.1.3 Influence of percentage of transverse layers 58

5.4.2 Derivation of empirical equations 60

5.4.2.1 Category 1 - load applied in the middle of CLT panel 63

5.4.2.2 Category 2 - load application at the edge of CLT panel 65

5.4.3 Maximum compression stress analysis 68

Chapter 6: Conclusion and Recommendations 72

6.1 Summary 72

6.2 Conclusions 72

6.3 Recommendations for future works 73

6.4 Highlights for the original contribution of this project 74

Bibliography 75

Appendix A 79

Appendix B 93

Appendix C 101

List of Tables

Table 3.1. Details of CLT specimens..... 21

Table 3.2. Compression Test Results..... 27

Table 4.1. Material properties of CLT lumber..... 37

Table 5.1. Model matrix and the load spread angle results for variation in a/w..... 55

Table 5.2. Model matrix and the load spread angle results for variation of h/w 57

Table 5.3. Model matrix and the load spread angle results for variation of transverse layer percentage 59

Table 5.4. Parameter study matrix to drive the equations..... 60

Table 5.5. Multivariate logistic regression results for category 1..... 64

Table 5.6. Multivariate logistic regression results for category 2..... 66

List of Figures

Figure 1.1. Load spread angle 2

Figure 1.2. Load spread angle (a) steel component (gusset plate)-adapted from (Wang et al. 2023) (b) load spreading from the center of the load downward to a one-way slab; top view of slab-adapted from (Lantsoght et al. 2015) 3

Figure 1.3. Example of CLT panels under in-plane compression applied to the edge of the panel 4

Figure 2.1. A typical CLT layup (Buck et al. 2016) 9

Figure 2.2. “Slip-lines” determining the direction of the main stresses (Van der Put 2008)..... 12

Figure 2.3. Stress distribution of compressive locally loaded for timber beams perpendicular to the grain - adapted from (Leijten et al. 2012) 13

Figure 2.4. The comparison of the load spread angle based on FE modelling and test results (Gräfe et al.2018) 17

Figure 2.5. Stress distribution within the width of in-plane partial loading of CLT panel (Wu et al. 2022) 18

Figure 3.1. Test Setup – schematic 22

Figure 3.2. Actual Test Setup-Front (Left)-Back (Right) 23

Figure3.3. Stress contour in lower steel plate obtained from FE Analysis 24

Figure 3.4. Type A specimens and load-displacement curves 28

Figure 3.5. Type B specimens and load-displacement curve 28

Figure 3.6. Type C specimens and load-displacement curve 30

Figure 3.7. Type CH specimens and load-displacement curve 30

Figure 3.8. Defects on CLT panels before testing: (a) split, (b) knot and check, (c) transverse lumber wane 31

Figure 3.9. Some examples of compression failure modes 32
Figure 4.1. 8-node brick element schematic, C3D8R 35
Figure 4.2. Axes of growth rings and grain direction in wood (Wood Handbook (2021)) 37
Figure 4.3. Structure of FE models with loading and boundary conditions 39
Figure 4.4. Mesh size sensitivity 40
Figure 4.5. FE model with uniform mesh size of 10 mm 41
Figure 4.6. The location of the reference line selected in DIC and FE models to obtain the uniform distribution 43
Figure 4.7. Displacement contour plots and displacement graph from compression test at 80% of failure load for specimen A-3- DIC (left), FE modelling (right) 44
Figure 4.8. Normal strain contour plots and normal strain graph in the y direction from compression test at 80% of failure load for specimen A-3- DIC (left), FE modelling (right) 44
Figure 4.9. DIC, Test and FE modelling results for specimen A-3 until failure 45
Figure 4.10. Displacement contour plots and displacement graph from compression test at 80% of failure load for specimen B-5- DIC (left), FE modelling (right) 46
Figure 4.11. Normal strain contour plots and normal strain graph in the y direction from compression test at 80% of failure load for specimen B-5- DIC (left), FE modelling (right) 46
Figure 4.12. DIC, Test, and FE modelling results for specimen B-5 in the failure mode 47
Figure 4.13. The load distribution results of FE modelling and testing at failure. 49
Figure 5.1. Schematic of three selected parameters (a) a/w (b) h/w (c) Transverse layer percentage 51
Figure 5.2. Load spread angle definition: (a,d) Actual load distribution, (b,e) Equivalent linear load distribution, (c,f) Stress distribution of FE model 53

Figure 5.3. Load-distribution angle as a function of the width of loading area to the width of CLT panel ratio in three different aspect ratios 55
Figure 5.4. Influence of aspect ratio on load spread angle 57
Figure 5.5. Influence of transverse layer percent on the load spread angle. 59
Figure 5.6. Load locations for studying the influence of loading area width and CLT panel width 61
Figure 5.7. CLT panels with different aspect ratios 62
Figure 5.8. CLT panels with different transverse layer percent 62
Figure 5.9. Loading configuration: (a) at the center of CLT panel, (b) at the edge of CLT panel 63
Figure 5.10. Predicted vs. actual angle for category 1 65
Figure 5.11. Predicted Vs. Actual angle for category 2 68
Figure 5.11. Actual compressive stress distribution (green arrows) and gross compressive mean stress (red arrows) 69
Figure 5.13. Predicted vs. actual K for Category 2 71
Appendix A.1. Displacement contour plots and displacement graph from compression test at 80% of failure load for specimen A-1- DIC (left), FE modelling (right) 80
Appendix A.2. Normal strain contour plots and normal strain graph in the y direction from compression test at 80% of failure load for specimen A-1- DIC (left), FE modelling (right) 80
Appendix A.3 Displacement contour plots and displacement graph from compression test at 80% of failure load for specimen A-2- DIC (left), FE modelling (right) 81
Appendix A.4. Normal strain contour plots and normal strain graph in the y direction from compression test at 80% of failure load for specimen A-2- DIC (left), FE modelling (right) 81

Appendix A.5. Displacement contour plots and displacement graph from compression test at 80% of failure load for specimen A-4- DIC (left), FE modelling (right)..... 82
Appendix A.6. Normal strain contour plots and normal strain graph in the y direction from compression test at 80% of failure load for specimen A-4- DIC (left), FE modelling (right)..... 82
Appendix A.7. Displacement contour plots and displacement graph from compression test at 80% of failure load for specimen A-5- DIC (left), FE modelling (right)..... 83
Appendix A.8. Normal strain contour plots and normal strain graph in the y direction from compression test at 80% of failure load for specimen A-5- DIC (left), FE modelling (right)..... 83
Appendix A.9. Displacement contour plots and displacement graph from compression test at 80% of failure load for specimen B-1- DIC (left), FE modelling (right)..... 84
Appendix A.10. Normal strain contour plots and normal strain graph in the y direction from compression test at 80% of failure load for specimen B-1- DIC (left), FE modelling (right)..... 84
Appendix A.11. Displacement contour plots and displacement graph from compression test at 80% of failure load for specimen B-2- DIC (left), FE modelling (right)..... 85
Appendix A.12. Normal strain contour plots and normal strain graph in the y direction from compression test at 80% of failure load for specimen B-2- DIC (left), FE modelling (right)..... 85
Appendix A.13. Displacement contour plots and displacement graph from compression test at 80% of failure load for specimen B-3- DIC (left), FE modelling (right)..... 86
Appendix A.14. Normal strain contour plots and normal strain graph in the y direction from compression test at 80% of failure load for specimen B-3- DIC (left), FE modelling (right)..... 86
Appendix A.15. Displacement contour plots and displacement graph from compression test at 80% of failure load for specimen B-4- DIC (left), FE modelling (right)..... 87

Appendix A.16. Normal strain contour plots and normal strain graph in the y direction from compression test at 80% of failure load for specimen B-4- DIC (left), FE modelling (right)..... 87
Appendix A.17. Displacement contour plots and displacement graph from compression test at 80% of failure load for specimen C-1- DIC (left), FE modelling (right)..... 88
Appendix A.18. Normal strain contour plots and normal strain graph in the y direction from compression test at 80% of failure load for specimen C-1- DIC (left), FE modelling (right)..... 88
Appendix A.19. Displacement contour plots and displacement graph from compression test at 80% of failure load for specimen C-2- DIC (left), FE modelling (right)..... 89
Appendix A.20. Normal strain contour plots and normal strain graph in the y direction from compression test at 80% of failure load for specimen C-2- DIC (left), FE modelling (right)..... 89
Appendix A.21. Displacement contour plots and displacement graph from compression test at 80% of failure load for specimen C-3- DIC (left), FE modelling (right)..... 90
Appendix A.22. Normal strain contour plots and normal strain graph in the y direction from compression test at 80% of failure load for specimen C-3- DIC (left), FE modelling (right)..... 90
Appendix A.23. Displacement contour plots and displacement graph from compression test at 80% of failure load for specimen C-4- DIC (left), FE modelling (right)..... 91
Appendix A.24. Normal strain contour plots and normal strain graph in the y direction from compression test at 80% of failure load for specimen C-4- DIC (left), FE modelling (right)..... 91
Appendix A.25. Displacement contour plots and displacement graph from compression test at 80% of failure load for specimen C-5- DIC (left), FE modelling (right)..... 92
Appendix A.26. Normal strain contour plots and normal strain graph in the y direction from compression test at 80% of failure load for specimen C-5- DIC (left), FE modelling (right)..... 92

Appendix B.1. DIC, Test and FE modelling results and load distribution results for specimen A-1 until failure 94
Appendix B.2. DIC, Test and FE modelling results and load distribution results for specimen A-2 until failure 94
Appendix B.3. DIC, Test and FE modelling results and load distribution results for specimen A-4 until failure 95
Appendix B.4. DIC, Test and FE modelling results and load distribution results for specimen A-5 until failure 95
Appendix B.5. DIC, Test and FE modelling results and load distribution results for specimen B-1 until failure 96
Appendix B.6. DIC, Test and FE modelling results and load distribution results for specimen B-2 until failure 96
Appendix B.7. DIC, Test and FE modelling results and load distribution results for specimen B-3 until failure 97
Appendix B.8. DIC, Test and FE modelling results and load distribution results for specimen B-4 until failure 97
Appendix B.9. DIC, Test and FE modelling results and load distribution results for specimen C-1 until failure 98
Appendix B.10. DIC, Test and FE modelling results and load distribution results for specimen C-2 until failure 98
Appendix B.11. DIC, Test and FE modelling results and load distribution results for specimen C-3 until failure 99

Appendix B.12. DIC, Test and FE modelling results and load distribution results for specimen C-4 until failure 99

Appendix B.13. DIC, Test and FE modelling results and load distribution results for specimen C-5 until failure 100

Appendix C.1. Load is applied in the middle of CLT 102

Appendix C.2. Load is applied at the edge of CLT 104

Chapter 1: Introduction

1.1 Background

Over the last decade, the use of mass timber panels (MTP) in building construction has been increasing. The most well-known MTP product is cross-laminated timber (CLT), made by gluing sawn lumber layers orthogonally in a cross-ply manner. CLT is an alternative to traditional materials such as steel and concrete in mid- and high-rise construction. In this market, although MTP has brought many advantages, such reduced construction costs due to the increased prefabrication, some technical problems need to be investigated further to allow for safe use of CLT in a range of different structures. One of these challenges is the limited technical information on the behaviour of CLT under in-plane compression loads with the loads applied to the edge of the CLT, such as in a wall under gravity loads.

Calculation of stress distribution in a member subjected to design loads is an essential part of structural design. Inaccurate prediction of stress distributions can result in either unsafe structures or uneconomical designs. When a load is applied to a structural element, it creates a load path through the element which is eventually transferred to the supporting components. In the case of axial point loads applied to CLT panels, loads tend to spread out as they travel towards the supporting structure below, as shown in Figure 1.1. As a result of the load spreading, the applied load is distributed over a wider area resulting in a lower applied stress level than that experienced at the contact surface between the applied load and the member surface.

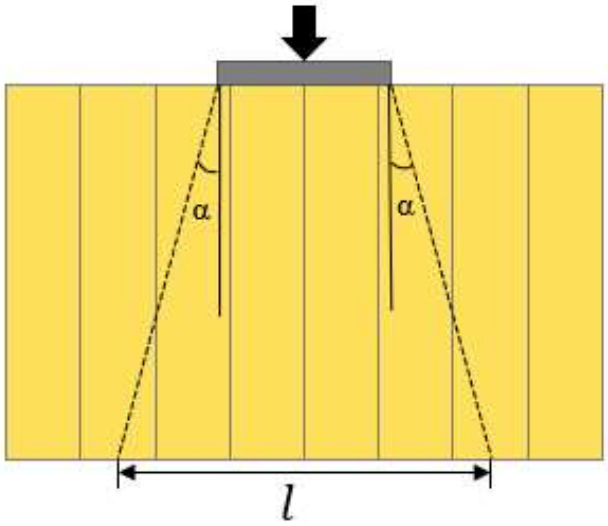

Figure 1.1. Load spread angle

The consideration of load spread angle is fundamental in designing structural elements for both steel and concrete structures. In steel structures, the load spread angle is used to design gusset plates under axial load and calculate reduced tension stress at the joint's end (Figure 1.2 (a)). In concrete structures, the load spread angle varies based on load and support types. For example, the effective width of one-way slabs for bending and shear with a vertically downward applied concentrated load near the support is determined based on the load spread angle (α). Figure 1.2 illustrates the effective width of one-way slabs under a concentrated load near the support, where the load spreads at an angle (α) from the center (b).

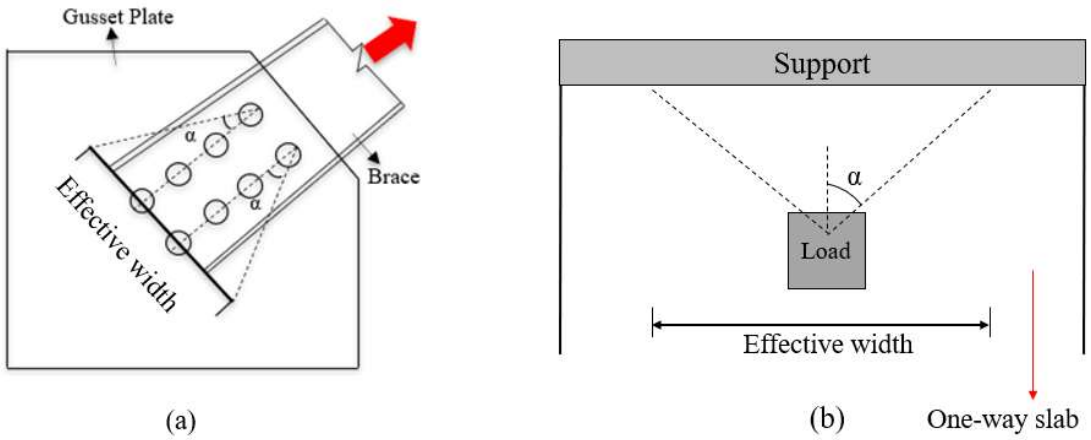

Figure 1.2. Load spread angle (a) steel component (gusset plate)-adapted from (Wang et al. 2023) *(b) load spreading from the center of the load downward to a one-way slab; top view of slab- adapted from* (Lantsoght et al. 2015)

Accurately calculating the load spread angle is critical to ensure that the design satisfies the strength and serviceability requirements. Inaccurate predictions of load spreading can result in errors and inefficiencies during the design process, potentially compromising the safety and stability of the structure. Therefore, developing a method to accurately calculate the load spread angle is crucial for safe and efficient design.

A limited number of studies have investigated the in-plane load spread angle for CLT and there are currently no appropriate design procedures available. The structural design provisions in CSA O86 (CSA 2019) for CLT under an in-plane compression load on the panel edge assume that the load is applied over the entire wall length. There is a lack of guidance for cases where the load is applied over a small wall section, such as a concentrated load. Figure 1.3 illustrates a few examples see in building structures where loads are applied in the middle or at the edge of the CLT panels.

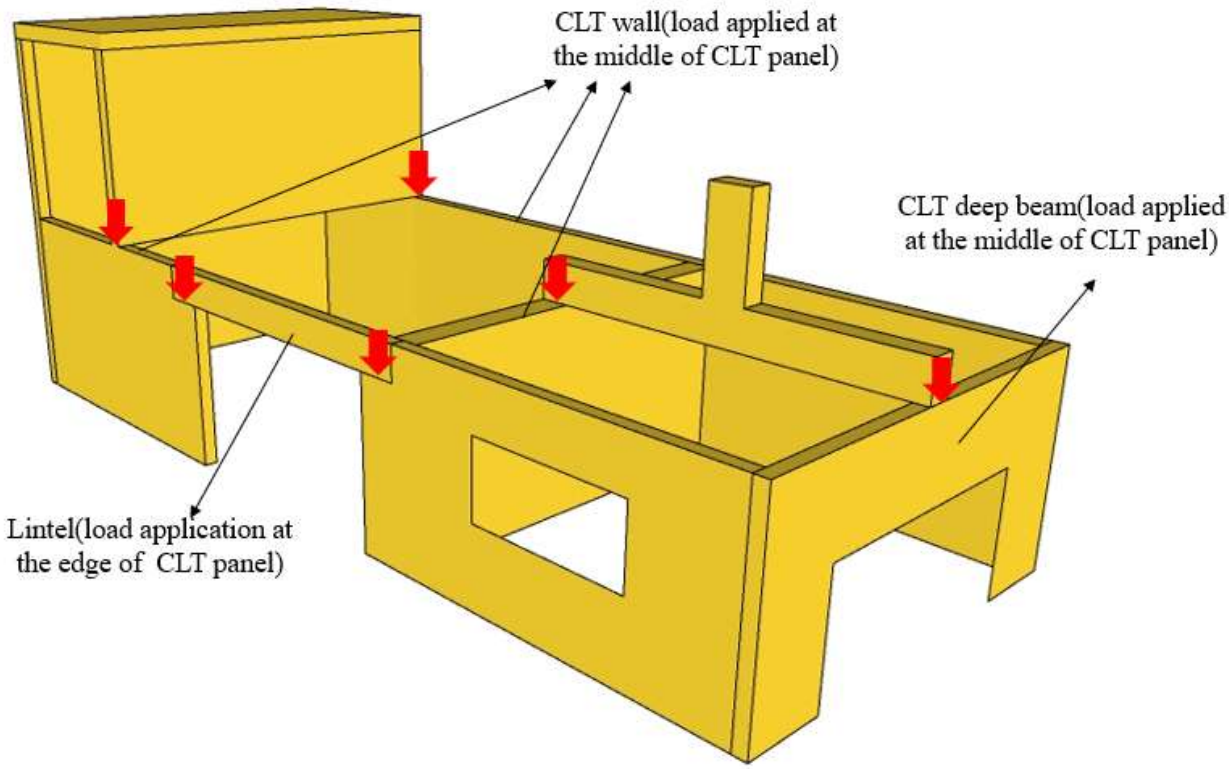

Figure 1.3. Example of CLT panels under in-plane compression applied to the edge of the panel

Under such loading conditions, the load will eventually be transferred to the supporting structure under the CLT wall. Due to the cross-laminating nature of CLT, the load transfer path may be complex, and the stress on the supporting structure would likely decrease due to the potential spreading of the load, as demonstrated in Figure 1.1. As a result of the load spread angle effect, it is conservative to assume that the stress at the supporting structure below the CLT wall is the same as that experienced at the loading point on the top edge.

An example of previous research is provided by Gräfe et al. (2018), who observed that the load spread angle for CLT under edge compression varies from 21° to 28°, depending on the transverse layer percentage, which ranges from 10% to 50%. Transverse layer percentage is defined as the ratio of the total transverse layer thickness to the total thickness of CLT.

Having a reliable method for calculating the load spread angle allows designers to ensure the design meets required levels of safety while also being economically efficient. This study aims to

investigate the behaviour of CLT panels under in-plane concentrated compression loading using numerical simulations, experimental and analysis. The main research outcomes are to better understand load distribution in CLT under in-plane compression loading and to develop a model to estimate the load spread angle in CLT structures.

1.2 Research objectives

The main objective of this study is to investigate the behaviour of CLT panels subjected to an in-plane compression loads applied to the edge of the CLT. Specifically, it is of interest to understand how the laminated structure affects the distribution of stresses resulting from a point load applied at the top of the panel. Understanding this stress distribution, and the influence of CLT layup parameters, loading location and CLT panel dimensions on stress distribution will assist in achieving a more economical design solution. An expected outcome of this project is to develop an approach for calculating load spread angle through a parametric study and multiple regression analysis. This angle is the angle between the vertical and the line from the top edge of the load area to the bottom, where the stress is practically zero. Such an approach could be implemented in timber design standards. This study can assist structural designers in gaining a better insight into the influence of different parameters, such as wall aspect ratio, loading area width to CLT panel width ratio, and transverse layer percentage on load spread angle under in-plane compressive point loads.

Research Methodology

This study investigated the performance of CLT panels under in-plane concentrated compressive loads applied to the panel edge. The research consists of three components. The first component was the testing phase in which 18 compression tests were conducted. The purpose of these tests

was to determine how a locally concentrated compression load on the narrow side of a CLT panel spreads from the loading area to the support system. To study this behaviour, several compression tests on CLT panels with different thicknesses were designed. The test matrix consisted of 18 samples containing three different layups of 3- and 5-ply CLT panels. The strain distribution was detected using a digital image correlation technique (DIC) on the front and a linear variable differential transformer (LVDT) on the back surface of the CLT panel. The distribution of the reaction force at the bottom support of CLT was measured using a series of load cells. The laboratory outcomes were then compared with finite element simulation models to validate the models.

The second component of this study was a parametric study aimed at determining the impacts of loading and panel dimension parameters on load spread angle of CLT panel. This component was studied using finite element modelling. Before studying these parameters, the finite element model was validated using test results obtained from the first component. Three parameters were selected, namely: aspect ratio of CLT, loading area width to panel width ratio, and transverse layer percent for investigation in this component. The influence of each parameter was evaluated separately. The percentage of the transverse layers varied from 13% to 50%. Three values of aspect ratio were examined (0.59, 0.88 and 1.25). Lastly, the influence of the ratio of loading width over the width of CLT panel was examined and was varied between 0.24 and 0.38.

The third component was the development of empirical equations based on the validated model and the results of the parametric study. Two cases were considered based on the loading situation: load applied at the middle of the CLT panel and load applied at the edge of the CLT panel. In the third component, FE modelling results were analysed statistically using multiple regression analyses to develop empirical equation for each loading case that predicts load spread angle based

on the three studied parameters. The final component of this study involves two compression stress modification factors (K_1 and K_2) developed for the two cases noted above, which evaluate the correlation between the maximum stress value observed in practical scenarios and its equivalent mean stress. Calculating the maximum stress can be a complex process, so it is necessary to consider an equivalent mean stress. These factors were developed based on the three parameters studied in this research. These modification factors will allow designers to predict applied stresses under point loads in CLT panels, which may then be compared with allowable stress resistance of the panel itself.

1.3 Thesis structure

This thesis consists of the following chapters:

- Chapter 2 reviews the previous studies regarding structural performance of CLT, particularly under in-plane concentrated compression loading. After presenting the existing research evaluations and findings, the gaps in knowledge are highlighted.
- Chapter 3 describes the experimental work conducted in this study. Initially, the laboratory test objectives are described, followed by an overview of the material properties, the test setup, and the test procedures. After discussing the outcomes and failure modes, the chapter ends with a discussion of test results and conclusions.
- Chapter 4 presents the 3D finite element models to simulate CLT wall. The FE models are used to predict the behaviour of CLT walls under concentrated compression loads. In this chapter, after explaining the material property inputs and FE modelling approach, the results obtained from tests described in Chapter 3 are compared with the numerical predictions.

- Chapter 5 presents a parametric study, whereby the sensitivity of load spread angle to changes in three influential parameters, aspect ratio of CLT, loading area width to panel width ratio, and transverse layer percentage was evaluated. Following this sensitivity analysis, two empirical equations are presented to predict load spread angle for two loading locations. Additionally, to evaluate the maximum stress value observed in practical situations compared to its allowable stress when CLT is subjected to in-plane concentrated compression, modification factors for two loading locations are presented in this study.
- Chapter 6 summarizes the overall thesis conclusions, the main findings, and the implications for future research.

Chapter 2: Literature Review

2.1 CLT Background

Throughout history, most timber structures have been lightweight frameworks with linear elements made of timber (Jeleč et al. 2018). The availability of modern mass timber products (MTPs) has allowed wood to be used in a greater variety of structures, thus increasing its market share in the construction industry (Li et al. 2019). CLT panels are often made up of an odd number of layers, with three to seven layups being the most common lumber boards are cross stacked in alternate grain directions and orthogonally glued laminations, as shown in Figure 2.1. On the narrow face of each layer, adjacent lumber layers may be edge glued. In certain product configurations, adjacent lumber layers may be aligned in the same direction, resulting in higher structural capacity in the major direction. CLT's high levels of in-plane and out-of-plane load capacity make it suitable for use as wall or floor panels under various loading conditions.

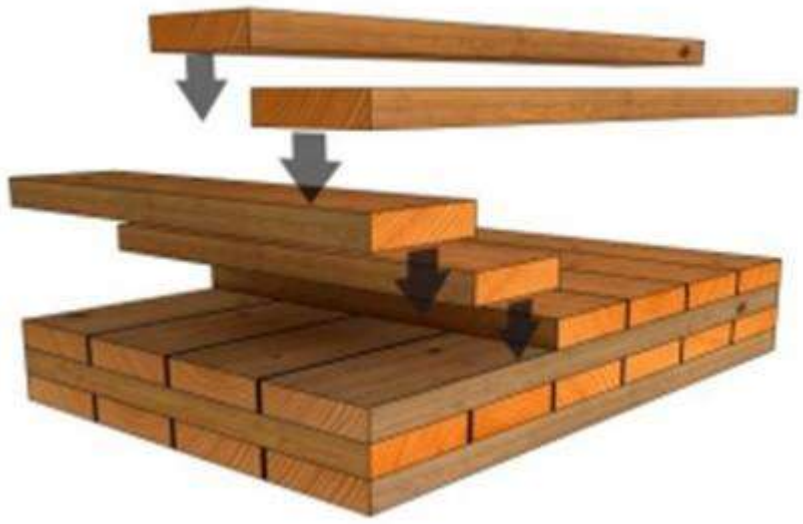

Figure 2.1. A typical CLT layup (Buck et al. 2016)

During the mid-1990s, CLT was patented as part of a subsequent development incentive to encourage further development. In 1990, the Graz University of Technology, Austria began conducting extensive research on CLT. There have been three long-term research projects carried out by Graz, followed by a number of international projects. Cross-laminated timber was also used in residential buildings in Switzerland and Germany around the same time. In the following years, there has been a significant increase in CLT research worldwide.

Central Europe was the first region to grant national technical approval for CLT in 1998. The European Union granted approval for the first CLT product in 2006 (Niederwestberg 2019). The SOFIE project, which included shake-table testing of a seven-story CLT building, was carried out in 2006 to demonstrate the performance of a mid-rise CLT building under seismic action (Ceccotti et al. 2013). This research was a collaborative work between Japanese and Italian researchers. CLT has become increasingly popular in building construction in the second decade of the 21st century. European work has shown that CLT can be a competitive construction material, especially in mid-rise and high-rise buildings, compared with steel and concrete. Because of the high prefabrication level, on-site work mainly involves only connecting and assembling individual panels. This allows for significant reductions in project construction time. Additionally, massive wood structures provide efficient thermal insulation, sound insulation, and fire resistance (Karacabeyli and Gagnon 2019). Aside from high-rise buildings, CLT can also be used to construct box-girder bridges, where it can either be used alone or in combination with other wood- or steel-based materials (Jeleč et al. 2018).

In the recent years, CLT has gained more widespread attention globally. Research, development, production, usage, and standardization activities have been carried out on a global basis in countries like Canada, the United States, Japan, China, and New Zealand. FPInnovations published the first edition of the CLT Handbook in 2011, followed by the American version in 2012 (Karacabeyli and Gagnon 2019). In North America and elsewhere, these resources were valuable

for CLT product design as there was no other information available in design standards at that time (Parajuli et al. 2018). Eurocode 5, published in 2004, is the most commonly used standard for structural timber design in Europe. The Japanese design manual for CLT construction was published in 2013, while the South African Building Standards (SABS) was released in 2020. The SABS is a modified version of the US ANSI/APA PRG 320, which serves as the CLT product standard in North America. There are currently no design or construction standards for CLT structures in Australia and New Zealand (Kurzinski et al. 2022).

2.2 Compression perpendicular to grain and bearing capacity

Timber, as an anisotropic material, has a lower capacity when it is under compression perpendicular to the grain, Design of timber structures therefore often involves minimizing compressive stress perpendicular to the grain direction (Dietsch and Brandner 2015, Alinoori et al. 2020)

There have been several studies on timber beam behavior under compression perpendicular to the grain in the literature. Van der Put (2008) offers a theoretical basis for the design rules proposed in EC5 (Eurocode 2005) related to the bearing strength perpendicular to the grain of locally loaded timber blocks. The study presented a method of plasticity to derive an analytical function that accurately represents slip-line construction results, determining the direction of the main stresses. This function is determined by taking into account various specimen parameters, including the loading area, height, distance from the loading area's edge to the specimen's edge as well as the specimen width. The function is based on theoretical principles, but is calibrated using a range of experimental data, limiting it's use for broad design rules. His model was able to predict load spreading under compression perpendicular to grain and could be implemented as reliable and simple design rules in timber design standard. Figure 2.2 shows a specimen under the applied compressive stress and the slip-lines that indicating the main stress directions (Van Der Put 2008).

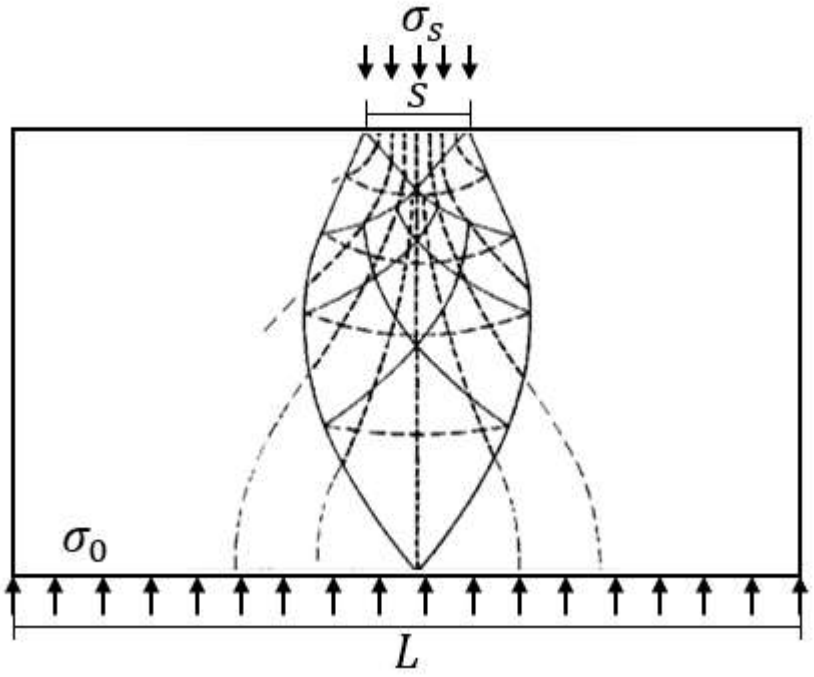

Figure 2.2. "Slip-lines" determining the direction of the main stresses (Van der Put 2008)

Leijten (2010), provides valuable insights into the challenges of finding a reliable model for compressive strength perpendicular to the grain in timber structures. The study discusses the significance of this strength in structural design and the different approaches taken by standardization committees globally. The study stated that the European Standard approach is more theoretical by focusing on well-defined basic material properties, while the US/Canada and Australia/New Zealand approach is more practical by reflecting typical uses for timber structure standardization. Furthermore, they evaluate several models proposed to predict perpendicular to grain strength using a database of 685 test results and shows that there is no reliable model that accounts for the full range of beam size and load configurations. They also showed that design codes and test methods were inconsistent and led to very different strength values. According to the study, the model developed by Van der Put is the only one that explains the different test results obtained from standardized test methods (Leijten et al. 2010).

In another study, Leijten et al. (2012) successfully applied Van der Put's physically based stress distribution model to determine the bearing capacity of continuously supported timber beams. The

study discusses the local bearing capacity perpendicular to the grain of structural timber elements, considering variations in the stress distribution slope due to grain deformation perpendicular to the grain.

When the deformation is between 3-4%, a 1:1 slope in the stress distribution under the applied load, this slope changes to 1:1.5 when the deformation increases to 10%. Figure 2.3 shows the stress distribution of timber blocks under local loading perpendicular to the grain where l is the length of continuous support and l_{eff} is the effective stress distribution length. This study demonstrates the feasibility of using a physically based stress distribution model in various practical design situations, including the determination of timber beam bearing capacity. This model was able to predict load-spreading under compression perpendicular to grain and could be implemented in reliable and simple design rules in timber design standards (Leijten et al. 2012).

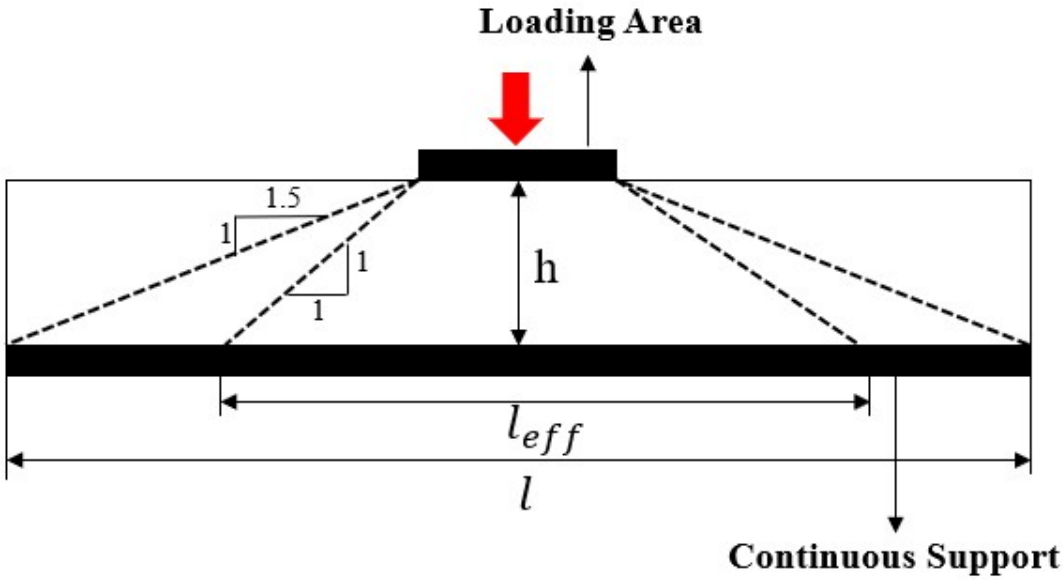

Figure 2.3. Stress distribution of compressive locally loaded for timber beams perpendicular to the grain - adapted from (Leijten et al. 2012)

In his last study, Leijten (2016) evaluated the reliability and accuracy of different bearing strength capacity models for spruce wood using a large experimental database to cover various design situations. Over 1000 test specimens conducted by researchers covering eight practical load cases were analyzed. The study emphasizes the importance of a unified approach to determining the

standard compressive strength perpendicular to grain. Three structural timber design models were evaluated, including physical models by Van Der Put (2008), semi-empirical models by Lathuilliere et al. (2015) and empirical models given by Eurocode (2005) for predicting compressive strength perpendicular to the grain. The research confirmed that existing models are generally unreliable, with only one yield slip-line theory-based model proving to be accurate. The analysis of the results shows that Van der Put's physical model emerged as a promising candidate for the new generation of timber design codes implementation, given its consistency and accuracy for all load cases tested (Leijten 2016).

A number of studies have also examined cross-laminated timber under compression perpendicular to the grain. Serrano and Enquist (2010) used several test setups with different types of loading, including uniform and line load compression over the surface of the CLT to investigate the stress distribution within the specimen. Based on the test results, they concluded that the compression strength defined in EC5 (Eurocode 2005) is affected by the relative sizes of the load application area, load direction in relation to the surface grain directions, and distance of loading point from the specimen edge (Serrano and Enquist 2010).

Brandner (2018) discussed the stress distribution models for CLT under compression perpendicular to the grain by comparing with results from several compression tests. His study tested various loading and support types, including point and line loads at the end and inside of continuously supported beams and partially supported beams. In addition, a series of specimens were loaded over the entire surface to determine their basic properties with different moisture content and surface areas. Based on these tests, Brandner presented a new stress distribution approach based on Van der Put's model, explaining how specific parameters, such as load configuration, contact area, support conditions, thickness and layout of CLT, clear edge distance, and edge spacing, influence stress distribution (Brandner 2018).

2.3 Behaviour of CLT panel under in-plane uniform compressive load

Oh et al. (2015) provided a model to predict the strength of block CLT specimens under continuous in-plane compression load by assuming that the transverse layers provide no resistance. Thirty-four test specimens with different timber grades in the longitudinal and transverse layers of CLT panels (short column) were tested to validate the model. The model was used to study the effect of laminate width and wall length on the compressive strength of CLT panel. The compressive strength increased as the laminate width decreased. Based on this finding, CLT panel layups can be developed to optimize its load-carrying capacity under continuous in-plane compression loading (Oh et al. 2015).

Pang and Jeong (2018) proposed a new approach for predicting the CLT compressive resistance and compared it with existing methods. In their study, they examined 120 specimens with varying grades, lay-ups, and thicknesses. They evaluated the compressive resistance of CLT panels using three different methods. The first method predicts CLT compressive resistance by multiplying the laminate's compressive strength and cross-sectional area aligned with the loading direction. In the second method, the laminate's stiffness ratio is also considered. A third method, developed by Pang and Jeong (2018), calculates compressive resistance while accounting for load sharing and weakest laminate effects. According to these experiments, most of the compression load was supported by laminates parallel to the loading direction. In conclusion, methods 1 and 2 were practical when one laminate grade was used for all layers parallel to the loading direction. Method 1 overestimated the results by up to 43.4% when using different grade laminates parallel to the loading direction. The overestimated values found in method 1 were reduced by 38.8% by method 2. Method 3 reduced the difference between predicted and measured values by 8.7–10.8% when different grade laminates were used for layers parallel to the loading direction. Overall, they showed that method 3 provided the most accurate prediction laminate (Pang and Jeong 2018).

2.4 Behaviour of CLT panel under in-plane compressive concentrated loading

In previous sections, several studies on the response of CLT under out-of-plane and in-plane loading were presented. A specific in-plane loading condition where a concentrated compression load is applied to the edge of CLT is of interest in this study and previous research in this area has been limited. The following is a review of the relevant studies.

Gräfe et al. (2018) examined how a CLT panel responds under in-plane concentrated loading. With the help of mechanical testing and finite element modelling, the load spread angle of CLT panels under concentrated compressive load was calculated. Several parameters influenced the angle, including the bonding of narrow faces, the width of single laminates, the specimen height, the proportion of transverse layers, and the stiffness of the bottom edge contact surface. Observations indicate that the load spread experienced by the bottom contact surface is always nonlinear, with the maximum load located at the center. According to their study, the maximum load at the center was underestimated due to the linear load distribution. Figure 2.4 shows the variation of load spread angle with different transverse layer percent based on experiments and numerical modelling (Gräfe et al. 2018).

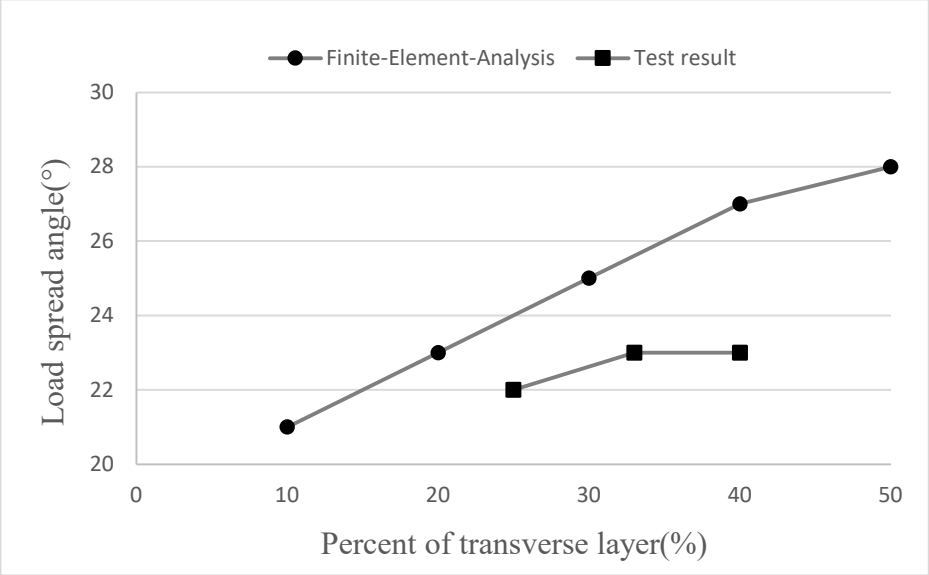

Figure 2.4. The comparison of the load spread angle based on FE modelling and test results (Gräfe et al.2018)

Wu et al. (2022) developed a finite element (FE) model for the buckling behaviour of partially loaded CLT members. Partial load refers to a load exerted on only part of a member. They conducted sixteen tests in four groups with different slenderness ratios. The width and thickness of the CLT members was constant, while the height varied. FE modelling was used to validate the experimental tests. A comparison between measured and simulated buckling capacities was performed, and the results were reasonably similar. After validation of the FE model, this model was used to investigate the buckling capacity of partially loaded members with different slenderness ratios and load-bearing length ratios. In fully loaded members, the stress was evenly distributed across the width but distribution was varied in partially loaded members. Figure 2.5 shows the stress distribution of CLT under in-plane partial loading. As can be seen in the figure, the CLT is partially loaded at the top and bottom. The horizontal axis in the figure is the distance from the left-hand corner of the CLT panel and the stress in y-axis is that along the red line in the figure i.e. at mid-height. This figure shows that the stress decreases moving away from the loading area. In addition, it was found that the buckling capacity of CLT members increased as the loading width to CLT width ratio increased. Finally, numerical results led to the formulation of an

equivalent width method (EWM) for calculating the buckling capacity of partially loaded CLT members (Wu et al. 2022).

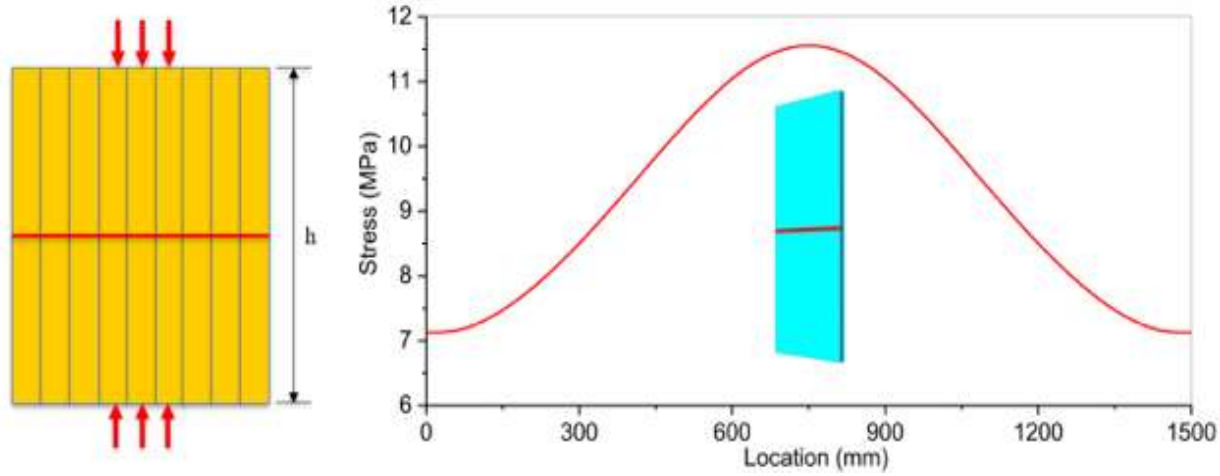

Figure 2.5. Stress distribution within the width of in-plane partial loading of CLT panel (Wu et al. 2022)

In another study, Totsuka et al. (2022) present a method for evaluating the strength and stiffness of the narrow face of a CLT panel subjected to a concentrated compressive load. They evaluated 42 specimens, with different loading plate widths, loading plate side margins, and loading directions (weak or strong axis), and compared tests results with FE model predictions. FE modelling results showed similar trends to the experimental results. Therefore, it was assumed that the verified model could be used to study physical behaviour of CLT under in-plane compression loads. FE modelling was used to develop an equation to predict the dimensions of the indented areas caused by the applied compression load. Indentation occurs in the area of the load and its surroundings when a point load is applied to a CLT panel surface. Two exponential function curves were introduced to assess the dented curves around a loading plate for laminates under in-plane concentrated compression perpendicular and parallel to the grain in CLT. Totsuka et al. (2022) also proposed equations for predicting the yield stress and Young's modulus of CLT under in-plane compression based on the material properties of the laminates (Totsuka et al. 2022).

Despite the above research on the behaviour of CLT panels under in-plane compressive loading, the situation where a concentrated compression load is applied at the top of a panel with continuous support at the base has not yet been investigated. This situation is more likely to occur in practice than those which were investigated in the research studies described above; several examples are illustrated in Figure 1.3. Additionally, it is desirable to develop a simplified design model to allow designers to predict the load spread angle under concentrated loads without the use of more complex methods such as FE modelling. The need to address these gaps is the motivation for the current study.

Chapter 3: In -plane compression test of CLT panel

3.1 Introduction

This chapter describes the experimental phase of this project. There are two main objectives of this phase. First, it was to understand the load distribution in CLT panel under partial in-plane compression load. The second objective was to provide test data to validate the FE models developed in this study and described in Chapter 4. The materials and their properties used in the tests, experimental setup and test procedure are described. This is followed by a discussion of the test results.

3.2 Compression Test

3.2.1 Materials

In this experiment, CLT panels with Spruce-Pine-Fir (SPF) lumber were used. These panels are categorized according to their thickness, such as 87V, 139V, and 175V. Based on the manufacturer's product brochure (Structurlam 2020), the 87V and 139V types were graded as V2.1, and the 175V types were classified as V2M1.1. The V2M1.1 grade is made up of SPF No.2 lumber in both longitudinal and transverse layers, while the V2.1 grade comprises SPF No. 2 lumber in longitudinal layers and SPF No. 3 lumber in transverse layers. These CLT panels are made from nominal 2 x 6 inch (38 mm x 140 mm) pieces. Longitudinal lumber thickness was 35mm, whereas transverse lumber thickness was either 17mm or 35mm. Polyurethane (PUR) adhesive with the commercial brand Henkel Loctite HB X Purbond was used for the face bonding of the CLT panels.

The investigation aimed to quantify the load distribution along the bottom edge of the CLT under an in-plane point compression load applied at the upper edge. A total of eighteen CLT specimens consisting of 4 groups of three- and five-ply CLT were tested (Type A, B, C and CH), as shown in Table 3.1. Types A to C consist of specimens with the same plane dimensions but differ by the number of layers (A vs B) and transverse layer thickness (B vs C). Type CH specimens have smaller height but the same thickness as type C.

Table 3.1. Details of CLT specimens

Type	ID	No of layers	Layer orientation	Thickness	width	Height	Longitudinal layer	Transverse layer	No of replicates
				[mm]	[mm]	[mm]	[mm]	[mm]	
87V	A	3	//-⊥-//	87	680	400	35	17	5
139V	B	5	//-⊥-//-⊥-//	139	680	400	35	17	5
175V	C	5	//-⊥-//-⊥-//	175	680	400	35	35	5
175V	CH	5	//-⊥-//-⊥-//	175	680	250	35	35	3

3.2.2 Test set-up

The test setup includes a CLT specimen subjected to a concentrated load applied through a laboratory load frame. These tests were performed with a Tinius Olsen universal testing machine that had a capacity of 1700 kN. Figure 3.1 presents a schematic representation of the test setup, where the load is applied to the upper steel plate and transmitted through the CLT laminates to the layers below. As indicated in the figure, the concentrated compression load is applied at the top of the specimen, indicated by a green arrow, and the transmitted load is applied to the lower plates, shown by red arrows.

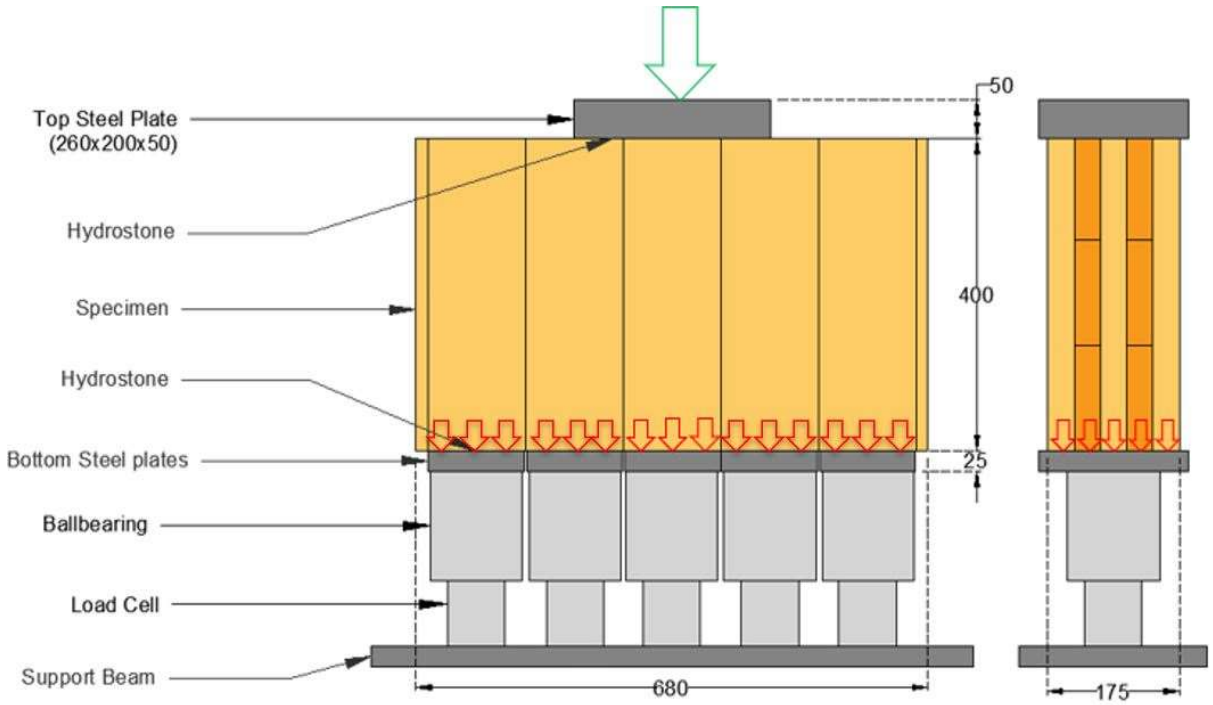

Figure 3.1. Test Setup – schematic

To measure transmitted load, the specimen was instrumented with load cells. Five load cells were used to measure load distribution along the length of the CLT specimen. Load cells were mounted on a support beam in a row next to each other. The load cells were equipped with five spherical ball bearings to ensure concentric load application. The specimen was also separated from the ball bearings by five discrete steel plates spaced 2mm apart. The uneven surface between the specimen and the steel plates caused some challenges and could potentially contribute to measurement errors. Therefore, leveling out the unevenness in this contact area is necessary. This issue was mitigated by placing a plastic sheet on the plates and pouring hydro-stone over the plastic sheet. Hydrostone was placed on the top and at the bottom of the CLT specimen, see Figure 3.1. The actual test setup can be seen in Figure 3.2.

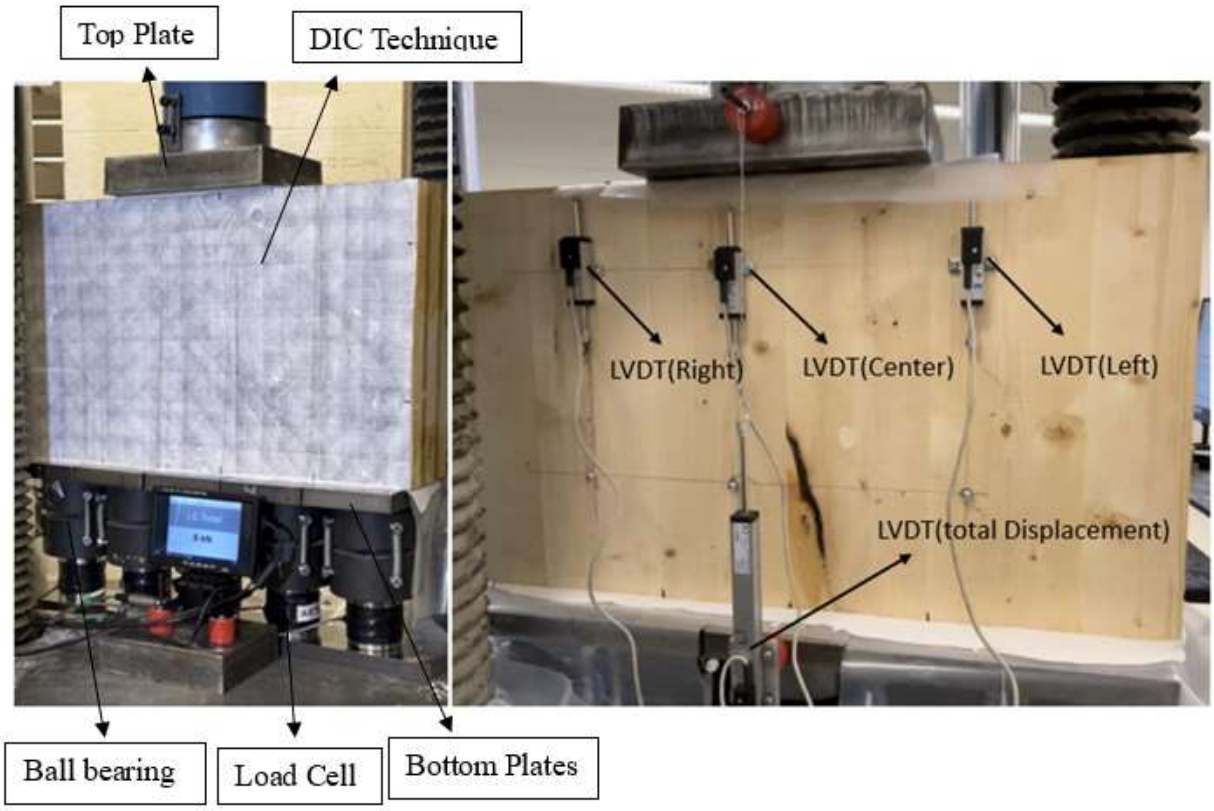

Figure 3.2. Actual Test Setup-Front (Left)-Back (Right)

Load measurement system

This system consists of upper and lower steel plates, ball bearings, load cells, and CLT specimen. In this setup, the lower and upper steel plates were made of grade A36 steel, which are usually hot-rolled plates. As far as mechanical properties are concerned, A36 has an ultimate tensile strength of 400-550MPa and yield tensile strength of 350MPa. Additionally, it's modulus of elasticity is 200GPa with a Poisson's ratio of 0.3. The upper steel plate dimensions are 260mm in length, 200mm in width, and 50mm in thickness. The dimensions of the lower steel plates are 200 mm long, 130 mm wide, and 25mm thick. The determination of the steel plate thickness is explained below.

In order for the steel plates to resist bending in two directions, the required thickness for the lower steel plates was analysed. The thickness must be sufficient to prevent significant deformation of

the steel plate, which could affect the accuracy of the force measurements by the load cells. An FE analysis was performed using ABAQUS software (Simulia. 2020) to confirm the thickness design of the bottom steel plate. Based on a simple analysis using the compressive strength of lumber, the expected maximum load reached by that plate was estimated conservatively as 1000kN. In addition, the lower plates are assumed to be 25mm thick, and both the ball bearing and steel plate are assumed to have a modulus of elasticity of 200GPa with a 0.3 Poisson's ratio. Due to the steel plate's yield strength of 350 MPa, the von mises contour result is limited to +/- 350 MPa. Figure 3.3 shows the stress contour of a lower steel plate obtained from FE analysis under a 1000 kN load. As it is shown, the maximum stress in the steel plate is 350MPa. This means that the 25mm thickness is adequate.

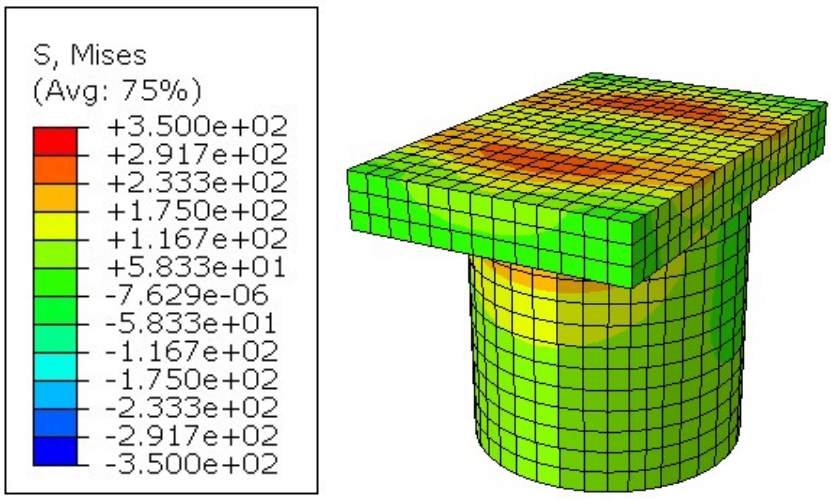

Figure3.3. Stress contour in lower steel plate obtained from FE Analysis

Five spherical ball bearings are responsible for decreasing rotational friction and ensuring concentric load was applied to the load cells, which were placed between the lower steel plates and load cells. The reaction forces were measured by five load cells with a capacity of 600kN, which were fabricated and calibrated by the laboratory technicians. The steel material of the load cell has a yield strength of 275MPa, an ultimate tensile strength of 517MPa, Young's modulus of 200GPa, and a Poisson's ratio of 0.3. Each load cell consists of four biaxial strain gauges. Several

calibration tests were carried out after manufacturing the load cells. The accuracy of the load cells was estimated to be about 0.5% of the ultimate capacity.

Deformation measurement using LVDT and DIC

The physical deformations were measured using linear variable differential transformers (LVDTs). In addition to using LVDT, Digital Image Correlation (DIC) technique was also used to measure the strain on the surface of the test specimen. Wood material properties can be characterized with the DIC technique by measuring strain directly on the surface. A DIC measurement process generally requires three consecutive phases. During these phases, the experimental set-up was prepared, the DIC images were captured during the loading test, and images were analyzed using DIC software. The camera should be positioned with its optical axis normal to the specimen surface. Before testing the specimen, the surface was sprayed with a speckle pattern. Pictures were taken every two seconds of a designated speckled area. Synchronizing the recorded load with the DIC images was accomplished using a small monitor placed in front of the camera. To analyze DIC images, VIC-2D commercial DIC software was used. Analysis of the digital images before and after deformation using the DIC software led to the determination of the full-field displacement and strain. Creating a specific path over the speckled area can extract strain values from the software. The front face of the CLT specimen was marked to determine the exact location of the LVDT mounted on the backside. Using these markings in VIC-2D software allowed for more accurate locating of points in the speckled area.

3.2.3 Test Procedure

The CLT panels were prepared for DIC using a dot-size stamp roller to paint random dots on the surface before testing. Load cells and LVDTs were then connected to data loggers with sixteen and nine channels, respectively, to record data automatically. LVDT and DIC were utilized to

record the displacement and strain field. Three LVDTs were mounted on one face of the CLT panel at predetermined locations to measure the CLT specimen's local deformations and validate the DIC measurements. Every specimen of the same group had the same locations for the LVDTs to facilitate meaningful comparison. These positions were adjusted slightly to prevent the LVDT from being placed at the gap between laminates. Additionally, an LVDT was placed between the upper and middle lower steel plates to measure the total deformation of the specimen.

A vertically arranged hydraulic cylinder applied the compression load to the centre of a steel load distribution plate. The specimen underwent a pre-programmed force control load at a rate of 2 kN/s using the Tinius Olsen machine. During the test, the total load applied was checked with the total load shown on the screen every 100kN to detect possible deviations. Additionally, the reaction forces measured by the five load cells were displayed separately on a computer monitor. The load was applied until the failure of the specimen was noted, which was identified by monitoring the force-displacement curve during the test and by visual examination of the specimen.

3.3 Test Results

Table 3.2 shows a summary of the compression test results. This table displays the vertical stiffness for each specimen. This value represents the maximum applied load divided by deformation at the location of the ultimate point in the vertical direction.

Table 3.2. Compression Test Results

Type	Specimen	Thickness (mm)	Maximum Load (kN)	Max Displacement (mm)	Vertical Stiffness (kN/mm)
A [(1)]	A1	87	749	2.34	357
	A2	87	671	3.05	252
	A3	87	754	3.32	256
	A4	87	697	3.12	245
	A5	87	721	2.05	364
B	B1	139	962	2.38	432
	B2	139	935	4.40	284
	B3	139	983	3.88	298
	B4	139	1168	2.16	662
	B5	139	1083	2.15	536
C	C1	175	1225	3.03	495
	C2	175	1041	3.21	398
	C3	175	1112	3.15	429
	C4	175	1150	2.98	485
	C5	175	1155	2.27	564
CH [(2)]	CH1	175	1107	2.62	579
	CH2	175	1112	2.65	500
	CH3	175	925	1.92	486

(1) Type A specimens are 3-ply CLT panels

(2) The height of type CH specimens is 250mm

Figure 3.4 shows the face plane and the load-displacement curves of type A specimens. According to Table 3.2, the ultimate load for this specimen type is between 671 - 749 kN with the maximum displacement between 2- 3.3 mm. Figure 3.4 illustrates that the steel plate under compression is positioned at a different location relative to the panel lamination gaps for the different specimens. The results of Figure 3.4 and Table 3.2 indicate that stiffness values of A2, A3 and A4 specimens were about 30% lower than those of A1 and A5. The load-deformation curves for A1 and A5 are similar to each other. There was no obvious reasons why A1 and A5 have higher stiffness values, although they do have high peak loads relative to others. In general, because of their smaller

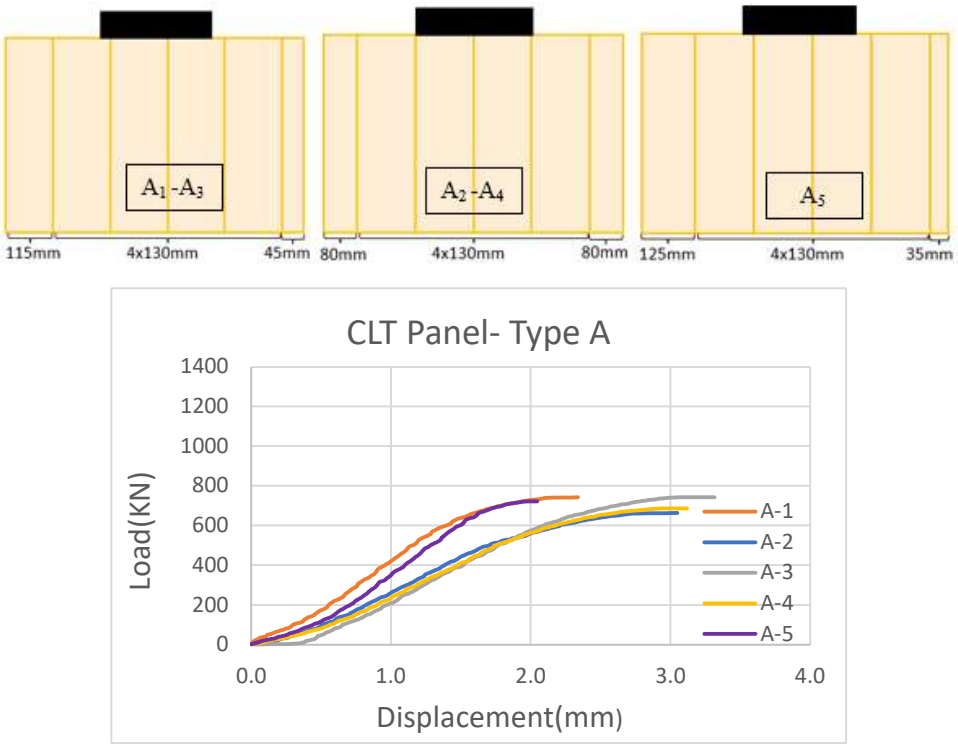

Figure 3.4. Type A specimens and load-displacement curves

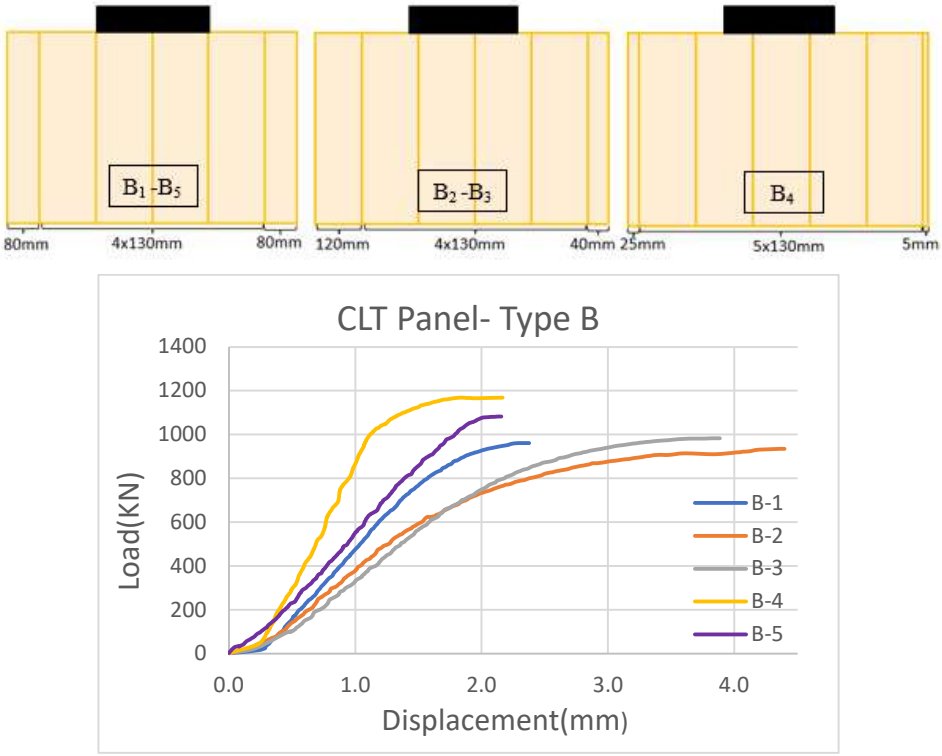

Figure 3.5. Type B specimens and load-displacement curve

thickness and fewer layers, type A specimens achieved the lowest maximum load among all the types. The load-deformation responses for type B specimens are shown in Figure 3.5. Based on Table 3.2, the maximum forces and displacements for type B specimens range between 936 and 1168 KN and 2.15 and 4.40 mm, respectively. Specimens B1 and B5 exhibit similar patterns, with higher maximum loads than specimens B2 and B3. It is noted that specimen B4 is the most symmetric specimen which recorded the greatest vertical stiffness compared to the other specimens. Generally, the vertical stiffness values of B5 and B1 are 80% and 65% respectively of that of B4. Similarly B2 and B3 stiffness values are about 44% of that of B4.

Figure 3.6 shows the position of the loading area and load-displacement curves of type C specimens. It can be seen that type C specimens have the highest compression strengths on average (1041 – 1225 kN) in comparison with other types. The loading area placed in almost the same position relative to lamination gaps for all of the specimens of this type resulted in fairly similar load-displacement responses. This figure shows that the difference between the highest vertical stiffness (C5) and the lowest (C2) is approximately 30%.

Figure 3.7 shows the load-displacement responses for type CH specimens. The difference between type C (400mm) and CH (250mm) is its height. The aim is to determine how height influences the load distribution in CLT. As can be seen, specimens CH1 and CH2 exhibit nearly identical patterns, with maximum load being around 1100 kN, while the maximum load for specimen CH3 is about 16% lower. Moreover, the measured applied load of specimens CH1 and CH2 increases until the peak value and then levels off. As a result, these two specimens had considerable deformation at the end, as compared to specimen CH3, which did not experience much deformation following its maximum load. The slope of CH1 is steeper than that of CH3, which means that specimen CH3 has approximately 16% lower vertical stiffness than CH1.

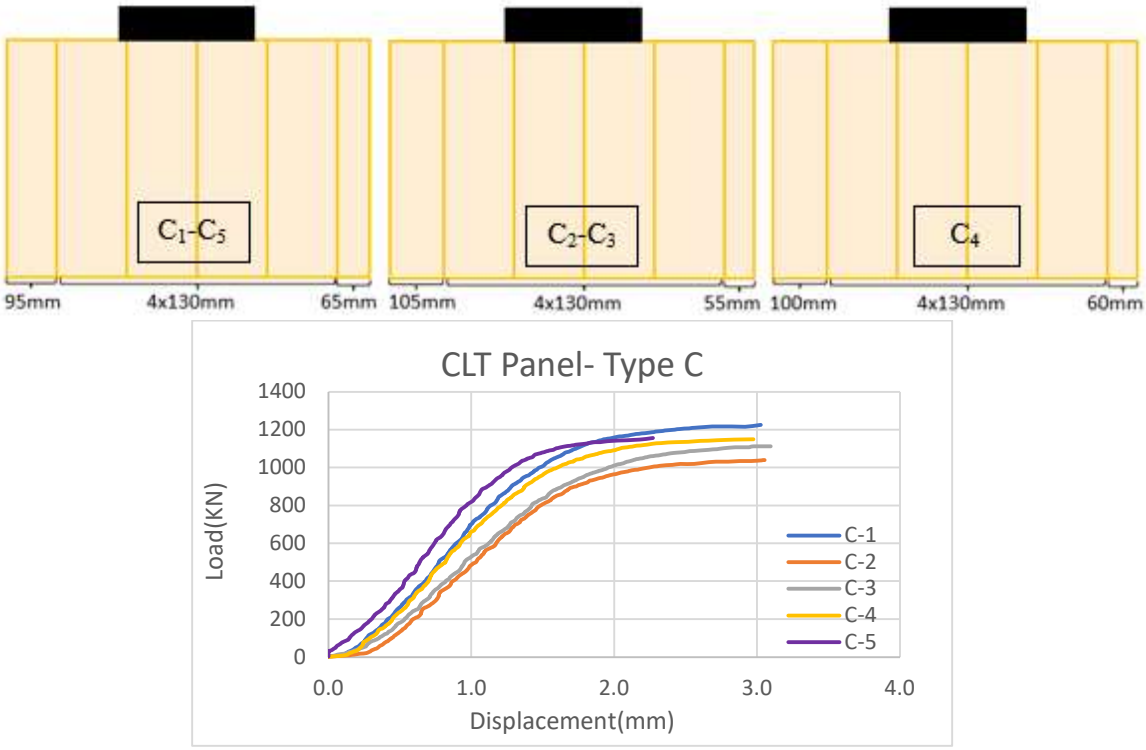

Figure 3.6. Type C specimens and load-displacement curve

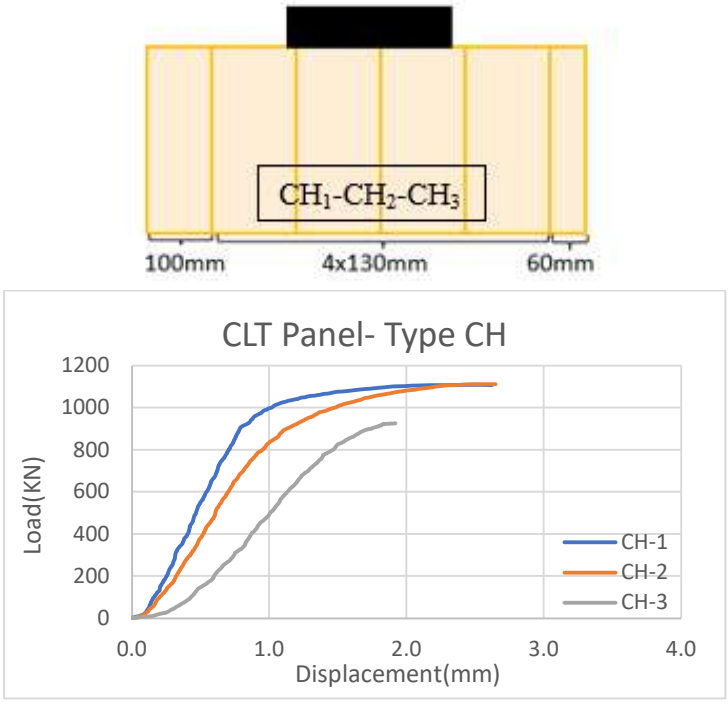

Figure 3.7. Type CH specimens and load-displacement curve

Overall, by comparing all types of specimens, it is obvious that by increasing the thickness of CLT panels, compression strength increases. Here, from type A specimens with 87mm thickness to type

C specimens with 175mm thickness, this value on average was raised by almost 60%. Both type B and type C specimens had 5 plies with a transverse layer percentage of 24.5% and 40%, respectively. As previously mentioned, type C used SPF No.2 in both longitudinal and transverse layers while type B used SPF No.2 for longitudinal and SPF No.3 in transverse. It was observed that the compression resistance increased on average by about 10% from type B to type C. The test results suggest that most of the compression load is supported by laminates parallel to the loading direction, which is consistent with Pang and Jeong's (2018) results. In addition, although type CH specimens had on average a 10% lower maximum load than type C specimens, there is no evidence to suggest that the maximum load is influenced by specimen height.

3.3.1 Failure Modes

A few potential defects were noted on CLT panels as shown in Figure 3.8. These were caused by

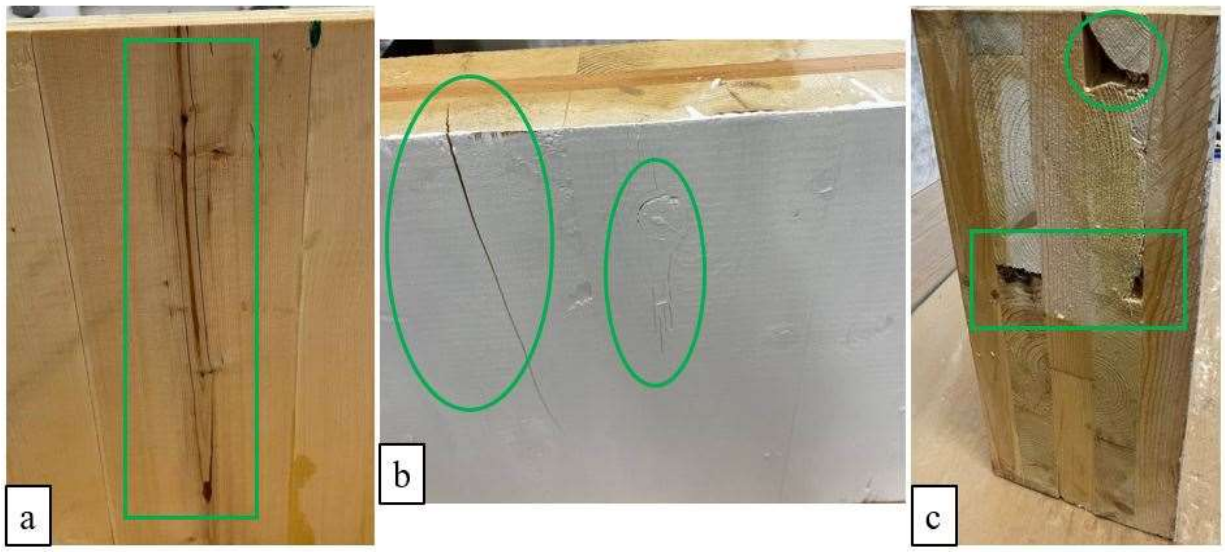

Figure 3.8. Defects on CLT panels before testing: (a) split, (b) knot and check, (c) transverse lumber wane

the characteristics of the wood, environmental condition and manufacturing process. Significant fractures can occur on the CLT face, including cracks caused by knots and lamentation gaps due to shrinkage. These imperfections can reduce the strength of CLT panels. Figure 3.9 illustrates the

typical failure modes of four specimens from type A to CH. It was observed that the predominant failure mode of compression tests was punching under the loading area. Fractures under the loading area indicate that there has been significant stress in this area. Specimen A1 clearly shows wood splinters surrounding knots and wood splitting under the steel plate. In specimen B5, the steel plate was precisely placed between two gaps, causing significant punching, and demonstrating concentrated stress between the two parallel red lines. This punching contributes to considerable horizontal fractures at a short distance below the applied load.

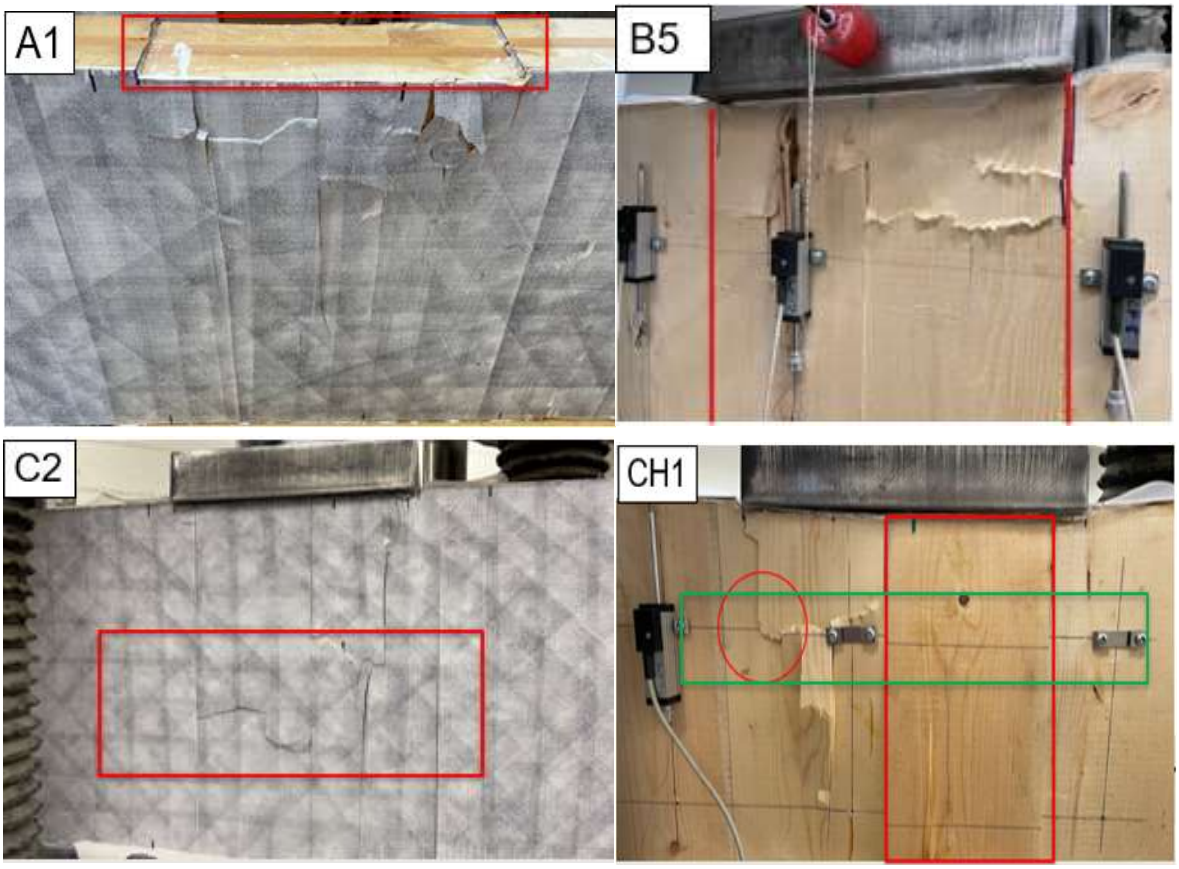

Figure 3.9. Some examples of compression failure modes

The fracture in specimen C2 appears to be far from the steel plate in the middle. It can be interpreted as a better distribution of load for this specimen. Since type CH specimens are shorter than other types, most of the compression is resisted by the middle laminate, resulting in less load distribution. A closer look at the specimen reveals both local buckling and local shattering.

Furthermore, local displacement is apparent following the black line inside the green rectangle, indicating the LVDT position.

Chapter 4: Numerical Simulation

4.1 Introduction

This chapter describes the development of a three-dimensional numerical model that simulates the CLT panel specimens tested in this study and described in Chapter 3. An overview of the simulation procedure is provided along with the component material properties, boundary conditions, interaction definitions, and mesh definitions. Models are created with the ABAQUS finite element (FE) software (Simulia. 2020). In terms of structural mechanics, FE software, such as ABAQUS, provides engineers with many features that will allow them to develop detailed and advanced models of structural problems. Once the FE model is validated with test data in Chapter 3, it provides an invaluable tool to investigate the influences of different parameters, such as geometry, layup arrangement, laminate thickness, etc., on the behavior of CLT under in-plane edge compression.

4.2 FE model development

4.2.1 Selection of element types

The numerical models include components representing the longitudinal and transverse laminates, the upper steel plate, the lower steel plates, and ball bearings. The components are all modeled as solid, deformable elements in three dimensions. The components were created by sketching a 2D cross-section and extruding it into 3D. The C3D8R (3-dimensional eight-node continuum linear brick element with reduced integration) and the increased hourglass control are used to model all the components, as shown in Figure 4.1. Geometric nonlinearity (Nlgeom) was also turned on for all analysis steps and all models. The gaps between adjacent laminates were assumed to have zero

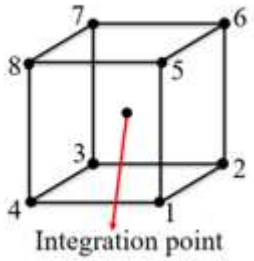

Figure 4.1. 8-node brick element schematic, C3D8R

dimensions. The dimensions of the laminations were measured and used for the component modelling. According to Table 3.1, three types of specimens with different thicknesses and heights are presented. All models have a width of 680mm with different thicknesses, 87mm, 139mm, and 175mm consisting of either three or five layers of laminates. In the five-layer CLT models, the outer layers as well as the interior layer consist of longitudinal laminates, whose fiber direction is parallel to the applied load, whereas the other two interior layers are composed of transverse laminations, and their fiber orientation is perpendicular to the applied load. For three-layer CLT, the outermost layers consisting of longitudinal laminations with fibers aligned parallel to the applied load and the middle layer consisting of transverse laminations with fibers oriented perpendicular to the applied load.

To ensure the validation of Finite Element (FE) models using test specimens, all components were taken into consideration, as any missing component could potentially lead to errors in the obtained results. During the validation process, it was observed that the movement of load cells had an impact on the behavior of the specimens. Consequently, a comparative analysis of the models was conducted, both with and without ball bearings, and it was determined that the model incorporating ball bearings provided results more closely aligned with experimental measurements. Thus, ball bearings were designed and included as simulation components to match experimental results more closely.

4.2.2 Material property of components

The CLT panels were constructed with 38mm x 140mm (2 in x 6 in) Spruce-Pine-Fir (SPF) lumber. CLT type 175V belongs to V2M1.1 grade, while types 87V and 139V belong to grade V2.1 (See Table 6, Structurlam 2020). According to Table 7 of Structurlam (2020), V2M1.1 grade consists of SPF No.2 lumber in both longitudinal and transverse layers, whereas grade V2.1 has SPF No. 2 grade lumber in longitudinal layers and SPF No. 3 grade lumber in the transverse layers. In this study, all lumber was assumed to be SPF No.2 grade lumber for longitudinal and transverse laminates for both V2.1 and V2M1.1 CLT. This assumption was adopted to simplify modelling, since it was observed that using SPF No.3 lumber properties for transverse layers did not show any significant difference in results. The finite element models created in this study were built using solid modelling as the basis. Nodes and elements were generated from solid models based on geometric shapes specified by the users. Solid volumes are made from linear elastic orthotropic materials using engineering constants, which has three moduli of elasticity (E), three shear moduli (G), and three Poisson's ratios (v).

In this study, lodgepole pine, which is one of the individual species within the Spruce-Pine-Fir (SPF) species combination, was assumed for the purpose of material property inputs in the FE models. The modulus of elasticity in the longitudinal direction (E_L) for grades V2.1 and V2M1.1 was assigned the same for SPF No.2 grade lumber i.e., 9500 N/mm^2. Figure 4.2 defines the radial and tangential directions relative to growth orientation in a cross section of lumber. In this study, however, the properties along the wider dimension of a cross section were assumed to be those corresponding to the tangential properties. Similarly, the radial direction is assumed to align with the smaller dimension of the cross section.

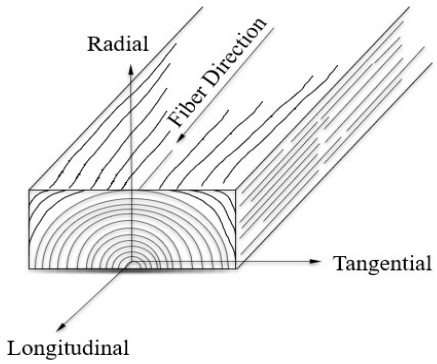

Figure 4.2. Axes of growth rings and grain direction in wood (Wood Handbook (2021))

The values for moduli of elasticity, shear moduli, and Poisson's ratios were obtained from the Wood Handbook (US FPL 2021) assuming the wood is lodgepole pine. Table 5.1 of the Wood Handbook (US FPL 2021) shows the elastic ratios for various species at approximately 12% moisture content, in which the values for the moduli of elasticity and shear moduli for lodgepole pine can be calculated. Furthermore, Table 5.2 of the Wood Handbook (US FPL 2021) provide three Poisson's ratio values for this species. The material properties for lumber in CLT tested in this study are presented in Table 4.1.

Table 4.1. Material properties of CLT lumber

Modulus of Elasticity (N/mm^2)			**Poisson's ratio (-)**			**Shear Modulus (N/mm^2)**		
L*	**R***	**T***	**LR**	**LT**	**RT**	**LR**	**LT**	**RT**
9500	**969**	**646**	**0.316**	**0.347**	**0.469**	**466**	**437**	**48**

* L: Longitudinal, R: Radial, T: Tangential

The steel material was assumed to be isotropic with a modulus of elasticity of 200GPa and a Poisson's ratio of 0.3. Linear elastic behavior was assumed in the analyses.

4.2.3 Interaction and constraints

Each surface that may come into contact with another should be defined as a contact. Surface-to-surface contact was applied to adjacent longitudinal and transverse laminates. Hard contact was defined between adjacent laminates (edge-to edge contact), allowing solid-material interactions to be modeled effectively. In other words, when the slave surface is in contact with the master surface at the constraint points, the pressure-overclosure relationship (hard contact) minimizes penetration. Additionally, friction between edges of adjacent lumber pieces laminate was ignored. Steel plates attached to CLT panels were subjected to fully constrained contact behavior (tie). The lower steel plates were also connected to the ball bearings using this constraint. Layers were tied together in this simulation (face-to-face contact) since the bond between layers was assumed to be rigid. The tie constraint was formulated as a master-slave relationship. Constraints prevent slave nodes from separating or sliding away from the master.

4.2.4 Loading and boundary conditions

In the FE models, boundary conditions were applied to simulate the conditions in the test set-up. To this end, displacement constraints were applied to the appropriate supporting nodes. Figure 4.3-(a) shows the coordinate axes of the CLT panel in this FE model. To ensure accurate measurement of compression load by the load cells, it is essential to provide freedom of movement in the y-direction while constraining all other degrees of freedom. Based on the experiments, the bottom of the ball bearings represents the bottom support. Because of this, the bottom of the ball bearings are constrained from movements in all directions (X-Y-Z). The rotational degrees of freedom of the ball bearings' end were set to be free about the X,Y and Z axes. This displacement constraint is shown in Figure 4.3-(b) at the bottom of the ball bearings.

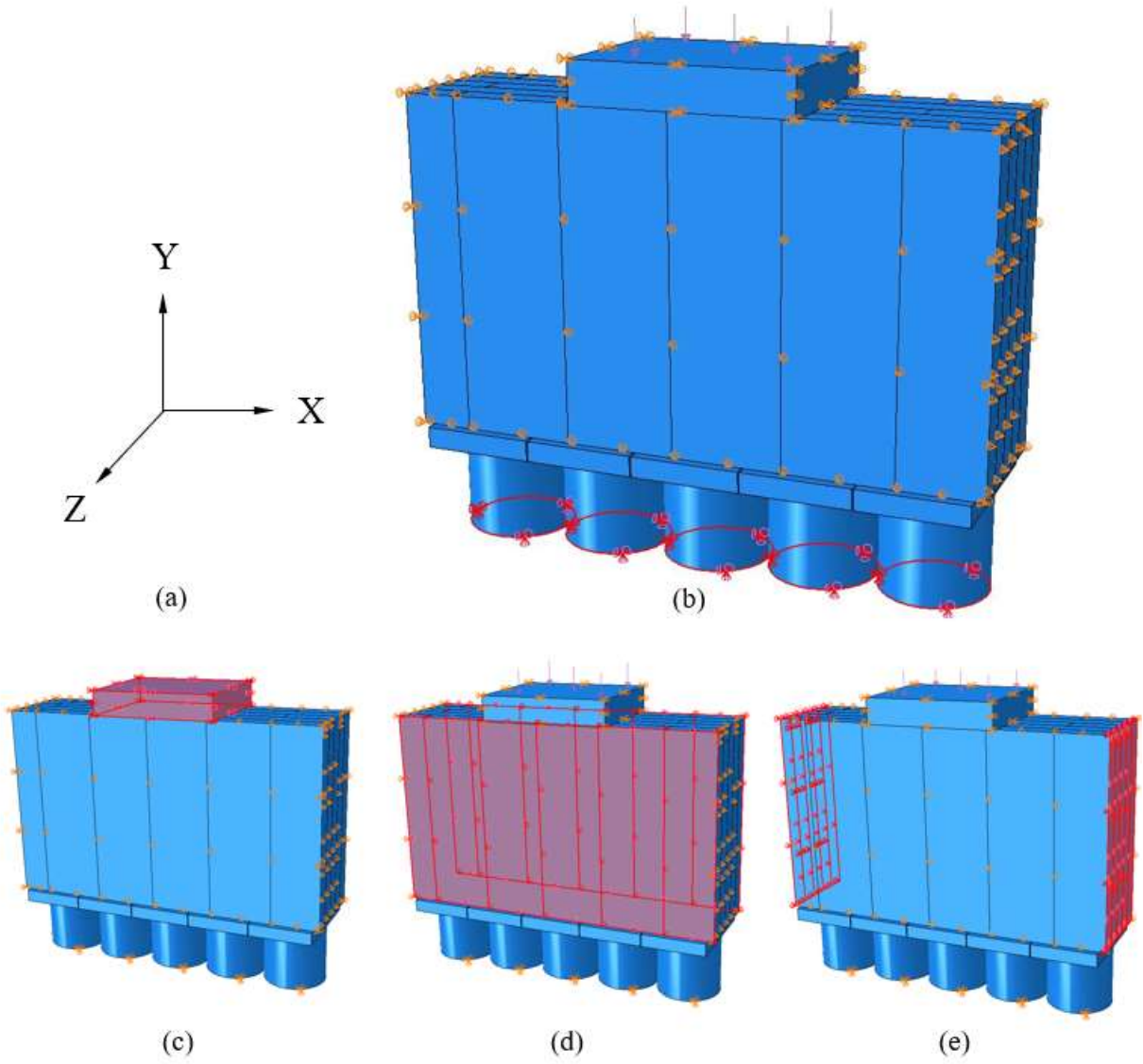

Figure 4.3. Structure of FE models with loading and boundary conditions

Since the loading method is force control, the upper steel plate is subjected to a static uniform load. This load is applied to the top of the geometric face of the upper steel plate (purple arrows, Figure 4.3-(b)). In order to prevent movement of the upper steel plate during the loading procedure, its movement is constrained in the X and Z directions (Figure 4.3-(c)). Therefore, translational loading can be performed on the Y-axis. For buckling prevention, CLT panels are constrained on XY and YZ planes on both sides (Figure 4.3-(d-e)).

4.2.5 Meshing

Mesh refinement is essential for achieving optimal accuracy in finite element modelling. Not only does mesh density affect accuracy, but it also affects computational processing time. Although smaller meshing sizes usually produce more precise results, the computation time increases. For this reason, several mesh densities were assessed to determine the optimum mesh size. A CLT type C specimen as outlined in Table 3.1, was selected for analysis. The upper steel plate had dimensions of 260mm in length, 200mm in width, and 50mm in thickness. A compression load of 1150 kN was applied, and the total displacement of the CLT between the upper steel plate and the middle lower steel plate was measured for the selected mesh sizes. Figure 4.4 illustrates the sensitivity of the model prediction to mesh size.

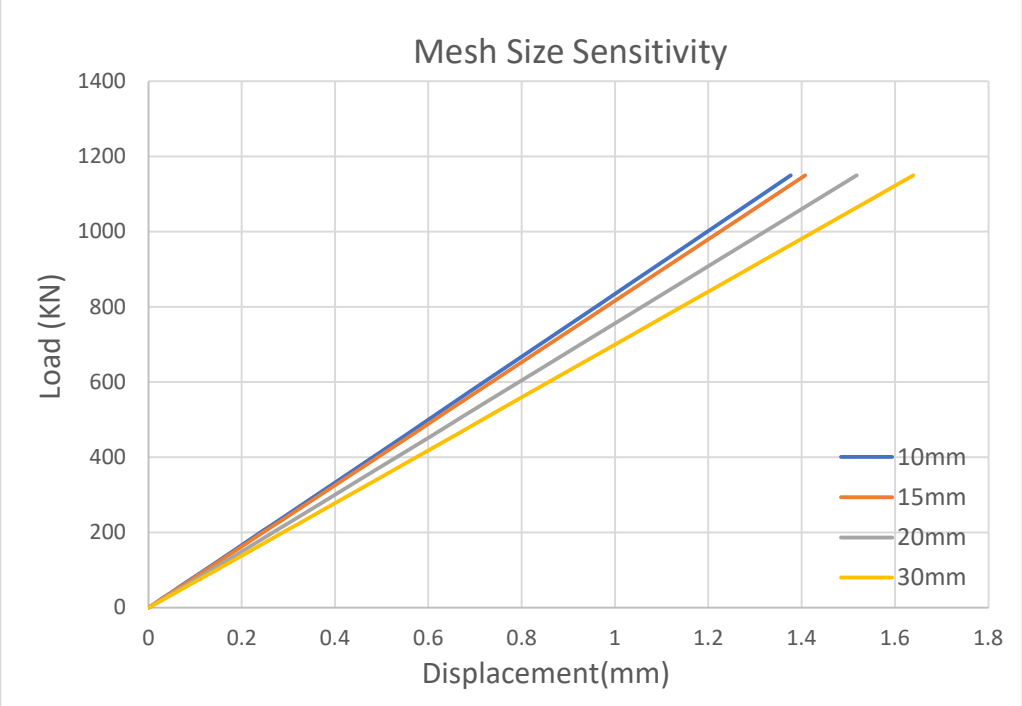

Figure 4.4. Mesh size sensitivity

Mesh convergence refers to the extent to which the elements need to be reduced in size to ensure that changes in the mesh size do not significantly impact the results of the finite element analysis. Figure 4.4 visually demonstrates the convergence of results, as the influence of mesh sizes (10 mm and 15 mm) on the obtained results is found to be negligible. Moreover, the computational time for the 10 mm mesh size was only slightly longer compared to the model with a mesh size of 15 mm. Therefore, a uniform mesh size of 10 mm was selected for all models.

For all the components, the mesh-dependent method was used. The mesh-dependent and mesh-independent methods in Abaqus are used to evaluate the accuracy and reliability of numerical simulations. A mesh-dependent method depends on the quality and refinement of the finite element mesh to provide accurate solutions. This means that the results of the simulation will be influenced by changes in the mesh. Meanwhile, mesh-independent methods are those in which the accuracy of the solution is unaffected by the mesh refinement. The simulation employed the mesh-dependent method, which was chosen due to its two primary advantages. Firstly, the mesh size directly affected result accuracy. Secondly, the presence of multiple laminates in the model allowed for easy replication, simplifying the manufacturing process through the utilization of the mesh-dependent approach. Figure 4.5 shows the FE model with a uniform mesh size of 10 mm.

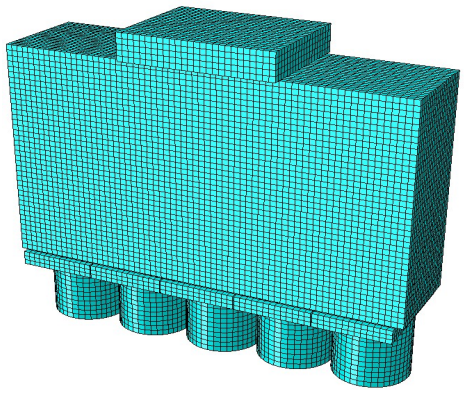

Figure 4.5. FE model with uniform mesh size of 10 mm

4.3 Validation of FE model

The model results should be verified with the test results to provide confidence in the modelling approach. The following step involves plotting and analyzing data collected from the test program and from FE modelling. Comparison of the results from the 18 laboratory tests and the corresponding predictions from the FE models confirms the validity of the models, as will be discussed later.

To ensure accurate comparison with test measurements, a reference line was assumed to be 200mm away from the top of the CLT specimen, as shown in Figure 4.6. This distance was chosen to achieve a more uniform distribution and to prevent load influence. Based on this reference line, strain and displacement behaviour were obtained for both FE models and DIC images. Figures 4.7, 4.8, 4.10, and 4.11 display the results based on this reference line. The gauge length of 200mm was used for comparing the results between the test, DIC, and FE model, as demonstrated in Figures 4.9 and 4.12. All figures display the results of specimens A-3 and B-5, while the remaining specimens' comparison results are presented in Appendix A. Finally, the comparison between DIC and FE modelling data confirmed the model's prediction capability when the specimen is subjected to an in-plane concentrated compression load.

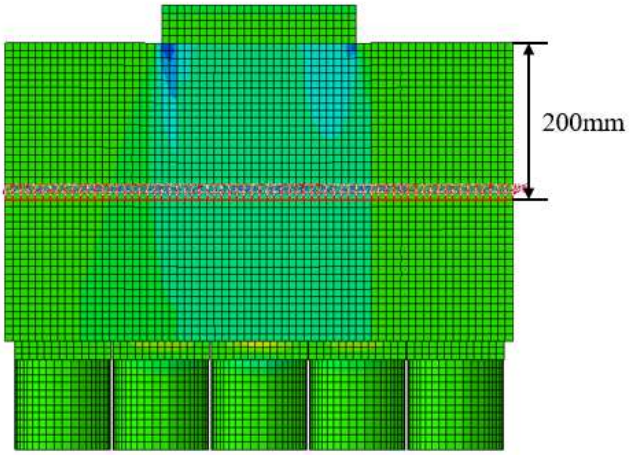

Figure 4.6. The location of the reference line selected in DIC and FE models to obtain the uniform distribution

Vertical displacement contour plots and plots of displacement along the length of the specimen are shown in Figures 4.7 and 4.10, while normal strain in the y direction of the specimens is shown in Figures 4.8 and 4.11. In addition, the load-displacement plots from the DIC images, FE models, and LVDTs in three locations of specimen (center, right and left) can be observed in Figures 4.9 and 4.12. The top and bottom dashed lines in the contour plots depict the gauge length of the LVDTs.

The displacement color contour plots for DIC and FE figures are expressed in mm. Since DIC contour plots present strain values as Lagrange strain tensors, the strain values in the legends for the DIC contour plots are almost half of the strain value for FE contour plots. The color contour plots of DIC and FE models generally agree fairly well in all the specimens. DIC and FE distributions both clearly show the effect of gaps between laminates. In both strain and displacement plots, sudden rises and falls in trends indicate the position of gaps near the loading area. There are noisy trends in the DIC patterns, while smooth trends are evident in FE distributions. High strain and displacement zones are located under the loading area in all specimens.

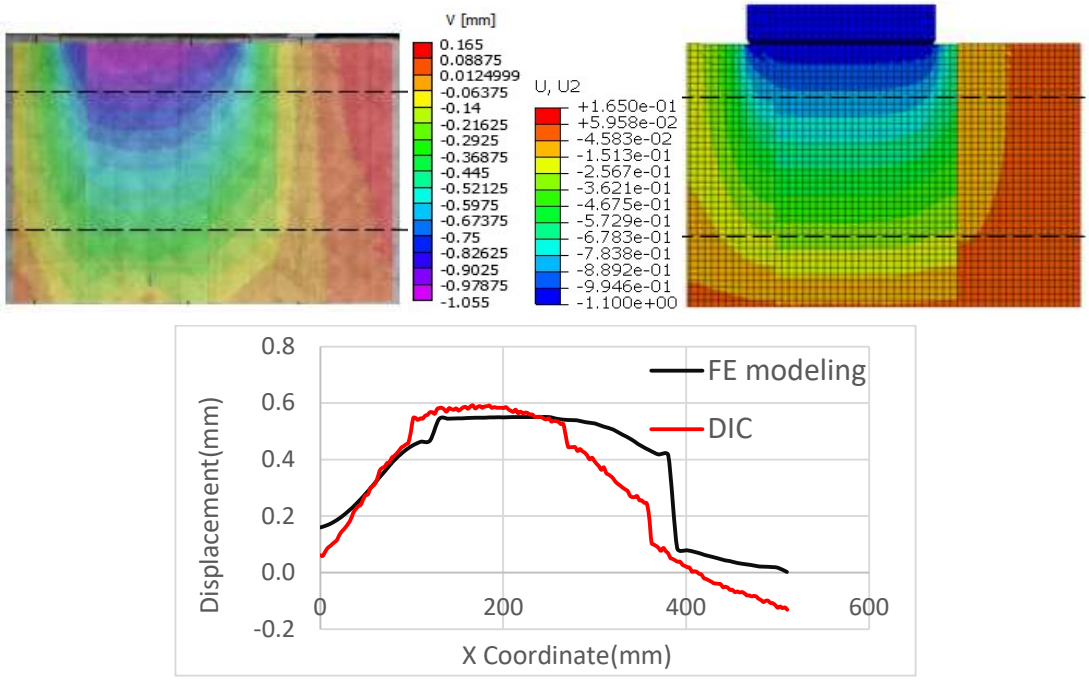

Figure 4.7. Displacement contour plots and displacement graph from compression test at 80% of failure load for specimen A-3- DIC (left), FE modelling (right)

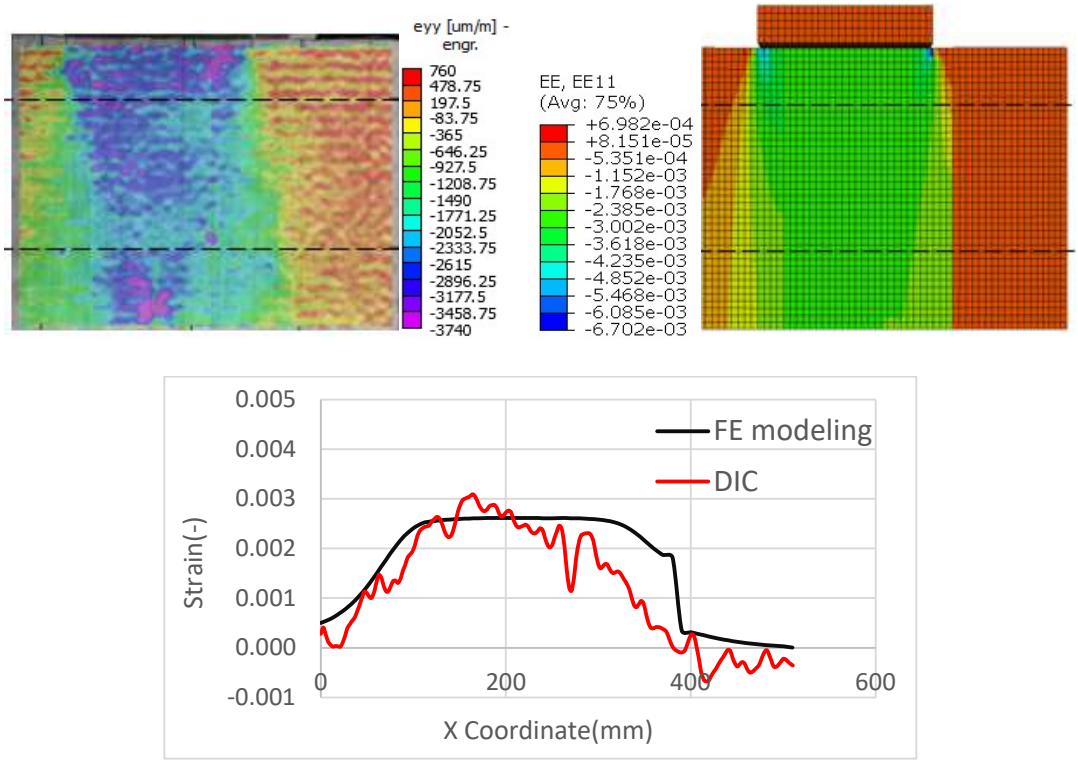

Figure 4.8. Normal strain contour plots and normal strain graph in the y direction from compression test at 80% of failure load for specimen A-3- DIC (left), FE modelling (right)

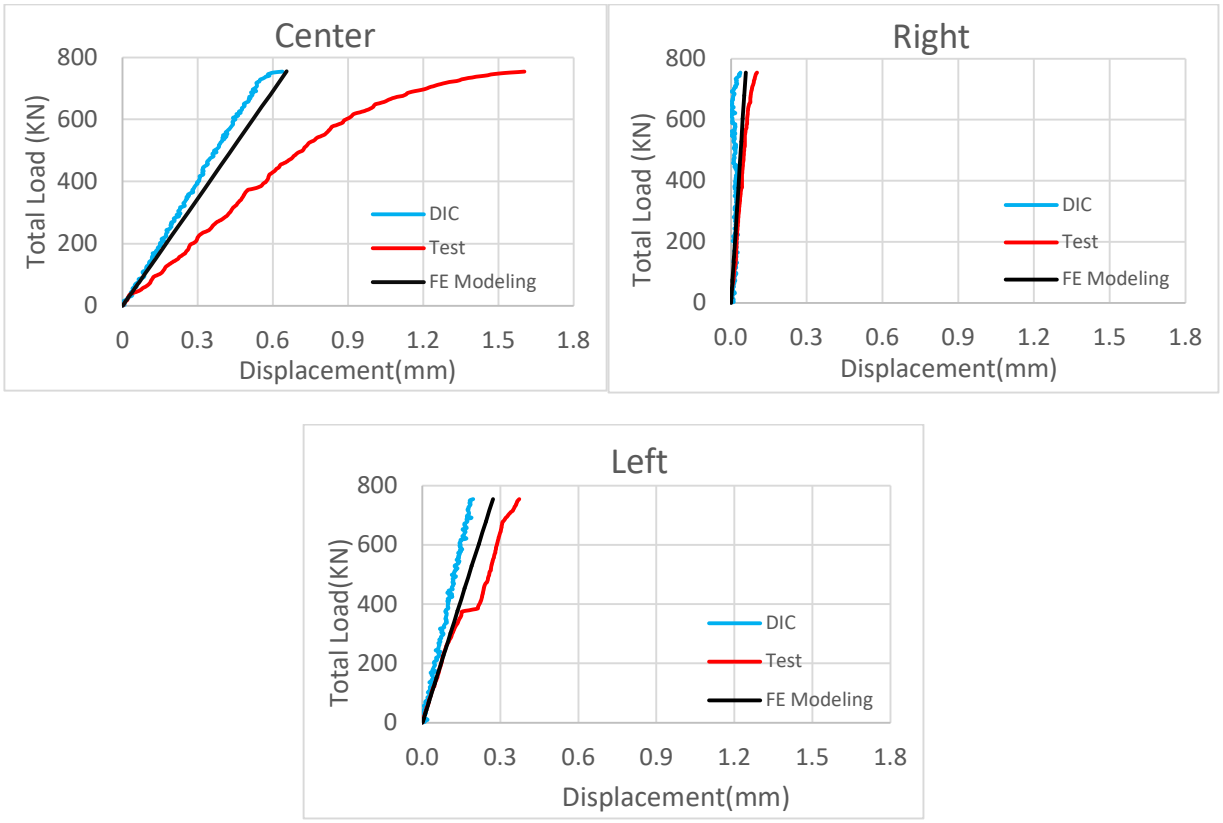

Figure 4.9. DIC, Test and FE modelling results for specimen A-3 until failure

In specimens where the loading area was placed on two gaps, the strain distribution was wider. However, in specimens where the loading was placed on three gaps, the strain distribution was tighter.

As A-3 is not a symmetric specimen, its distribution is not symmetric. Strain and displacement contour plots from DIC and FE model show reasonable agreement. A similar distribution pattern can also be observed between the DIC and FE figures in this specimen. According to both DIC and FE figures, the displacement shape looks like nested semi-circles under the loading area, and the high deformation zone occurs just under the steel plate (Figure 4.7). As shown in Figure 4.8, the high strain distribution also begins under the steel plate and gradually decreases to the edge of the CLT panel. Figure 4.7 shows that as the distribution approaches the gap on the half-right side of the specimen, the gap has a dramatic effect on the strain. The displacement shape and strain

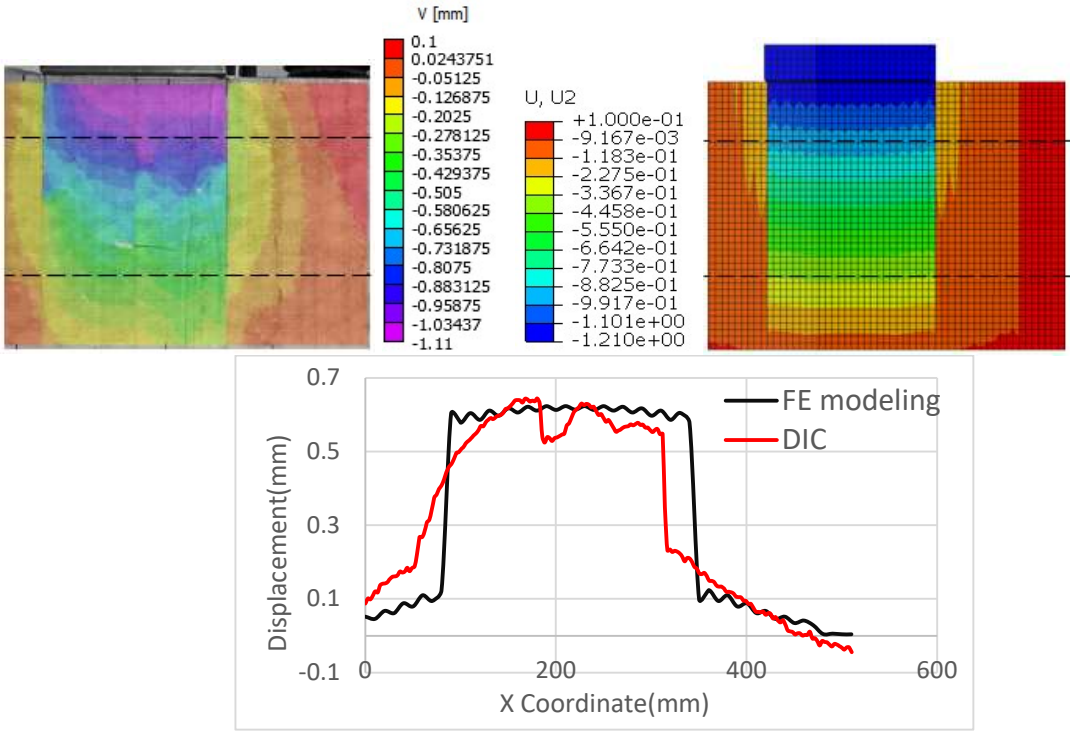

Figure 4.10. Displacement contour plots and displacement graph from compression test at 80% of failure load for specimen B-5- DIC (left), FE modelling (right)

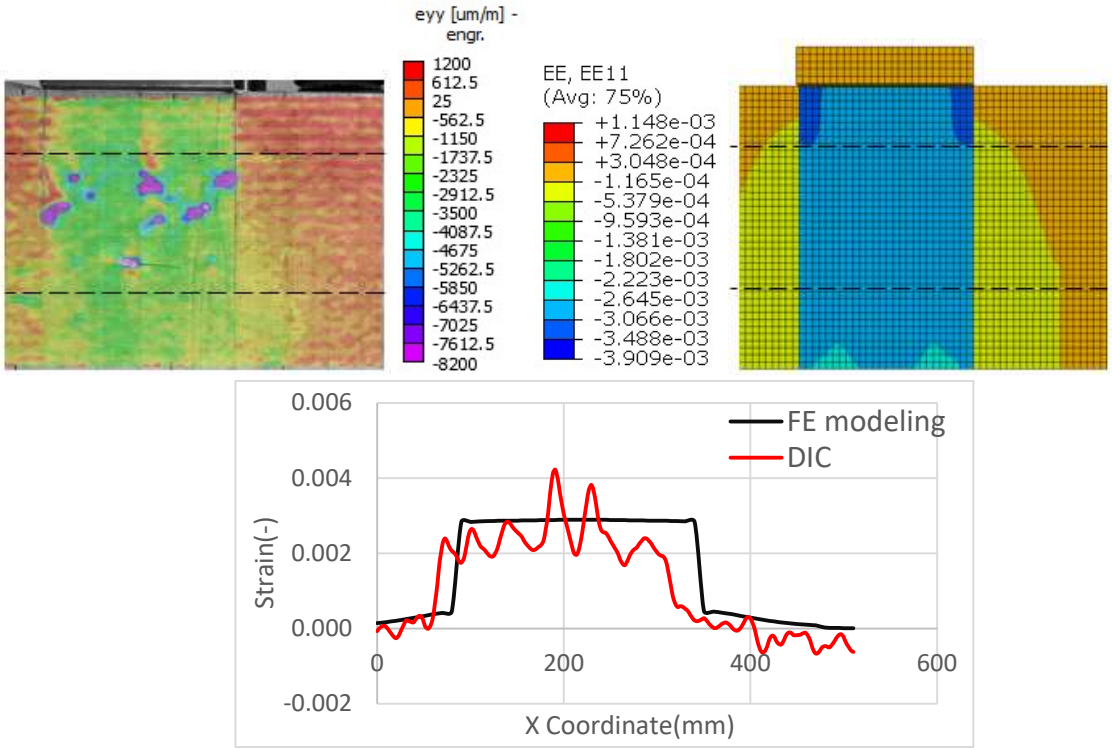

Figure 4.11. Normal strain contour plots and normal strain graph in the y direction from compression test at 80% of failure load for specimen B-5- DIC (left), FE modelling (right)

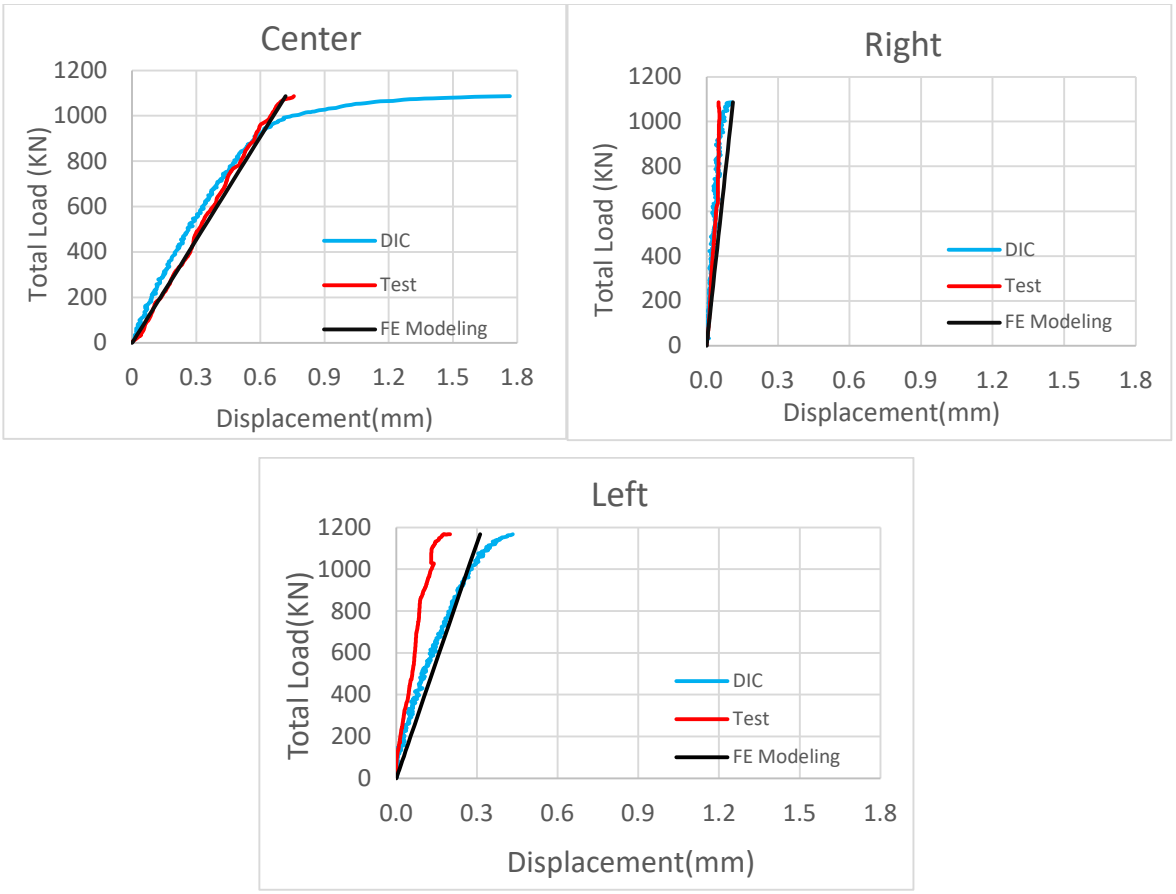

Figure 4.12. DIC, Test, and FE modelling results for specimen B-5 in the failure mode

distributions are different when the loading area is placed on top of two laminates and entirely between two gaps (specimen B-5).

It is noted that the DIC and FE figures show a symmetric shape due to the symmetric specimen. Similar to A-3, the high displacement zone can be seen under the steel plate, and it reduces towards the bottom and sides of the CLT panel, but there is no evidence of semi-circular distributions (Figure 4.10). Under the loading area, specimen B-5 has a deeper and longer high strain zone than specimen A-3, resulting in a pronounced concentration of strain between two gaps. This behavior is also evident from the graphs, particularly in terms of the sharp rises and falls at the corresponding gaps. In fact, gaps prevent the strain from spreading to the edge of the CLT panel, meaning that most of the strain concentrates under the loading area.

As illustrated in the actual test setup shown in Chapter 3, the LVDTs were placed at three locations on the CLT specimen. Figures 4.9 and 4.12 show a comparison of the results from DIC, test, and FE modelling at these locations. In general, it can be said that the experimental and modelling results are well matched. Furthermore, since LVDT data were recorded from the back of the CLT panels, while DIC data were obtained from images taken from the front of the CLT panels, some deviation is expected. The right and left diagrams show remarkable agreement between DIC, LVDTs, and FE modelling results for both specimens. Nevertheless, specimen A-3 shows a deviation in the center load-displacement curve and specimen B-5 shows a plateau trend in DIC results. As mentioned above, the differences between DIC and LVDT readings were expected due to differences in wood properties, growth features and cracks on opposite sides of the specimens.

Figure 4.13 shows four graphs of the failure load for each specimen type (A-B-C-CH) at the 5 load cell locations. Appendix B contains the rest of the data. In these figures, the Y-axis indicates the load value, and the X-axis represents the five load cells placed under the CLT specimens.

Regarding specimen A-3, the load received by the center load cell of this 3-ply specimen was around 300 kN, while the load decreased toward the side of the CLT specimen to less than 50 kN. This specimen shows less than 5% discrepancy between the test and FE results, indicating that the model is accurate. Specimen B-5 exhibited comparatively less load spreading: more than 90% of the ultimate load was received by the three middle load cells (LC-2, LC-3, and LC-4). The reason is that the loading area is positioned between two gaps. It means that most of the concentrated compression load was resisted by the elements directly under the applied loading area.

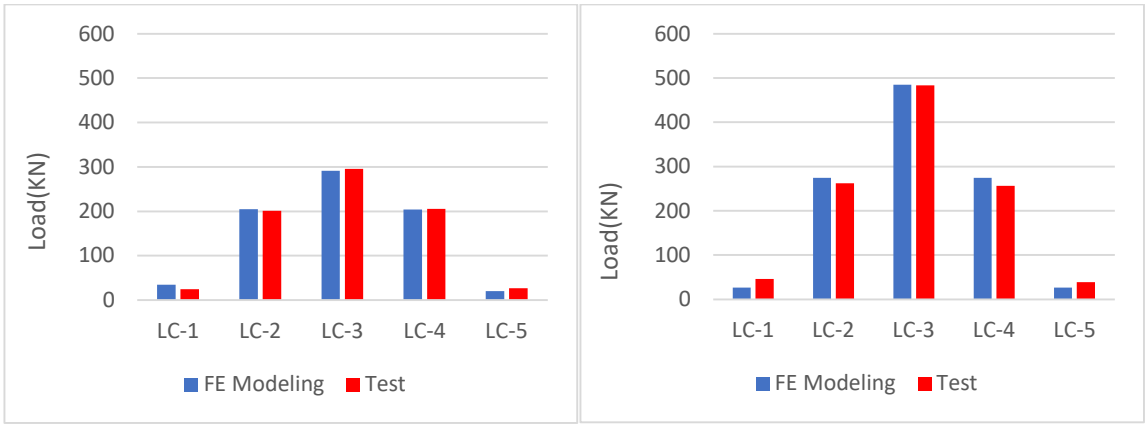

A-3-3ply-87V

B-5-5ply-139V

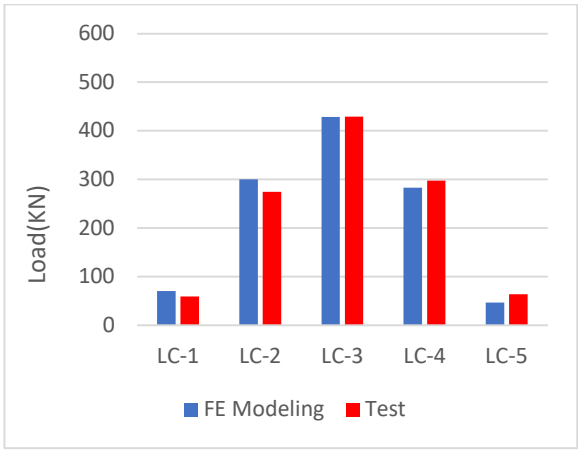

C-3-5ply-175V

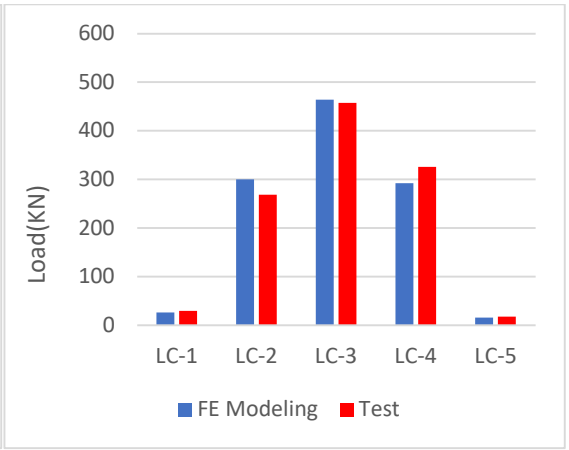

CH-1-5ply-175V

Figure 4.13. The load distribution results of FE modelling and testing at failure.

It is generally observed that the load distributions in specimens are bell-shaped. This implies that LC-3 receives the maximum load and that the load decreases toward the side of the CLT specimen. The discrepancy between FE results and test results, as shown in the figures for C-3 and CH-1, reached around 10% for load cells LC-2 and LC-4, but the predicted loads are still in reasonable agreement with the measured load.

Chapter 5: Parametric Study

5.1 Introduction

The overarching goal of this study was to develop design information that will allow engineers to determine how an in-plane compression load applied to the edge of a CLT panel is transferred through the height of the panel, referred to here as the load spread angle. In this study, three influential parameters are evaluated using the developed FE model: the aspect ratio of CLT (h/w), the ratio of loading area width to panel width (a/w), and the ratio of total transverse layer thickness to total CLT thickness. This chapter is primarily concerned with investigating the effects of these parameters on the in-plane behaviour of CLT panels under a compression load applied to the edge of CLT panel, eventually leading to the development of empirical equations to calculate the load spread angle based on these three parameters. Two load locations relative to the CLT panel length are considered: the load applied in the middle and load applied near the edge of the CLT panel.

5.2 Studied parameters

Figure 5.1 shows the three parameters investigated in this parametric study: 1. Ratio of loading area width to panel width (a/w); 2. Ratio of height to panel width (h/w); (3) Transverse layer percentage.

5.2.1 Ratio of loading area width to CLT panel width (a/w)

In practice, a point load is essentially a distributed load applied uniformly over a finite width. In Chapter 4, it was noted that the configuration of the loading area affects the load distribution and the load spread angle. It is therefore of interest to study the ratio of loading width, a, over the CLT panel width, w (Figure 5.1 (a)).

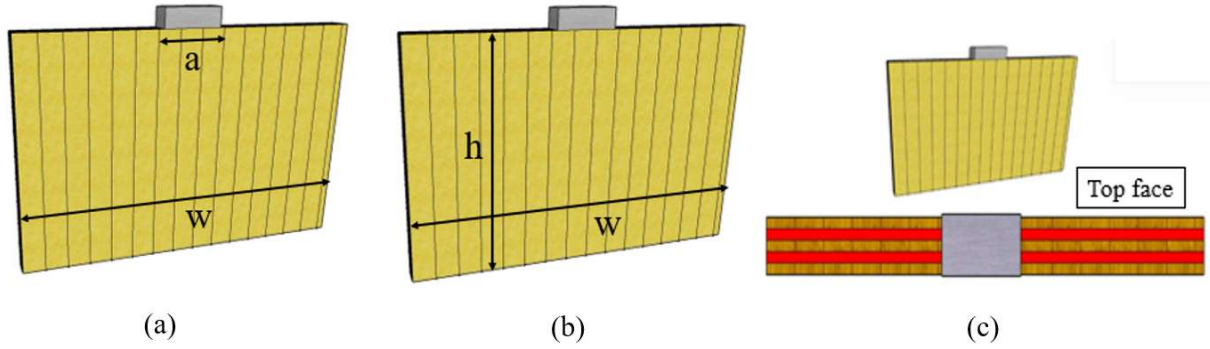

Figure 5.1. Schematic of three selected parameters (a) a/w (b) h/w (c) Transverse layer percentage

5.2.2 Aspect ratio of CLT panel (h/w)

The aspect ratio of cross-laminated timber (CLT) panels, defined as the ratio of height to width, can have an impact on how the applied load is distributed along the height of a CLT specimen. Even though the laboratory tests presented in Chapter 3 show minimum sensitivity, due to the limited range of specimen geometries tested, further evaluation of this parameter through FE modelling is necessary. Thus, investigating the relationship between the height-to-width ratio of CLT panels and their structural behaviour may provide valuable insights into their design and performance (Figure 5.1-(b)).

5.2.3 Percentage of transverse layers

Figure 5.1-(c) shows the transverse layers of CLT panels as two interior layers marked with red rectangles. Previous work by Gräfe et al. (2018) showed that the percent transverse layer thickness relative to the total CLT thickness influences the load spread angle. Transverse layer percentage was therefore selected as a parameter for investigation in this study.

5.3 Load spread angle and effective length calculation

Results from the test program discussed in Chapter 4 showed that the load distribution in CLT panel under compression loading is not linear. The highest stressed zone is directly under the loading area, and decreases rapidly at first, with more gradual change observed further away from the loading area. Due to the gradual reduction after the initial rapid reduction, the zero-load location could be far from the origin. Therefore, defining the load spread angle using the zero-load point would be unrealistic. Instead, in this study, the load spread angle is defined as the angle between the vertical and the line connecting the edge of the load area at the top to a bottom location that corresponds to the 2.5% exclusion limit of the load distribution curve, as illustrated in Figure 5.2(a). With this approach, 95% of the total applied load is considered to be resisted by the CLT, and the distance between the lower 2.5% and upper 2.5% exclusion limits is defined as the effective length that effectively reacts against the applied load. As shown in Figure 5.2-(b), the actual load spread angle of CLT panels can be found by using the following formula:

$$\alpha = \arctan\left(\frac{S}{h}\right) \tag{5-1}$$

where α is the load spread angle, h is the height of CLT panel, and S is the horizontal distance between the edge of the load area and the nearest 2.5% exclusion limit. Figure 5.2-(d) shows that the effective length's definition differs when the load is applied on the CLT panel's side. With this approach, the effective length definition refers to the distance between the side of the CLT panel to 5% of the exclusion limit, indicating 95% of the total applied load, as shown in Figure5.2-(e). The load spread angle can then be derived from Equation 5.1. Figure 5.2-(c-f) shows the stress contour from FE modeling, indicating the concentration of applied stress under the applied load in the loaded laminate and the adjacent ones.

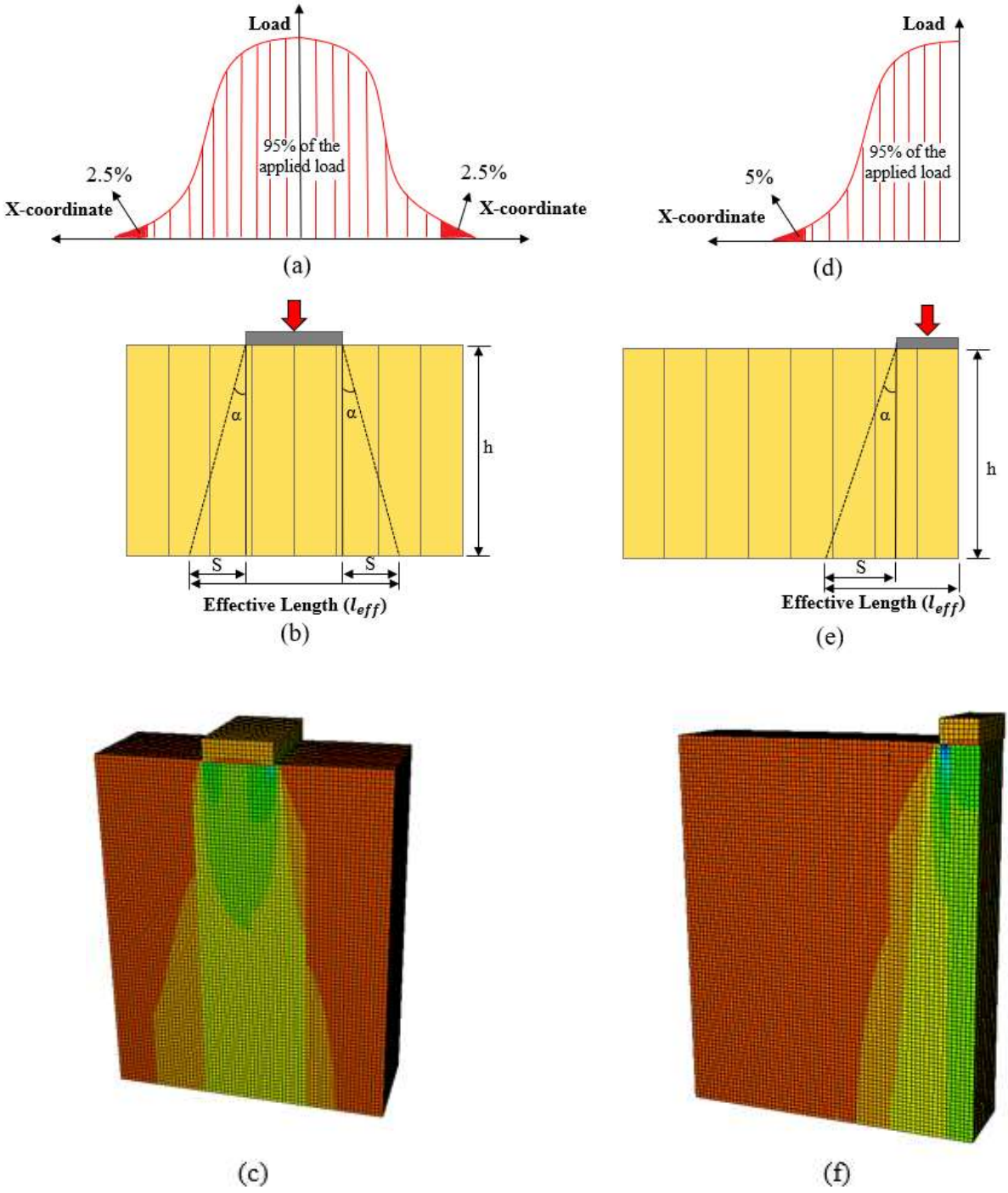

Figure 5.2. Load spread angle definition: (a,d) Actual load distribution, (b,e) Equivalent linear load distribution, (c,f) Stress distribution of FE model

5.4 Results and Discussion

In this section, the results from the parametric study are presented and the impacts of each parameter on the load spread angle discussed. Subsequently, two empirical equations are presented to estimate the load spread angle based on the three studied parameters.

5.4.1 Load spread angle

This section shows how the selected parameters affect the load spread angle separately. Based on the results, the most critical parameter can be determined, which can effectively explain the panel behaviour under concentrated compressive load. A model matrix and the individual load spread angle results for each parameter are shown in Tables 5.1 to 5.3.

5.4.1.1 Influence of the ratio of load area width to the width of the CLT panel

This parameter is investigated in 12 models including four different a/w ratios (0.24, 0.29, 0.35, and 0.38) in three different aspect ratios (h/w) when the load applied in the middle of CLT panel as shown in Table 5.1. These (a/w) ratios were selected by increasing the width of loading area (a) from 160mm to 260mm and keeping constant the CLT panel width at 680mm. These ratios encompass a wide range of applied point loads to CLT panels under compression, considering their widths and positions relative to the lamination gaps. By using a diverse set of ratios, the results can offer valuable insights into the behaviour of CLT panels under a range of realistic loading conditions.

As illustrated in Figure 5.3, the load spread angle (α) decreases gradually by about 3° when the a/w ratio increases from 0.24 to 0.38. To assess the reproducibility of this pattern, three different aspect ratios were taken into account. Similar patterns were observed at different aspect

Table 5.1. Model matrix and the load spread angle results for variation in a/w

Model	CLT Thickness(mm)	Lay up (layer thickness)	h/w	a/w	Load spread angle (°)
1	175	35-35-35-35-35	0.59	0.38	11.5
2				0.35	13.9
3				0.29	14.1
4				0.24	15.1
5	175	35-35-35-35-35	0.88	0.38	12.4
6				0.35	13.3
7				0.29	14.2
8				0.24	15.7
9	175	35-35-35-35-35	1.25	0.38	10.8
10				0.35	12.0
11				0.29	12.6
12				0.24	13.8

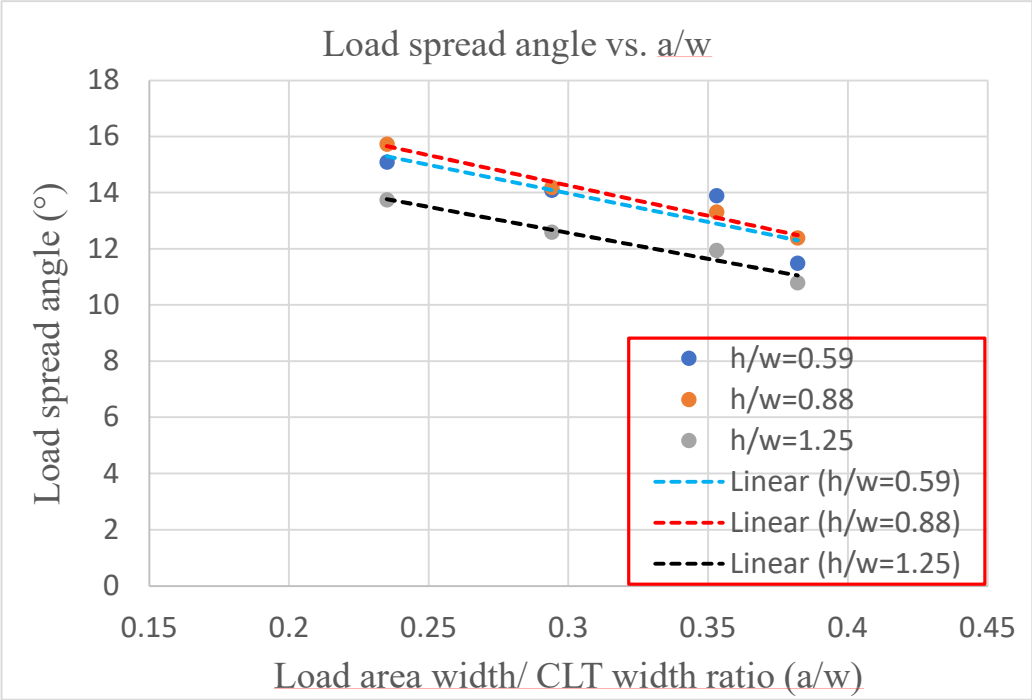

Figure 5.3. Load-distribution angle as a function of the width of loading area to the width of CLT panel ratio in three different aspect ratios

ratios. As can be seen, the trend lines for 0.59 and 0.88 aspect ratio panels show similar trends, while the trend line for the 1.25 aspect ratio panel shows a lower y-intercept, with slope similar to the other two panels. In general, the trend line representing the 0.88 aspect ratio exhibits the highest load spread angle, with some minor exceptions that can be attributed to numerical analysis complexities and finite element errors, potentially resulting from inadequate mesh alignment between the steel plate and panel laminations or unanticipated issues with the hard contact constraint. Furthermore, when the ratio of a/w is about 0.35 (length of steel plate is 240 mm), the edges of the loading area are further away from the lamination gaps, resulting in a greater spread of load and a larger load spread angle.

5.4.1.2 Influence of the aspect ratio of CLT panel

A total of 15 models with five different aspect ratios of CLT panels for 3, 5 and 7-ply CLT panels were examined to investigate the impact of CLT panel aspect ratio. The loading area width was 260 mm (a/w=0.38). Aspect ratios of 0.37, 0.59, 0.74, 0.88 and 1.25 were considered by keeping the width of the panel constant and increasing the height (Table 5.2). The selection of these aspect ratios was made with the intention of covering a diverse range of CLT panel configurations commonly used in construction, including CLT walls and deep beams.

Figure 5.4 shows the change in load spread angle with CLT panel aspect ratio. In general, the same pattern is observed for CLT with different numbers of layers. The order of the response curves from top to bottom is 7-, 5- and 3-layer CLT. The pattern shows an upward trend at first as aspect ratio increases from 0.37 to about 0.74 and then slowly declines by about 2° at 1.25 after reaching a peak. For all three types of CLT panel, the peak occurs at an aspect ratio of 0.74.

Table 5.2. Model matrix and the load spread angle results for variation of h/w

Model	CLT Thickness(mm)	Lay up (layer thickness)	a/w	h/w	Load spread angle (°)
1	105	35-35-35	0.382	0.37	11.8
2				0.59	13.5
3				0.74	14.5
4				0.88	14.0
5				1.25	13.3
6	175	35-35-35-35-35	0.382	0.37	12.7
7				0.59	15.1
8				0.74	15.6
9				0.88	15.4
10				1.25	13.8
11	245	35-35-35-35-35-35-35	0.382	0.37	13.1
12				0.59	15.6
13				0.74	16.2
14				0.88	15.7
15				1.25	14.1

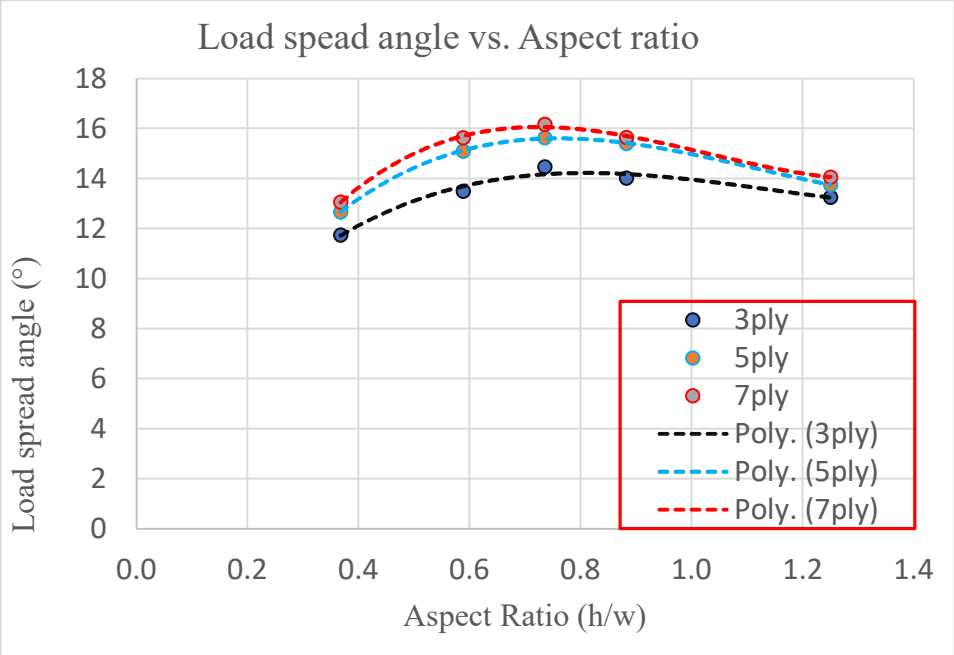

Figure 5.4. Influence of aspect ratio on load spread angle

Based on Figure 5.4, it can be anticipated that increasing the h/w ratio beyond 1.25 will reduce the load spread angle. In general, it can be noted that the load spread angle does not appear to be sensitive to CLT aspect ratio within the range studied here. When the aspect ratio is increased from 0.38 to the peak of 0.74 the change in load spread angle is only about 3° to 4 °, and between 0.38 and 1.25 aspect ratio the difference in load spread angle is only about 2 °.

5.4.1.3 Influence of percentage of transverse layers

Eighteen FE models with different percent values of transverse layers, 13%, 20%, 24.5%, 33%, 40%, and 50%, in three different aspect ratios, were developed to investigate the influence of the transverse layer percentage on load spread angle. The loading area width was kept constant at 0.38. The FE modelling matrix and results are summarized in Table 5.3.

According to Figure 5.5, the load spread angle increases linearly as the transverse layer percentage increases from 13% to 50%. This means that the compression load under a specimen with a higher transverse layer percentage is more evenly distributed than a specimen with a smaller transverse layer percentage. It can also be observed that increasing the aspect ratio of the CLT panel from 0.59 to 1.25 decreases the load spread angle.

Numerically, the load spread angle increases from almost 10 ° to 18 ° for the aspect ratio of 0.59, 12 ° to 17 ° for the aspect ratio of 0.88, and 12 ° to 14 ° for the aspect ratio of 1.25 when the transverse layer percent increases from 13% to 50%. In general, it can be noted that the load spread angle is sensitive to percent transverse layers in CLT.

Table 5.3. Model matrix and the load spread angle results for variation of transverse layer percentage

Model	a/w	h/w	Transverse layer percent (%)	Load spread angle (°)
1	0.382	0.59	13	9.9
2			20	12.3
3			24.5	12.6
4			33	14.7
5			40	15.1
6			50	17.6
7	0.382	0.88	13	12.3
8			20	13.8
9			24.5	14.0
10			33	14.9
11			40	15.7
12			50	16.8
13	0.382	1.25	13	11.9
14			20	13.0
15			24.5	13.1
16			33	13.5
17			40	13.8
18			50	14.3

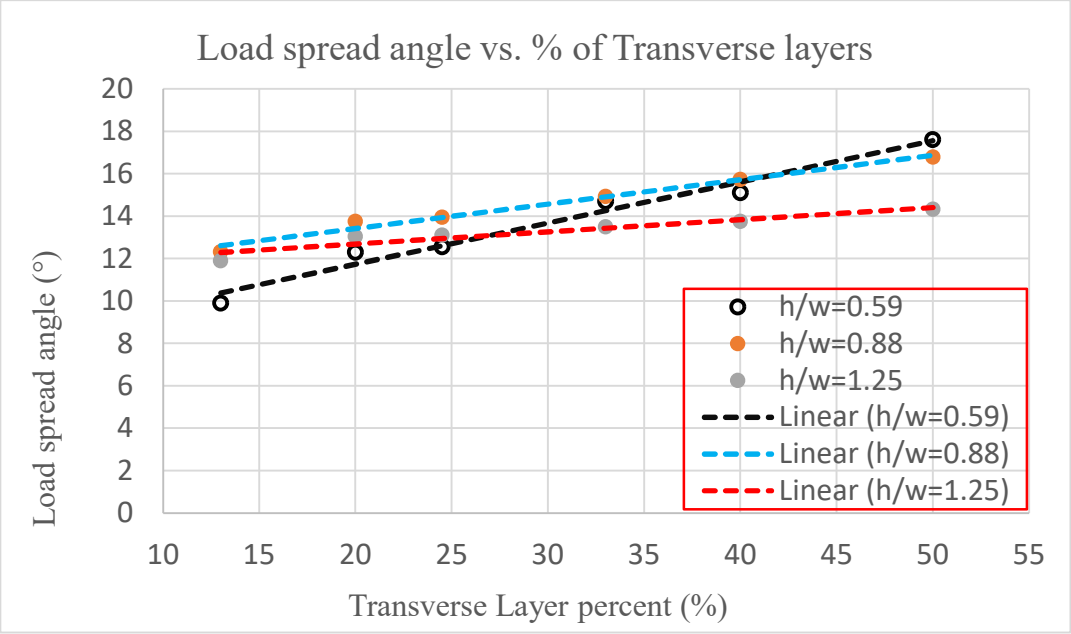

Figure 5.5. Influence of transverse layer percent on the load spread angle.

5.4.2 Derivation of empirical equations

One of this project's main objectives was to develop a design model that will enable designers to estimate the distribution of applied concentrated compression loads in CLT panels. This is the main reason for performing the parametric study, which would generate technical information for deriving an empirical model that could be used for design purposes. To this end, additional FE analyses were performed for two loading scenarios for the load applied at the middle and at the edge of the CLT panel, respectively. Table 5.4 shows the parametric study matrix of 5-layer CLT panels to derive the empirical equations. As shown in Table 5.4, the parametric study covers 108 configurations divided into two categories. In the first category, the load is applied in the middle of the CLT panels, while in the second category, the loading area is situated at the edge of the CLT panels, as illustrated in Figure 5.6. Four loading area width to specimen width ratios (a/w) were investigated in the first category (0.24, 0.29, 0.35 and 0.38) and two in the second category (0.12 and 0.18).

Table 5.4. Parameter study matrix to drive the equations

Parameter	**Value**					
h/w	0.59		0.88		1.25	
a/w	0.24	0.29	0.35	0.38	0.12*	0.18*
Transverse layer percent (%)	13	20	24.5	33	40	50

* Load applied at the edge of CLT

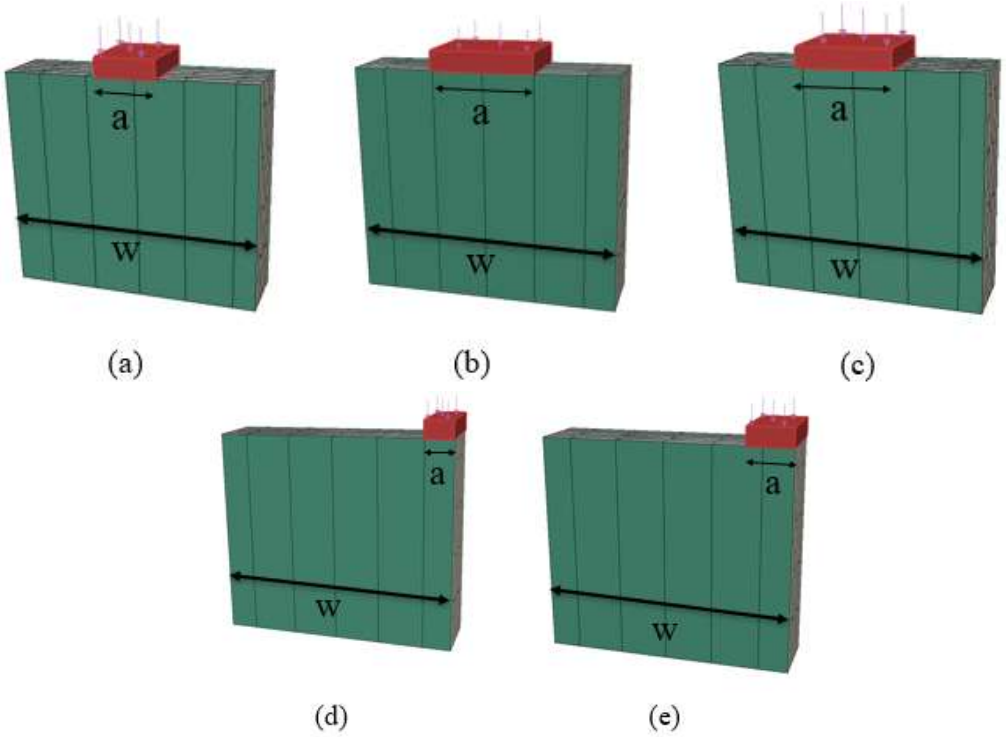

Figure 5.6. Load locations for studying the influence of loading area width and CLT panel width

In each case, the location of the loading area relative to the lamination gaps behavior was also investigated. For example, in Figure 5.6(b), the loading area intercepts two lamination gaps. In each case, the location of the loading area relative to the lamination gaps was examined. Figure 5.6(a) shows the loading area partially covering two laminates and intercepting only one lamination gap. Figure 5.6(b) shows the case that the loading area fully covers two laminates while in Figure 5.6(c), the loading area covers one laminate fully, two laminates partially, and intercepts two lamination gaps. In Figure 5.6(d), the load is applied between a gap and the side of the panel, while in Figure 5.6(e), the loading area fully covers one laminate and partially covers another laminate, intercepting one gap between the laminates. Three different aspect ratios (0.59, 0.88 and 1.25) were selected as illustrated in Figure 5.7. In addition, six different transverse layer percentages from 13% to 50% as illustrated in Figure 5.8 were included.

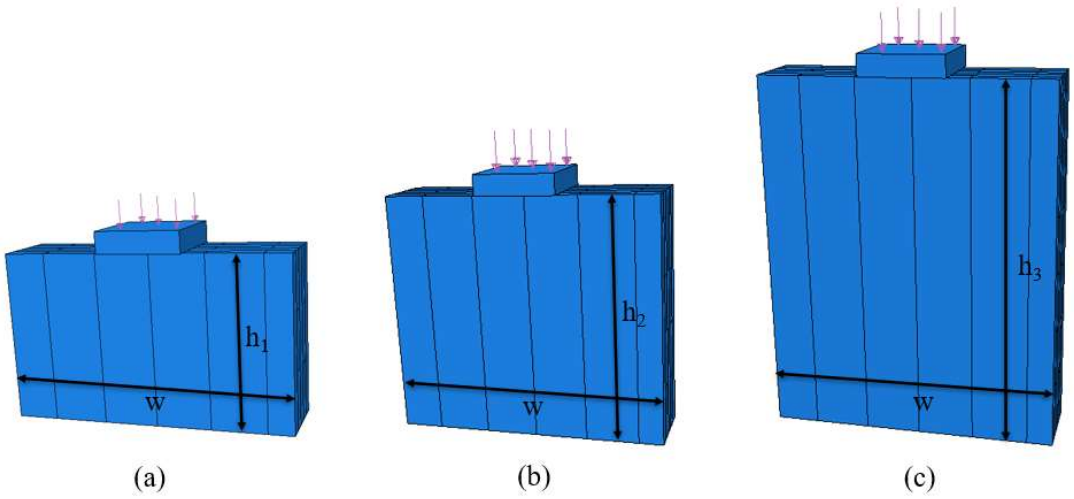

Figure 5.7. CLT panels with different aspect ratios

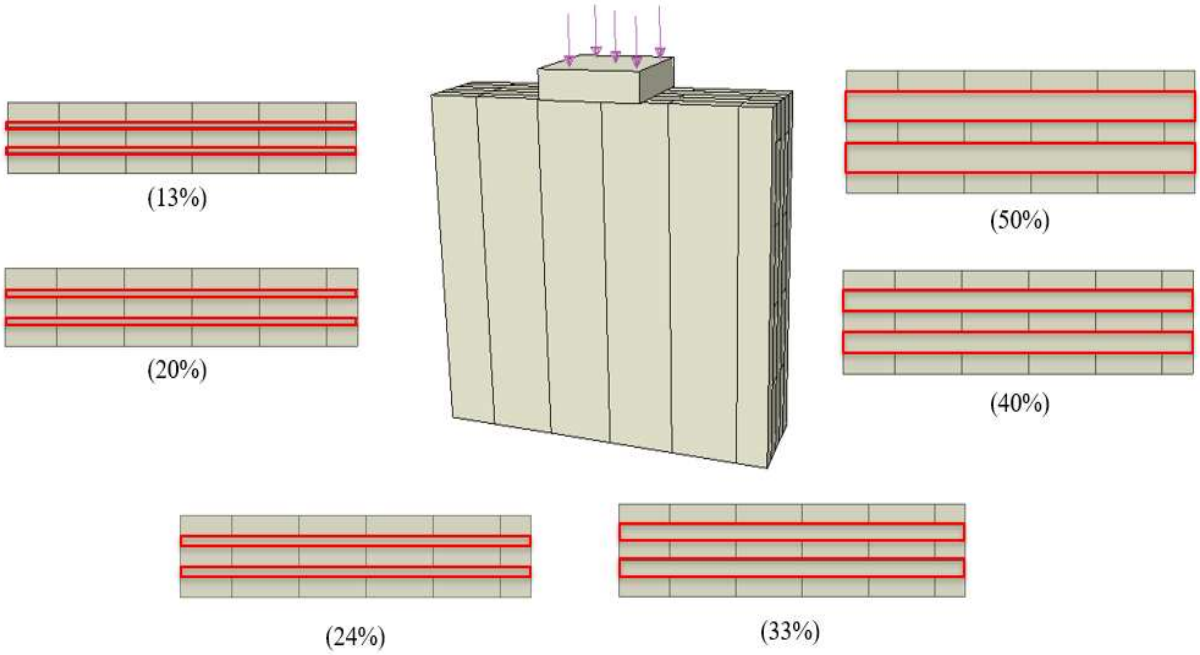

Figure 5.8. CLT panels with different transverse layer percent

In total 72 and 36 FE models were developed using ABAQUS software and analyzed for load applied at center and edge, respectively. The two loading modes examined in this study can be seen in Figure 5.9. Empirical equations were developed in this study using a commercial statistics analysis software, Stata (Stata Corp, 2015). The equations were verified by comparing the predicted and actual results. The actual results are derived from the analyses conducted via FE

modeling, whereas the predicted values are obtained using a multiple regression model developed with the values obtained from the FE model.

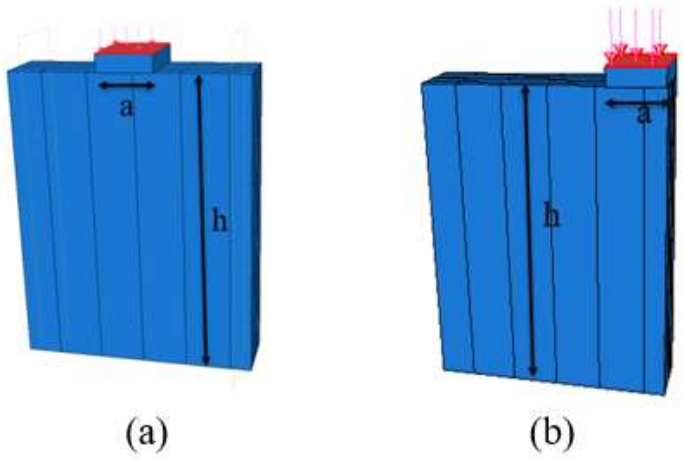

Figure 5.9. Loading configuration: (a) at the center of CLT panel, (b) at the edge of CLT panel

5.4.2.1 Category 1 - load applied in the middle of CLT panel

This category contains 72 FE models. Based on the results obtained from FE modelling, a multiple linear regression analysis was performed to develop the best-fit empirical model using Stata (2015). In the multiple regression analysis, the three independent variables are a/w ratio, h/w ratio and percent transverse layer, and the dependent variable is load spread angle. The following equation is derived for Category 1:

$$\alpha = 9.55\left(\frac{h}{w}\right)^{-0.03}\left(\frac{a}{w}\right)^{-0.46}p^{0.22} \qquad (5.2)$$

Where:

α = Load-spread angle

h/w = Height to width of CLT panel ratio

a/w = Width of loading area to width of CLT panel ratio

p = Percentage of transverse layers (%)

Table 5.5. Multivariate logistic regression results for category 1

Name of Variables	Effect size (95% CI)
h/w	-0.03 (-0.1, 0.05)
a/w	-0.46 (-0.58, -0.33)
Transverse layer percent	0.22 (0.17, 0.27)

According to Table 5.5, the h/w, a/w, and transverse layer percent coefficients were estimated to be -0.03, -0.46, and 0.22, respectively. For example, the a/w coefficient value (-0.46) suggests that, on average, for every one-unit increase in the ratio of height to width (a/w), the load spread angle decreases by -0.46 unit while holding other parameters constant. Furthermore, the a/w confidence interval range (-0.58, -0.33) indicates 95% confidence that a/w effect values are within this range. In addition, the adjusted R-square value for this equation is 0.65. Accordingly, the aspect ratio (h/w), the load application width to the width of CLT panel ratio (a/w), and the percentage of transverse layers can explain 65% of the variation in the load spread angle, adjusted for the number of parameters.

The effective length can be derived from the following relationship:

$$l_{eff} = a + 2S \tag{5.3}$$

Where:

a = Width of loading area

S = The horizontal distance between the edge of the load area and the nearest 2.5% exclusion limit

Equation (5.2) is applicable to the following ranges of the three parameters that were analyzed in this study:

$$0.5 < \frac{h}{w} < 1.25$$

$$0.2 < \frac{a}{w} < 0.4$$

$$0.1 < p < 0.5$$

A plot of the predicted and actual load spread angle in the first category is shown in Figure 5.10. The predicted values are calculated using multiple regression model developed based on the values provided by the FE model, whereas the actual values refer to the values provided by the FE models.

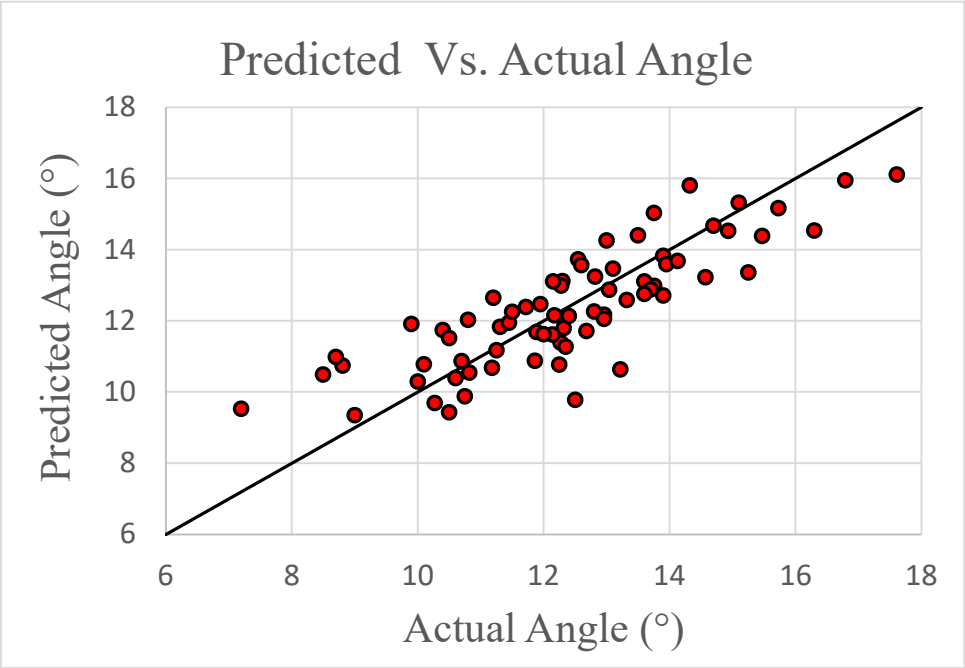

Figure 5.10. Predicted vs. actual angle for category 1

To visually evaluate the degree of agreement between the results predicted by the empirical model and the original values obtained from the FE analyses, a 45-degree line has been plotted on this graph.

In Figure 5.10, it can be seen that the empirical model provides a reasonable prediction of the load spread angle. In the worst-case scenarios, the difference between the predicted and actual degree was about 2°.

5.4.2.2 Category 2 - load application at the edge of CLT panel

In the second loading mode (Figure 5.9(b)), a total of 36 models were investigated. The same three parameters were treated as independent variables, and the same statistical analysis procedure was

applied to analyse the FE model results. The developed empirical equation for the case where the load is applied at the edge of CLT is shown in Equation (5.4).

$$\alpha = 21.09\left(\frac{h}{w}\right)^{0.22}\left(\frac{a}{w}\right)^{0.02} p^{0.28} \quad (5.4)$$

Where:

α = Load-spread angle

h/w = Height to width of CLT panel ratio

a/w = Width of loading area to width of CLT panel ratio

p = Percentage of transverse layers (%)

Table 5.6 shows that the h/w, a/w, and p coefficients were estimated to be 0.22, 0.02, and 0.28, respectively. Using the transverse layer percent coefficient (0.28) as an example, for every unit increase in the transverse layer percent, the load spread angle increases by 0.28 unit while keeping other parameters constant. It can be noted that the transverse layer percent effect values fall within the 95% confidence interval with the range of (0.23, 0.33).

Table 5.6. Multivariate logistic regression results for category 2

Name of Variables	**Effect size (95% CI)**
h/w	0.22 (0.15, 0.29)
a/w	0.02 (-0.085, 0.13)
Transverse layer percent	0.28 (0.23, 0.33)

The adjusted R-square value for this equation is 0.84. A highly adjusted R-square would result in all points being close to the regression line. Lower values correspond to weaker goodness of fit, indicating that the points are further from the regression line.

In this case, the effective length can be calculated from the following relationship:

$$l_{eff} = a + S \quad (5.5)$$

Where:

a = Width of loading area

S = The horizontal distance between the edge of the load area and the nearest 5% exclusion limit

According to Equation (5.4), the three parameters that were analyzed in this study fall into the following ranges:

$$0.5 < \frac{h}{w} < 1.25$$

$$0.1 < \frac{a}{w} < 0.2$$

$$0.1 < p < 0.5$$

The scatter plot presented in Figures 5.11 compares the predicted and actual values for category 2. A 45-degree line is plotted on each graph to provide a visual indication of the agreement between values predicted by the empirical mode and the original values provided by FE analyses. A good match between the predicted and actual values can be seen in Figure 5.11 for the load spread angle. It can also be observed that the largest discrepancy between predicted and actual values was about 1.5° to 2°.

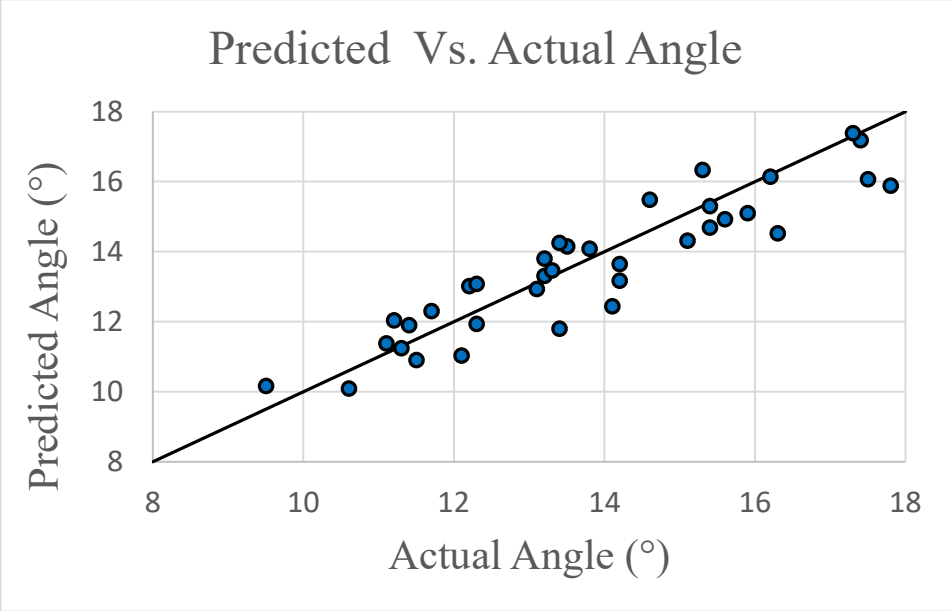

Figure 5.11. Predicted Vs. Actual angle for category 2

5.4.3 Maximum compression stress analysis

When considering a CLT panel under in-plane compressive loading, the maximum stress occurs within the loading area. Designers should compare this maximum stress with the material resistance specified in design standards.

For designing the supporting member or assembly beneath a CLT wall panel, the maximum compression stress at the bottom of the panel needs to be evaluated. When subjected to an in-plane concentrated compressive load, the resulting compression stress distribution at the bottom of the panel exhibits a bell-shaped curve. To simplify the design process, an equivalent rectangular mean stress is assumed. Figure 5.11 illustrates the actual compression stress distribution at the bottom of the CLT panel (indicated by the green arrows), and the gross mean stress distribution (depicted by the red arrows). A compression stress modification factor (K) is utilized to establish the relationship between the maximum stress and mean stress, calculated as the ratio of the maximum to the mean compression stress ($K = \frac{\sigma_{max}}{\sigma_{mean}}$).

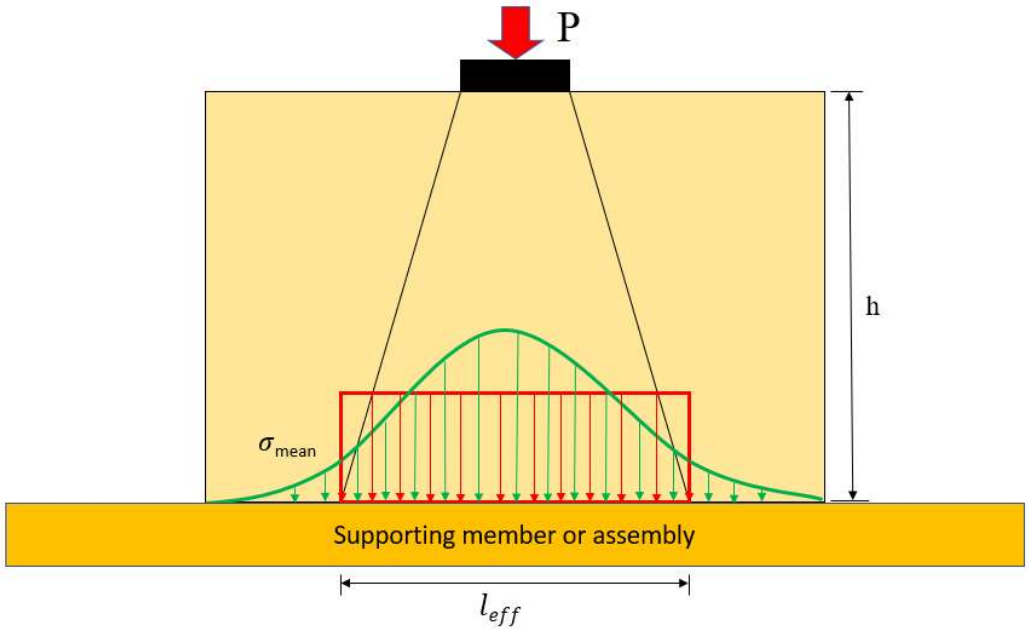

Figure 5.11. Actual compressive stress distribution (green arrows) and gross compressive mean stress (red arrows)

The supporting member or assembly beneath the CLT wall panel experiences a distributed load over an effective length (l_{eff}), as depicted in Figure 5.11. Thus, the design of the supporting member or assembly should consider the effective load area ($b \times l_{eff}$), applied load (P), and a compression stress modification factor (K). The application of the K is to convert the mean applied stress to the peak stress.

Based on the three parameters examined in this research, two compression stress modification factors, K_1 and K_2, were developed for the above loading situations involving compressive load applied at the middle and edge of the CLT respectively. After obtaining the maximum compressive stress results from the FE models, a multiple linear regression analysis was conducted to create an empirical model with the best fit, using Stata (2015).

According to the 72 models presented in Category 1, the ratio of peak stress to mean stress, K_1, can be obtained from the following equation:

$$K_1 = 1.34\left(\frac{h}{w}\right)^{0.11}\left(\frac{a}{w}\right)^{-0.16} p^{0.03} \qquad (5\text{-}6)$$

K_2 represents the ratio of peak stress over mean stress for Category 2, which can be determined as below:

$$K_2 = 0.582\left(\frac{h}{w}\right)^{0.23}\left(\frac{a}{w}\right)^{-0.61} p^{0.06} \quad (5\text{-}7)$$

Where:

K_1 and K_2 = the ratios of the maximum to the mean compression stress

h/w = Height to width of CLT panel ratio

a/w = Width of loading area to width of CLT panel ratio

p = Percentage of transverse layers (%)

The adjusted R-squared were 0.61 and 0.8 for equations (5-6) and (5-7), respectively. Figures 5.12 and 5.13 illustrate the scatter plots of the predicted and actual values of K in Categories 1 and 2. The predicted values are determined by a multiple regression model created with the values derived from the FE model, while the actual values refer to the values obtained from the FE model. It is noted that the K range for Category 1 lies between 1.3 to 1.73, while for Category 2, it is 1.2 to 2.15. Moreover, this highlights that the worst discrepancy between predicted and actual values was about 0.1 for Category 1 and 0.2 for Category 2.

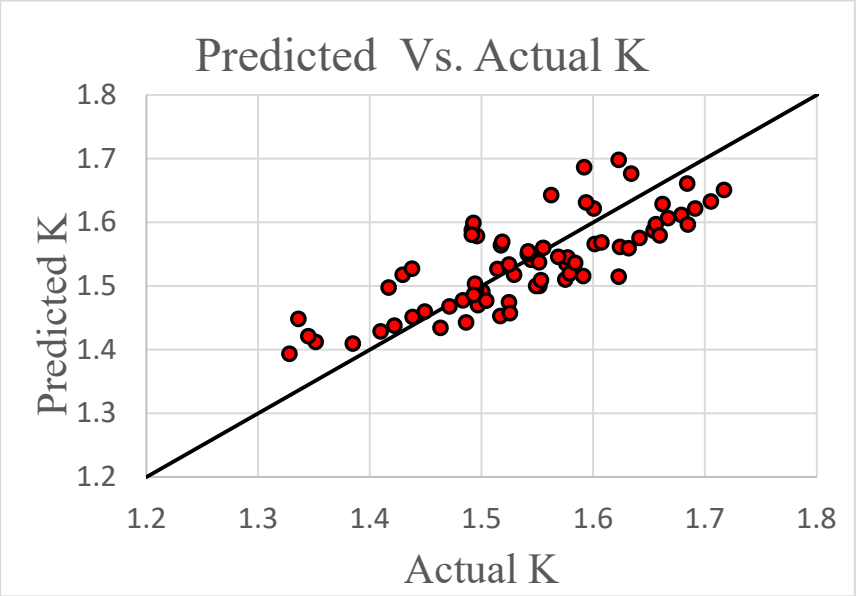

Figure 5.12. Predicted vs. actual K for Category 1

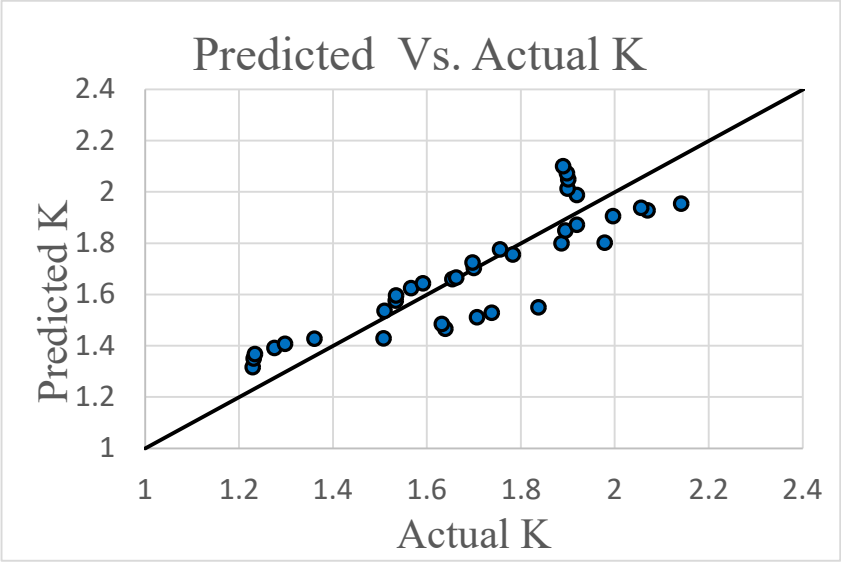

Figure 5.13. Predicted vs. actual K for Category 2

Chapter 6: Conclusion and Recommendations

6.1 Summary

This research was carried out to bridge the knowledge gap in the behavior of cross-laminated timber (CLT) under in-plane concentrated compression loading. Several laboratory tests were conducted to better understand this behavior for various thicknesses and layups. These experiments were designed to investigate how load transmission is likely to occur in reality when a CLT panel is subjected to a concentrated compression load on the narrow face. ABAQUS software was used to create 3D finite element models to predict this behavior. After confirming the validity of the FE models, they were used to generate additional data to allow for the development of empirical equations to predict the load spread angle based on three input parameters: the aspect ratio of CLT (h/w), the ratio of loading area width to panel width (a/w), and the ratio of total transverse layer thickness to total CLT thickness. The conclusions of this study are discussed in this chapter, along with recommendations for further research.

6.2 Conclusions

The conclusions from this study are summarized below:

- Under an in-plane local compression load, CLT panel exhibits a nonlinear, bell-shaped load distribution, with high load under the loading area and rapidly decreasing load moving away from the loading zone.
- The gaps between laminations significantly affect the load distribution, reducing load spreading along the sides of the CLT panel. A more even load spread is obtained when the loading area intercepts a smaller number of gaps.

- The load spread angle initially increases with aspect ratio (h/w) until it reaches a peak at h/w equal to 0.74, after which it decreases up to h/w of 1.25. However, in general, within the range of aspect ratios (h/w) studied (0.37 to 1.25), aspect ratio has a minor influence on load-spread angle, with the values staying within 3° of each other.
- By increasing the number of layers from 3 to 7 of CLT panels, the load distribution angle goes up between 1° and 2 °.
- Reducing the width of the loading area to the CLT panel width (a/w) from 0.24 to 0.38 causes the load-spread angle to increase by approximately 2°.
- The most influential parameter on load spread angle is transverse layer percent. It is noted that an increase in the transverse layer percent in CLT panel from 13% to 50% results in a significant increase in the load spread angle, raising it from 10° to 18° for an aspect ratio of 0.59, 12° to 17° for an aspect ratio of 0.88, and 12° to 14° for an aspect ratio of 1.25.

6.3 Recommendations for future works

The following areas are recommended for future investigations on CLT panel behavior under concentrated in-plane compression loading:

- Because this study was based on small-scale specimens and numerical modelling, full-scale panels should be tested under various loading configurations and positions to confirm the validity of the findings from this study.
- The CLT used in this study had no edge gluing. The influence of narrow-face bonding is expected to have a significant influence on the load distribution. Its effect should be investigated in a future study.
- In this study, the bottom supports were assumed to be rigid. This assumption is not representative of support conditions in real structures, however. For a better understanding

of CLT panel behavior under concentrated edge compression loads, further research should be undertaken considering deformable support.

6.4 Highlights for the original contribution of this project

The present research contributes to cross-laminated timber (CLT) design by presenting a novel approach and set of equations for estimating the load spread angle of CLT panels under in-plane concentrated compressive loading. 18 compression tests on CLT panels with varying geometries and composition were conducted in order to validate a finite element model, which was then used to investigate load spreading from the loading area to the support area. In order to achieve this angle with reasonable accuracy, three influential parameters were taken into account, including aspect ratio (h/w), loading area width to CLT panel width (a/w), and transverse layer percentage. These results have significant implications for designers, providing new insights and understanding in determining the load spread angle of CLT panels for structural applications. Furthermore, the empirical equations developed in this study have the potential to be further developed to consider additional parameters or to be used in conjunction with other design approaches. Overall, this research serves as an important contribution to the existing body of knowledge on estimating load spread angles of CLT panels under in-plane concentrated compression loading and has the potential to inspire future research in this area.

Bibliography

Alinoori, F., Moshiri, F., Sharafi, P., and Samali, B. 2020. Reinforcement methods for compression perpendicular to grain in top/bottom plates of light timber frames. Construction and Building Materials, **231**: 116377. Elsevier Ltd. doi:10.1016/j.conbuildmat.2019.07.103.

Brandner, R. 2018. Cross laminated timber (CLT) in compression perpendicular to plane: Testing, properties, design and recommendations for harmonizing design provisions for structural timber products. Engineering Structures, **171**(November 2017): 944–960. Elsevier. doi:10.1016/j.engstruct.2018.02.076.

Buck, D., Wang, X., Hagman, O., and Gustafsson, A. 2016. Further development of cross-laminated timber (CLT) - Mechanical tests on 45° alternating layers. WCTE 2016 - World Conference on Timber Engineering, (August).

Ceccotti, A., Sandhaas, C., Okabe, M., Yasumura, M., Minowa, C., and Kawai, N. 2013. SOFIE project – 3D shaking table test on a seven-storey full-scale cross-laminated timber building. Earthquake Engineering & Structural Dynamics, **42**(13): 2003–2021. John Wiley & Sons, Ltd. doi:10.1002/EQE.2309.

CSA. 2019. CAN/CSA-086-01. A National Standard of Canada. Engineering Design in Wood. *In* Standard.

Dietsch, P., and Brandner, R. 2015. Self-tapping screws and threaded rods as reinforcement for structural timber elements-A state-of-the-art report. Construction and Building Materials, **97**: 78–89. Elsevier Ltd. doi:10.1016/j.conbuildmat.2015.04.028.

Eurocode. 2005. EN 1995-1-1:2004 - Eurocode: Design of Timber Structures - General.

FPL, U. 2021. Wood Handbook 2021.

Gräfe, M., Dietsch, P., Hipper, A., and Wild, M. 2018. Vorspannung von Brettsperrholzkonstruktionen.

Jeleč, M., Varevac, D., and Rajčić, V. 2018. Cross-laminated timber (CLT) – a state of the art report. Journal of the Croatian Association of Civil Engineers, **70**(02): 75–95. doi:10.14256/jce.2071.2017.

Karacabeyli, E., and Gagnon, S. 2019. Canadian Cross Laminated Timber Handbook: 2019 Edition.

Kurzinski, S., Crovella, P., and Kremer, P. 2022. Overview of Cross-Laminated Timber (CLT) and Timber Structure Standards Across the World. Mass Timber Construction Journal | www.masstimberconstructionjournal.com Mass Timber Construction Journal, **5**. doi:10.55191/MTCJ.2022.1.

Lantsoght, E.O.L., Van Der Veen, C., De Boer, A., and Walraven, J.C. 2015. Transverse load redistribution and effective shear width in reinforced concrete slabs. Heron, **60**(3): 145–179.

Leijten, A.J.M. 2016. The bearing strength capacity perpendicular to grain of Norway spruce - Evaluation of three structural timber design models. Construction and Building Materials, **105**(2016): 528–535. Elsevier Ltd. doi:10.1016/j.conbuildmat.2015.12.170.

Leijten, A.J.M., Jorissen, A.J.M., and De Leijer, B.J.C. 2012. The local bearing capacity perpendicular to grain of structural timber elements. Construction and Building Materials, **27**(1): 54–59. Elsevier Ltd. doi:10.1016/j.conbuildmat.2011.07.022.

Leijten, A.J.M., Larsen, H.J., and Van der Put, T.A.C.M. 2010. Structural design for compression

strength perpendicular to the grain of timber beams. Construction and Building Materials, **24**(3): 252–257. Elsevier Ltd. doi:10.1016/j.conbuildmat.2009.08.042.

Li, H., Wang, B.J., Wei, P., and Wang, L. 2019. Cross-laminated Timber (CLT) in China : A State-of-the-Art. Journal of Bioresources and Bioproducts, **4**(1): 22–31. Elsevier Masson SAS. doi:10.21967/jbb.v4i1.190.

Niederwestberg, J. 2019. Influence of laminate characteristics on properties of single-layer and cross laminated timber (CLT) panels.

Oh, J.K., Lee, J.J., and Hong, J.P. 2015. Prediction of compressive strength of cross-laminated timber panel. Journal of Wood Science, **61**(1): 28–34. doi:10.1007/s10086-014-1435-x.

Pang, and Jeong, Y. 2018. Load sharing and weakest lamina effects on the compressive resistance of cross-laminated timber under in-plane loading. Journal of Wood Science, **64**(5): 538–550. Springer Japan. doi:10.1007/s10086-018-1741-9.

Parajuli, R., Gale, C., Vlosky, R., and Martin, R.O. 2018. An overview of cross-laminated timber in North America. Increasing the Use of Wood in the Global Bio-Economy - Proceedings of Scientific Papers,: 217–225.

Van Der Put, T.A.C.M. 2008. Derivation of the bearing strength perpendicular to the grain of locally loaded timber blocks. Holz als Roh - und Werkstoff, **66**(6): 409–417. doi:10.1007/s00107-008-0258-0.

Serrano, E., and Enquist, B. 2010. Compression strength perpendicular to grain in cross-laminated timber (CLT).

Simulia. 2020. ABAQUS Software (No. 2020). Dassault Systèmes, United State.

StataCorp. 2015. Stata Statistical Software: Release 14. StataCorp LP.

Structurlam. 2020. Mass Timber Technical Guide There ’ s a Revolution And Structurlam Is.

Totsuka, M., Aoki, K., and Inayama, M. 2022. Prediction of strength and stiffness of concentrated compressive load applied to the narrow face of cross-laminated timber. European Journal of Wood and Wood Products, **80**(2): 451–463. Springer Berlin Heidelberg. doi:10.1007/s00107-021-01765-4.

Wang, Y., Wang, T., Persson, P., Hedlund, P., Crocetti, R., and Wålinder, M. 2023. Birch plywood as gusset plates in glulam frame via mechanical connectors: A combined experimental and numerical study. Journal of Building Engineering, **65**(December 2022): 105744. Elsevier Ltd. doi:10.1016/j.jobe.2022.105744.

Wu, G., Huo, L., Shen, Y., and Ren, H. 2022. Partially Loaded CLT Member. : 1–12.

Appendix A

This Appendix contains the contour plots of displacement and normal strain, along with their corresponding graphs, comparing the results from DIC and FE modeling with the compression tests conducted at 80% of failure load. These results were previously discussed in Chapter 4.

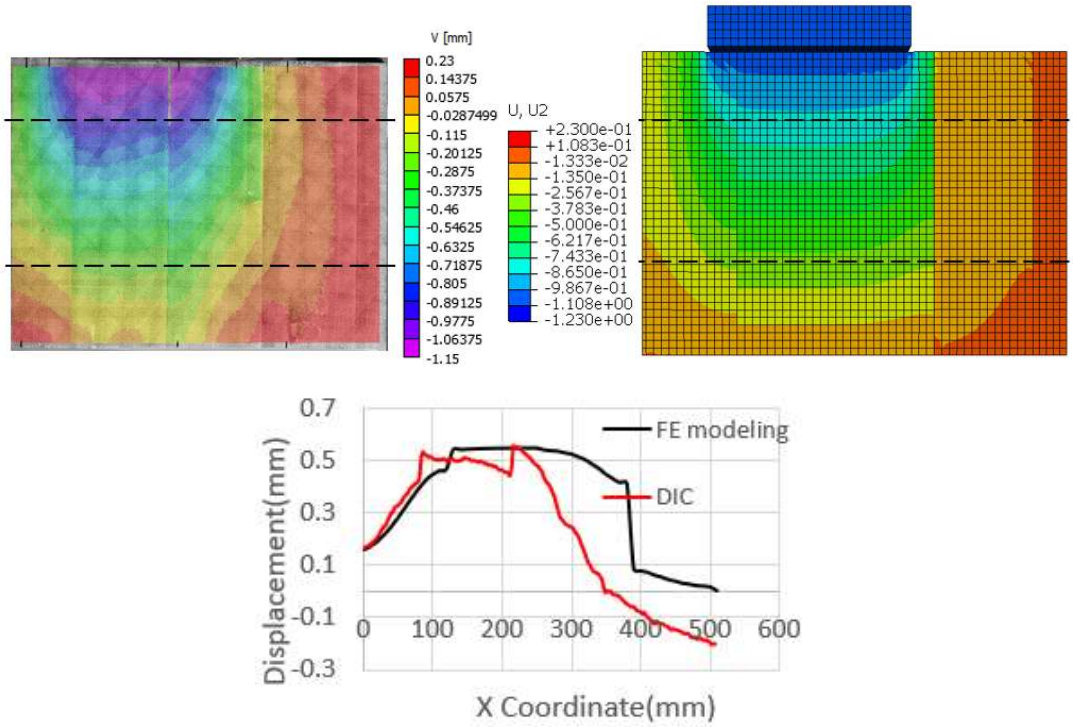

Appendix A.1. Displacement contour plots and displacement graph from compression test at 80% of failure load for specimen A-1- DIC (left), FE modelling (right)

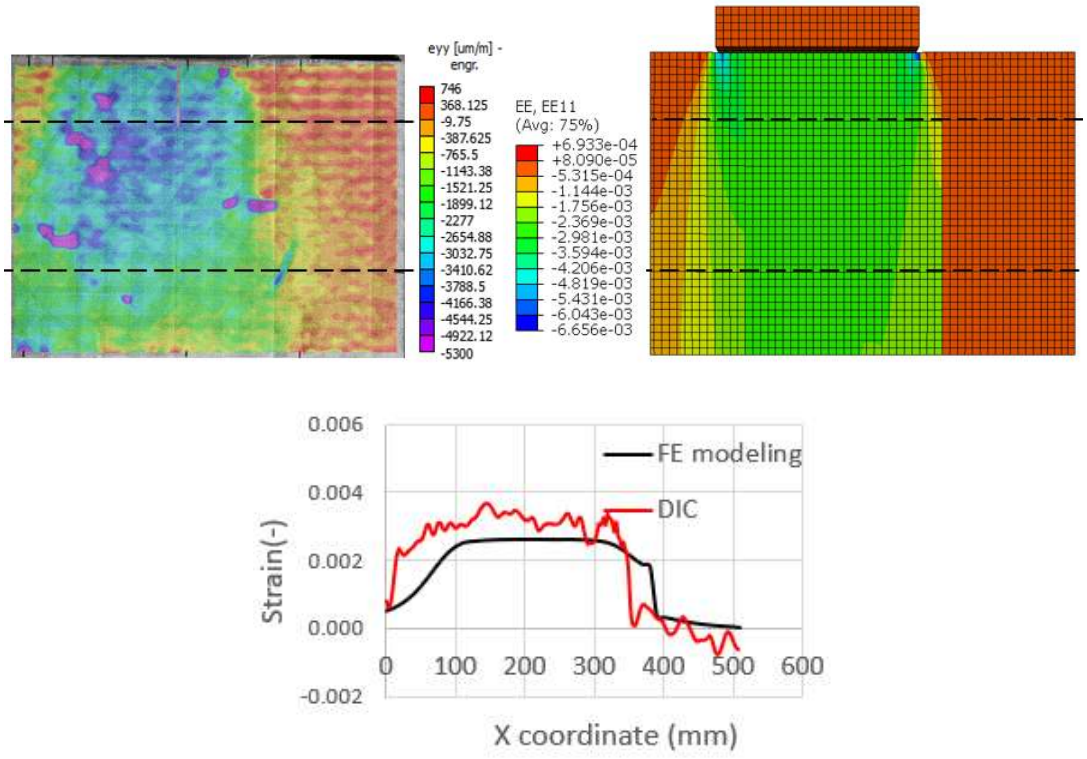

Appendix A.2. Normal strain contour plots and normal strain graph in the y direction from compression test at 80% of failure load for specimen A-1- DIC (left), FE modelling (right)

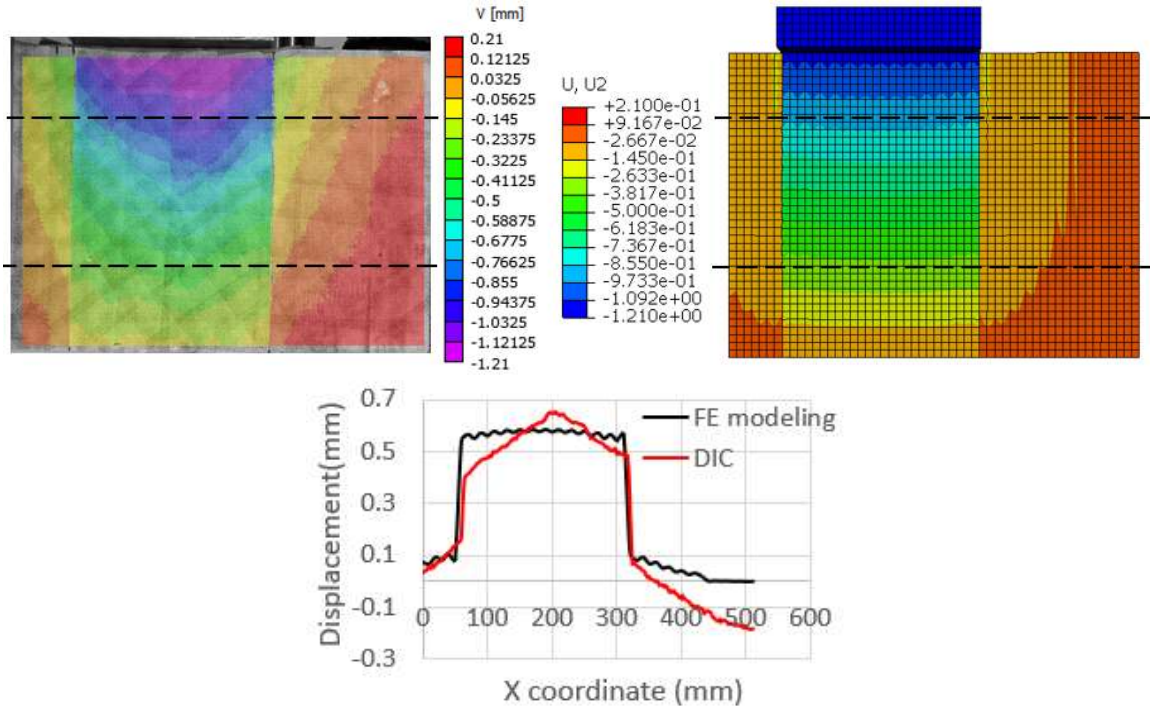

Appendix A.3 Displacement contour plots and displacement graph from compression test at 80% of failure load for specimen A-2- DIC (left), FE modelling (right)

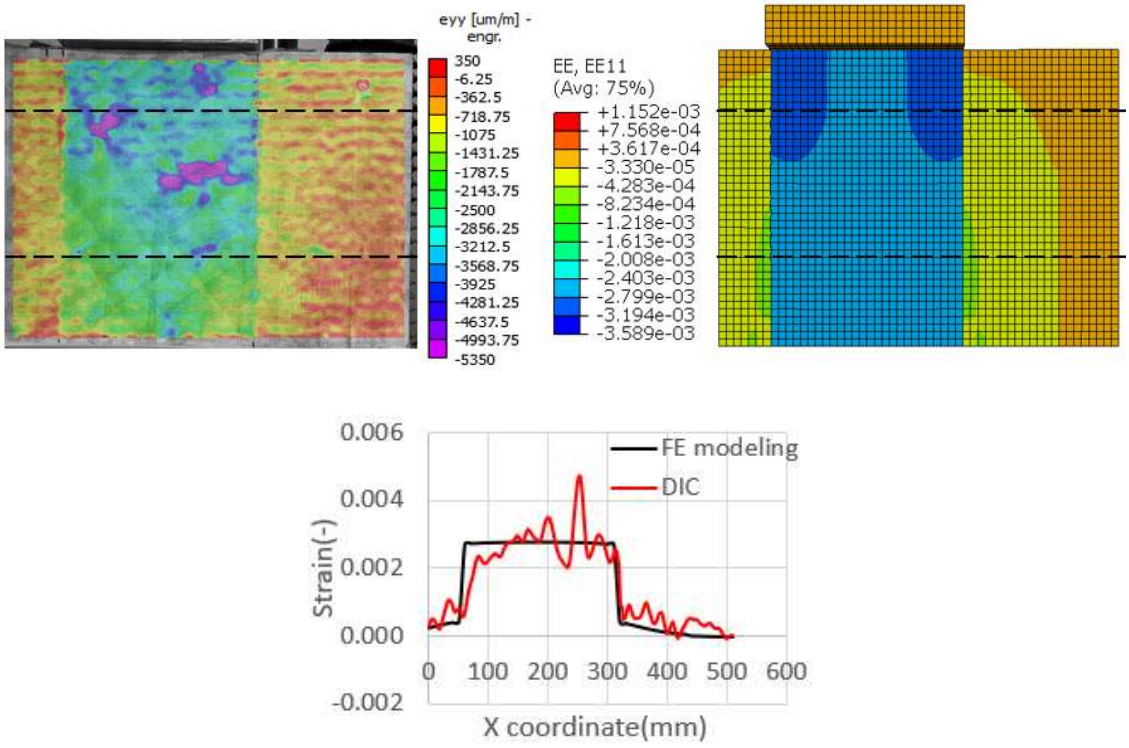

Appendix A.4. Normal strain contour plots and normal strain graph in the y direction from compression test at 80% of failure load for specimen A-2- DIC (left), FE modelling (right)

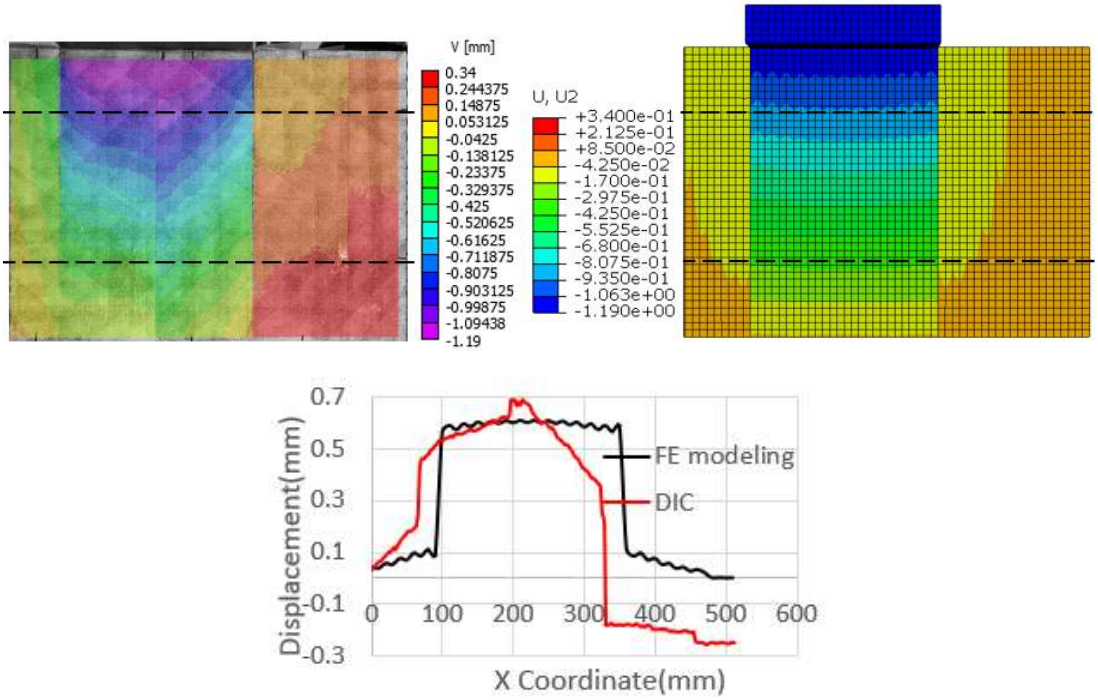

Appendix A.5. Displacement contour plots and displacement graph from compression test at 80% of failure load for specimen A-4- DIC (left), FE modelling (right)

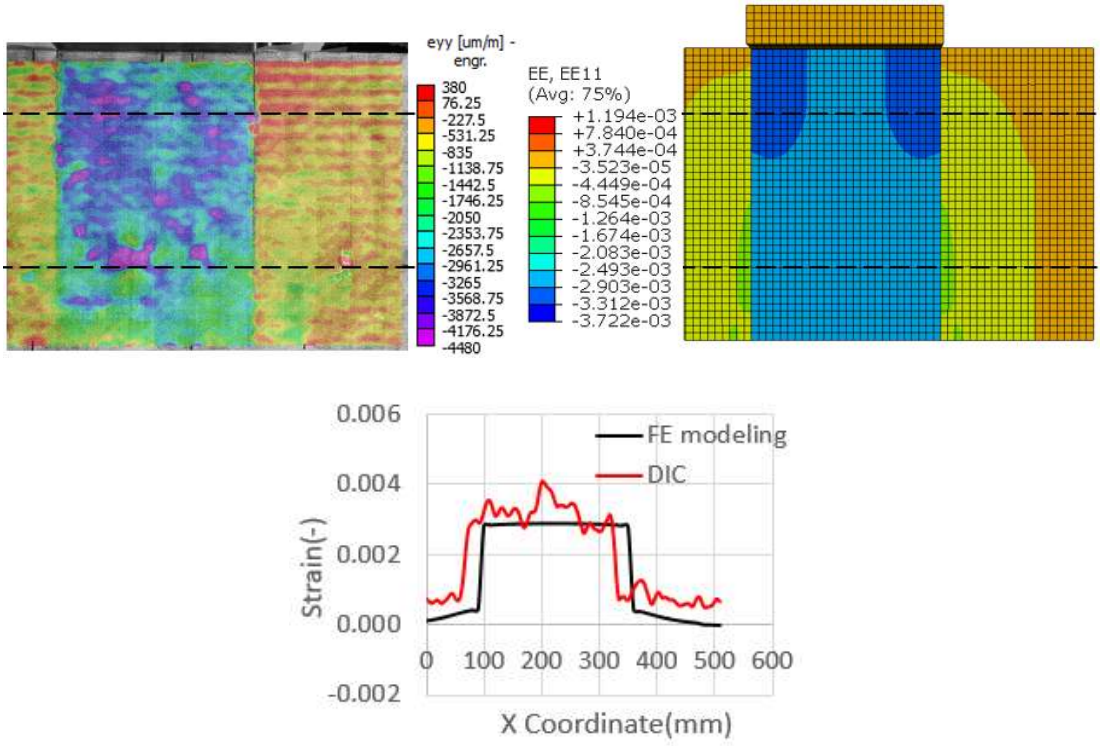

Appendix A.6. Normal strain contour plots and normal strain graph in the y direction from compression test at 80% of failure load for specimen A-4- DIC (left), FE modelling (right)

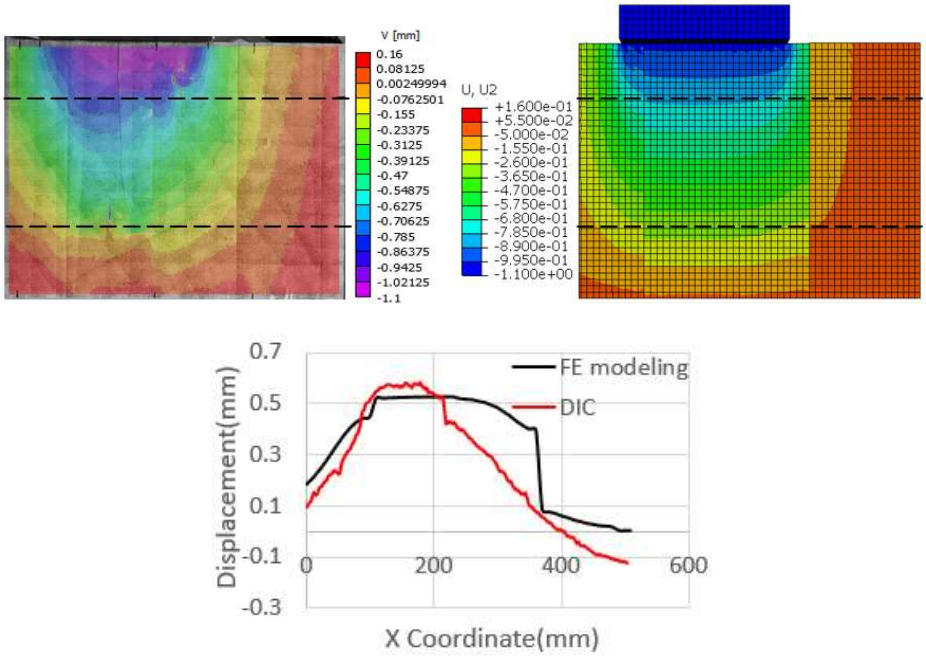

Appendix A.7. Displacement contour plots and displacement graph from compression test at 80% of failure load for specimen A-5- DIC (left), FE modelling (right)

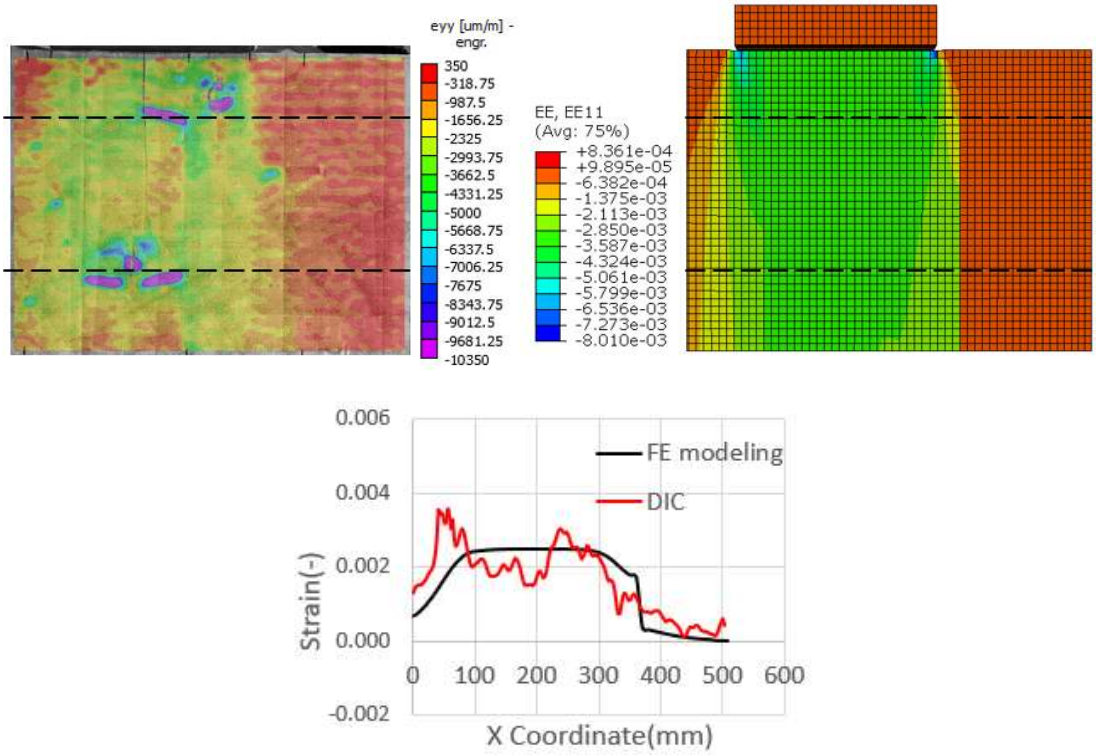

Appendix A.8. Normal strain contour plots and normal strain graph in the y direction from compression test at 80% of failure load for specimen A-5- DIC (left), FE modelling (right)

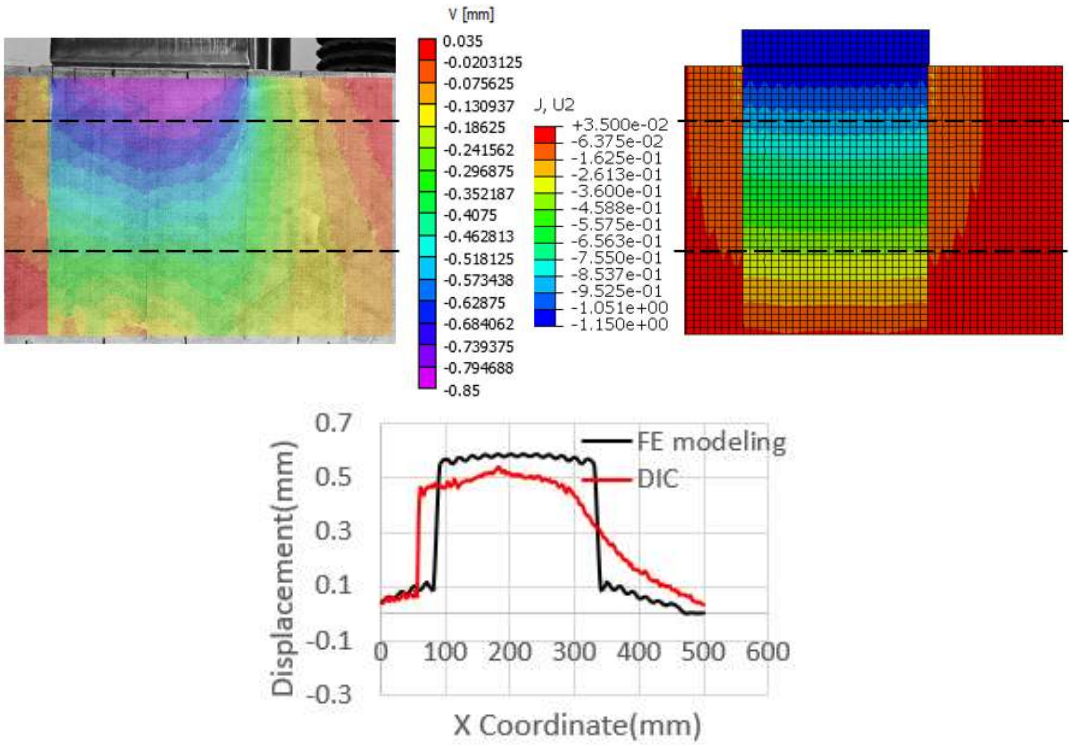

Appendix A.9. Displacement contour plots and displacement graph from compression test at 80% of failure load for specimen B-1- DIC (left), FE modelling (right)

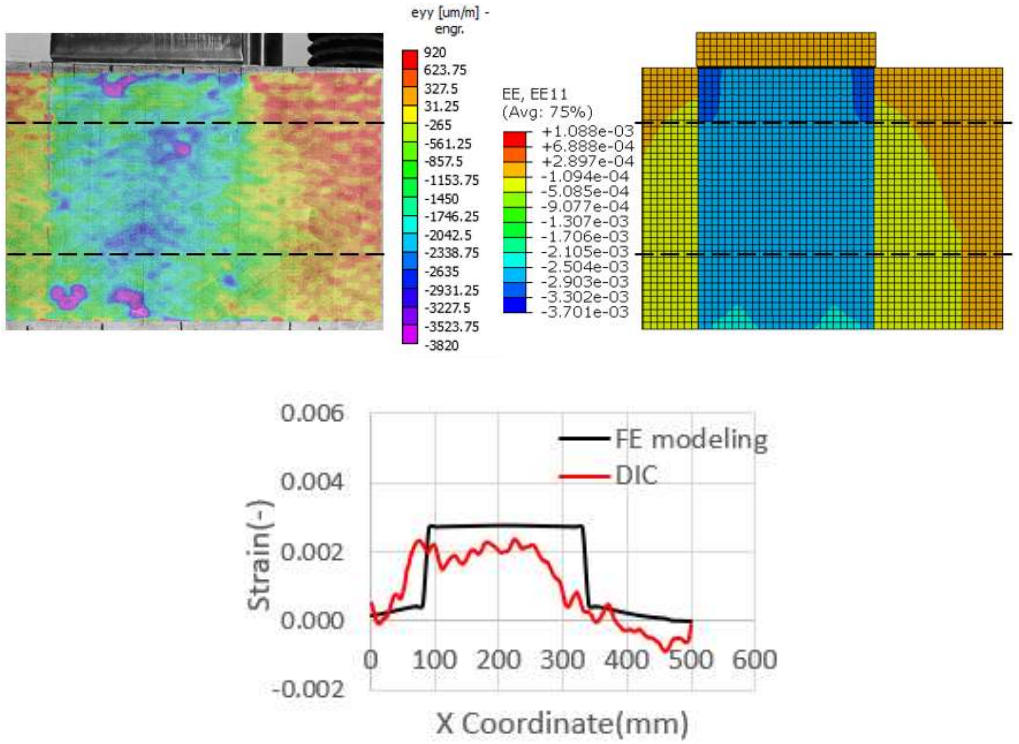

Appendix A.10. Normal strain contour plots and normal strain graph in the y direction from compression test at 80% of failure load for specimen B-1- DIC (left), FE modelling (right)

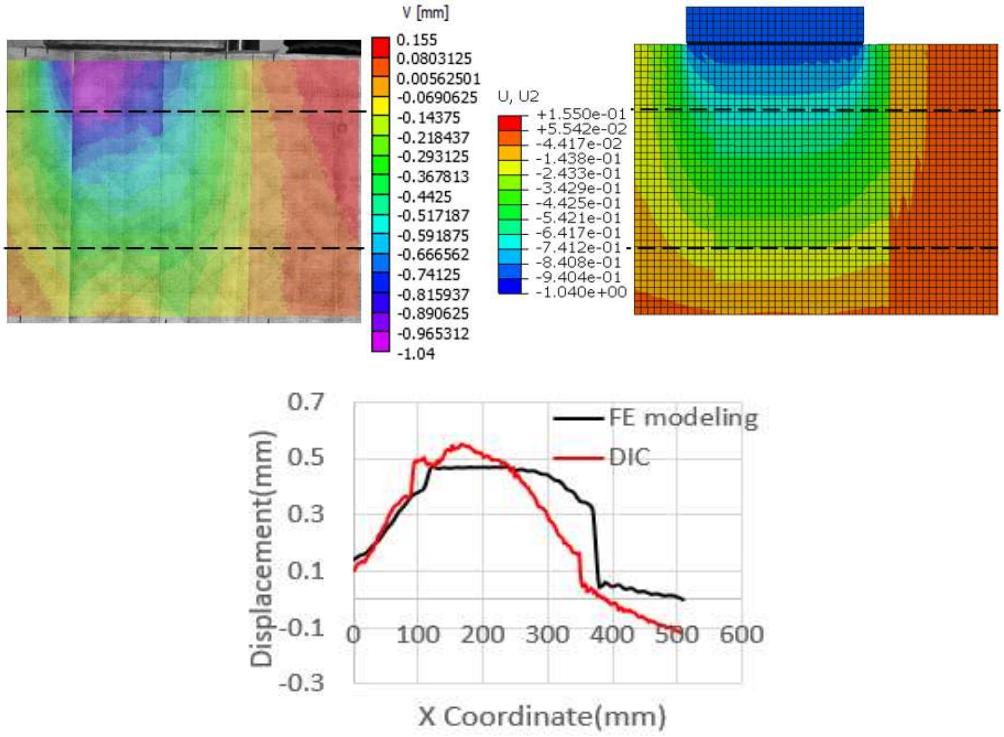

Appendix A.11. Displacement contour plots and displacement graph from compression test at 80% of failure load for specimen B-2- DIC (left), FE modelling (right)

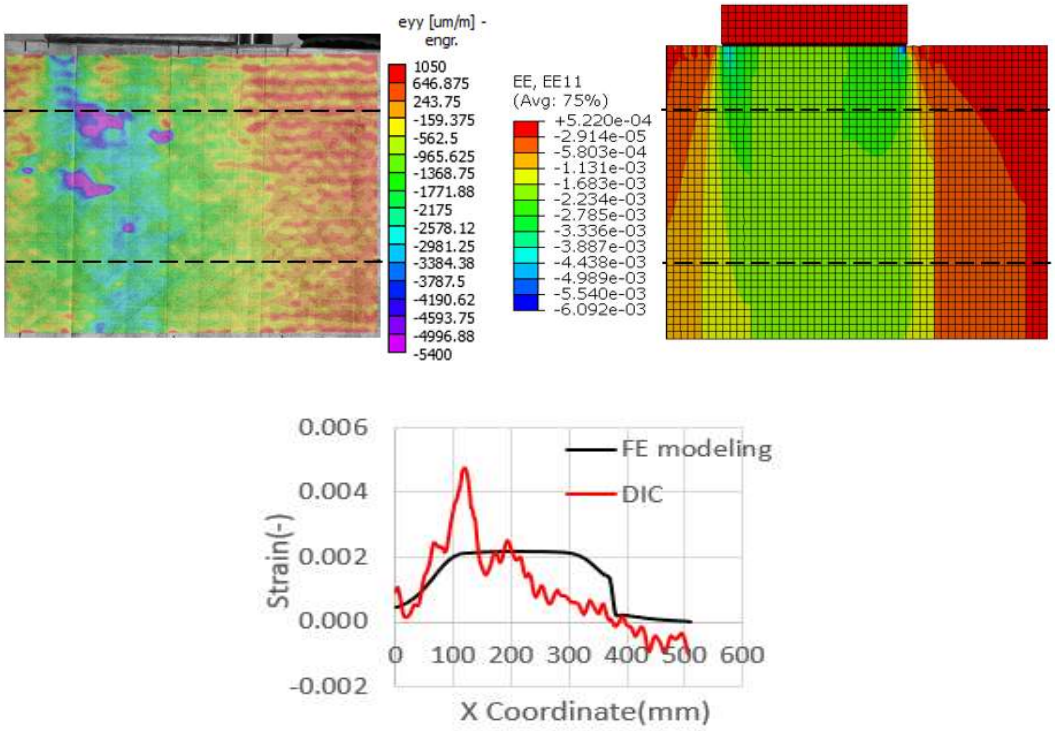

Appendix A.12. Normal strain contour plots and normal strain graph in the y direction from compression test at 80% of failure load for specimen B-2- DIC (left), FE modelling (right)

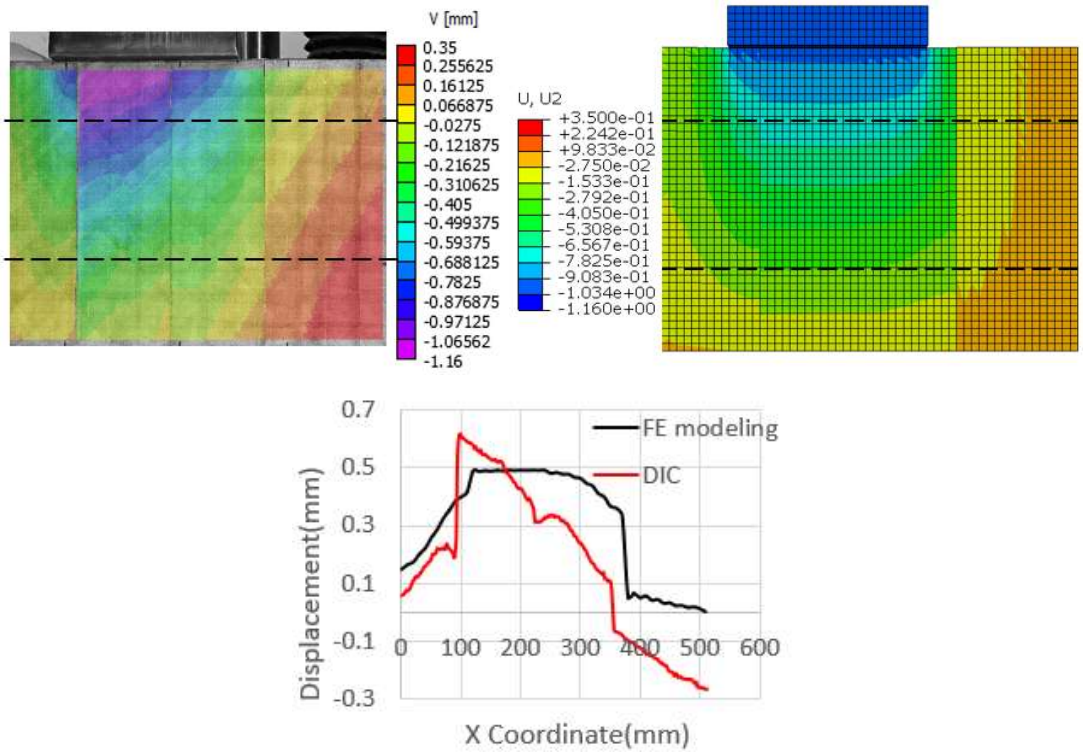

Appendix A.13. Displacement contour plots and displacement graph from compression test at 80% of failure load for specimen B-3- DIC (left), FE modelling (right)

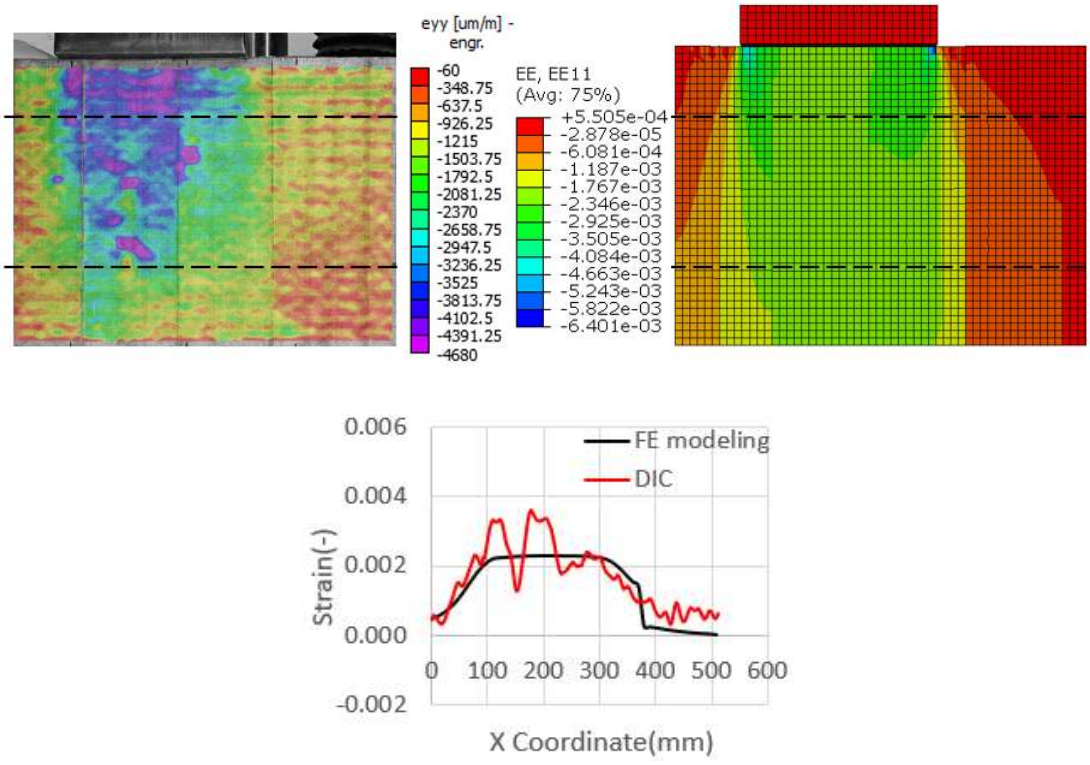

Appendix A.14. Normal strain contour plots and normal strain graph in the y direction from compression test at 80% of failure load for specimen B-3- DIC (left), FE modelling (right)

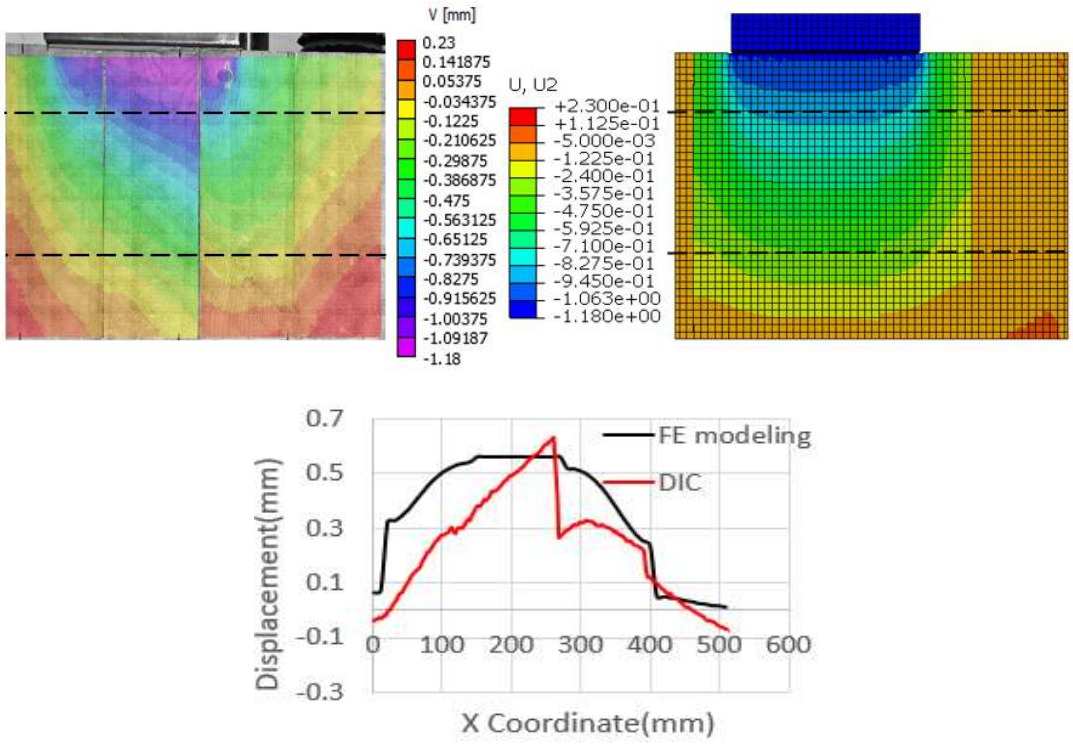

Appendix A.15. Displacement contour plots and displacement graph from compression test at 80% of failure load for specimen B-4- DIC (left), FE modelling (right)

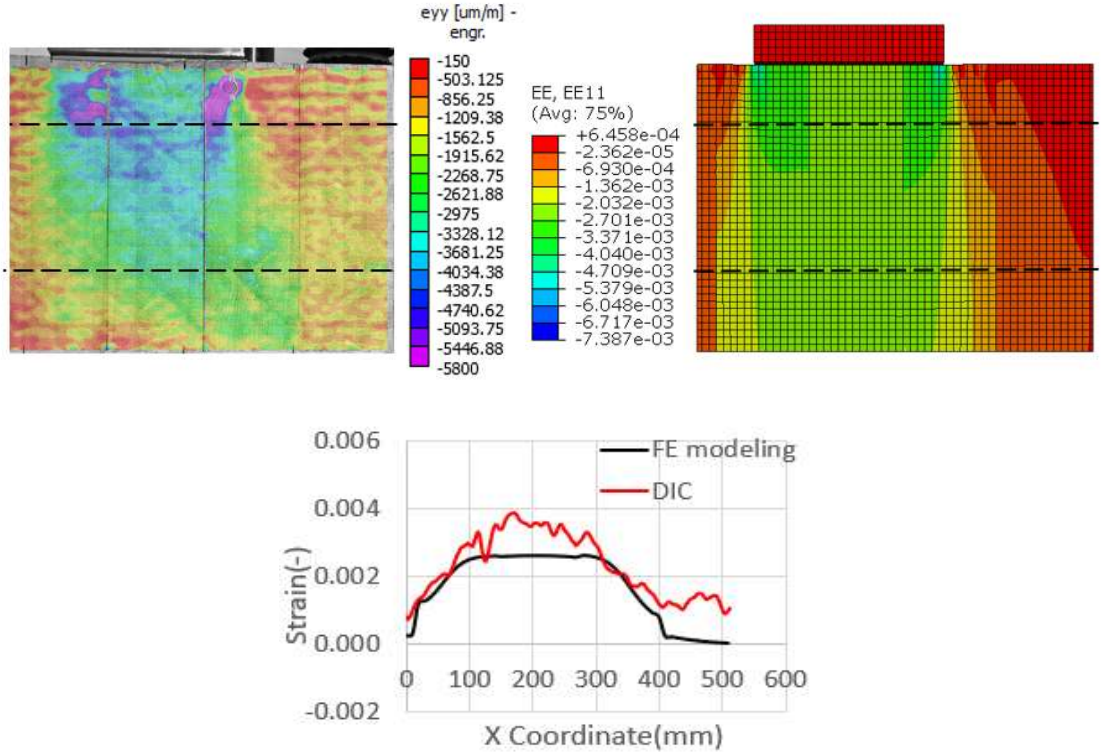

Appendix A.16. Normal strain contour plots and normal strain graph in the y direction from compression test at 80% of failure load for specimen B-4- DIC (left), FE modelling (right)

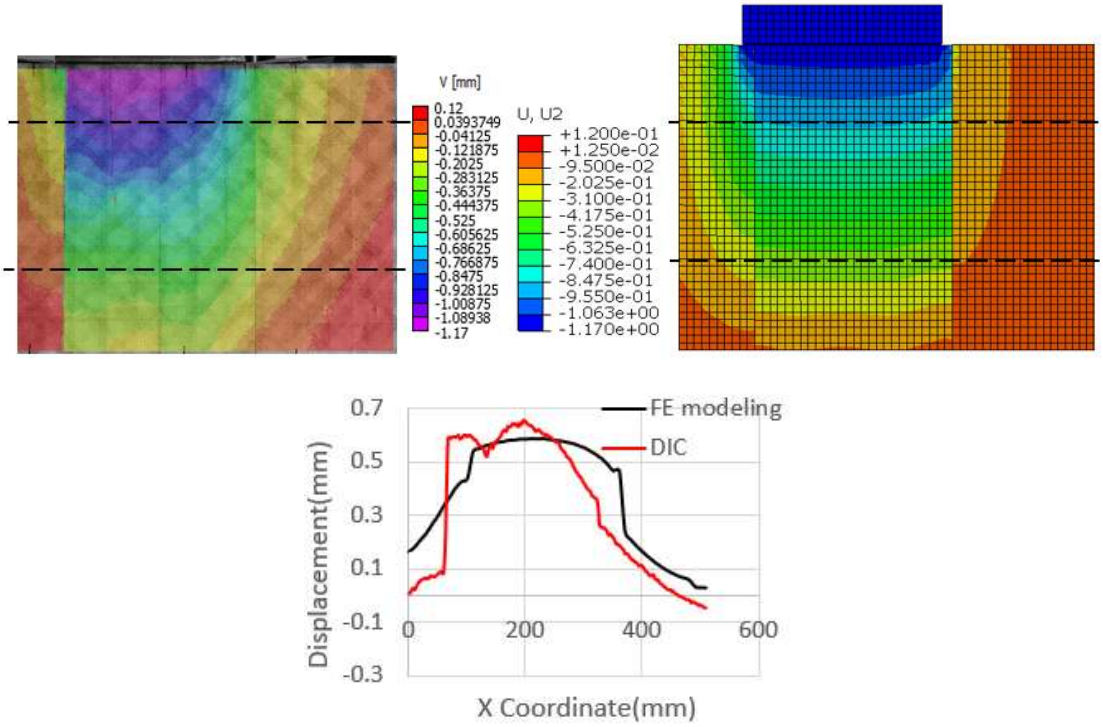

Appendix A.17. Displacement contour plots and displacement graph from compression test at 80% of failure load for specimen C-1- DIC (left), FE modelling (right)

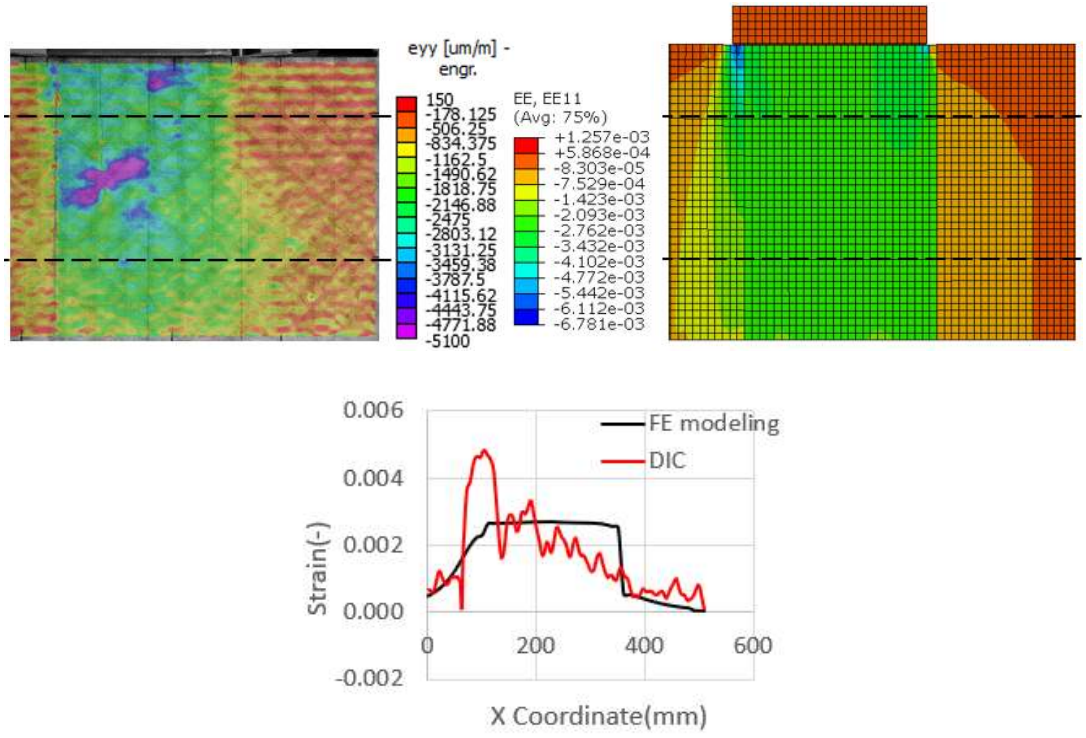

Appendix A.18. Normal strain contour plots and normal strain graph in the y direction from compression test at 80% of failure load for specimen C-1- DIC (left), FE modelling (right)

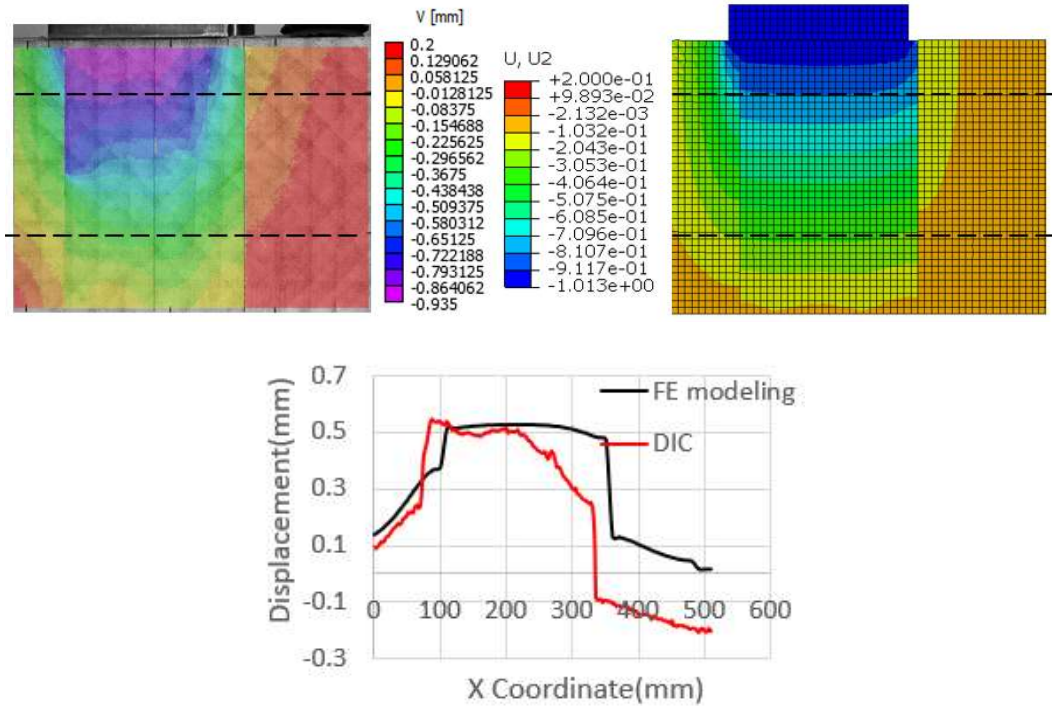

Appendix A.19. Displacement contour plots and displacement graph from compression test at 80% of failure load for specimen C-2- DIC (left), FE modelling (right)

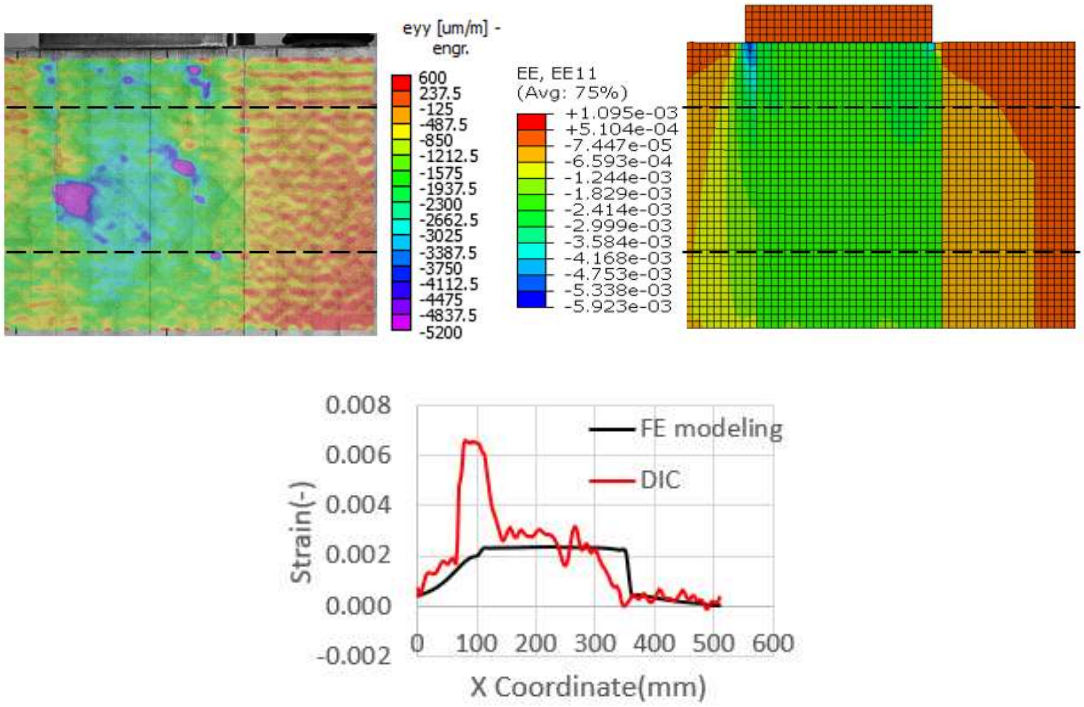

Appendix A.20. Normal strain contour plots and normal strain graph in the y direction from compression test at 80% of failure load for specimen C-2- DIC (left), FE modelling (right)

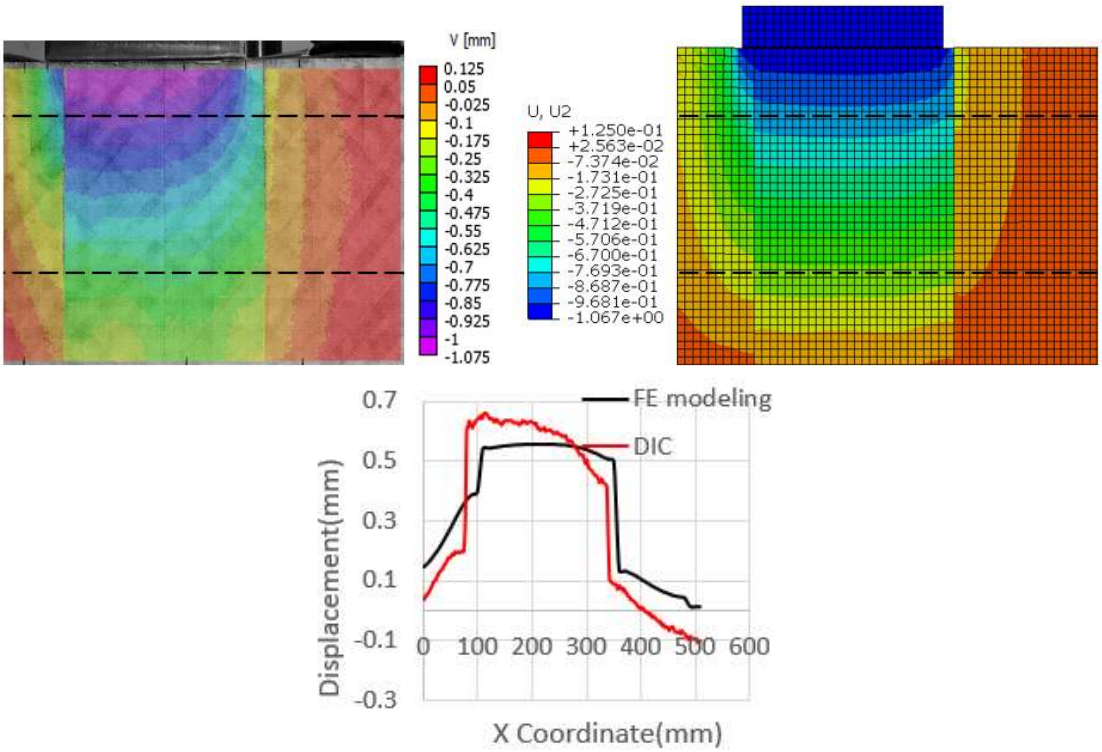

Appendix A.21. Displacement contour plots and displacement graph from compression test at 80% of failure load for specimen C-3- DIC (left), FE modelling (right)

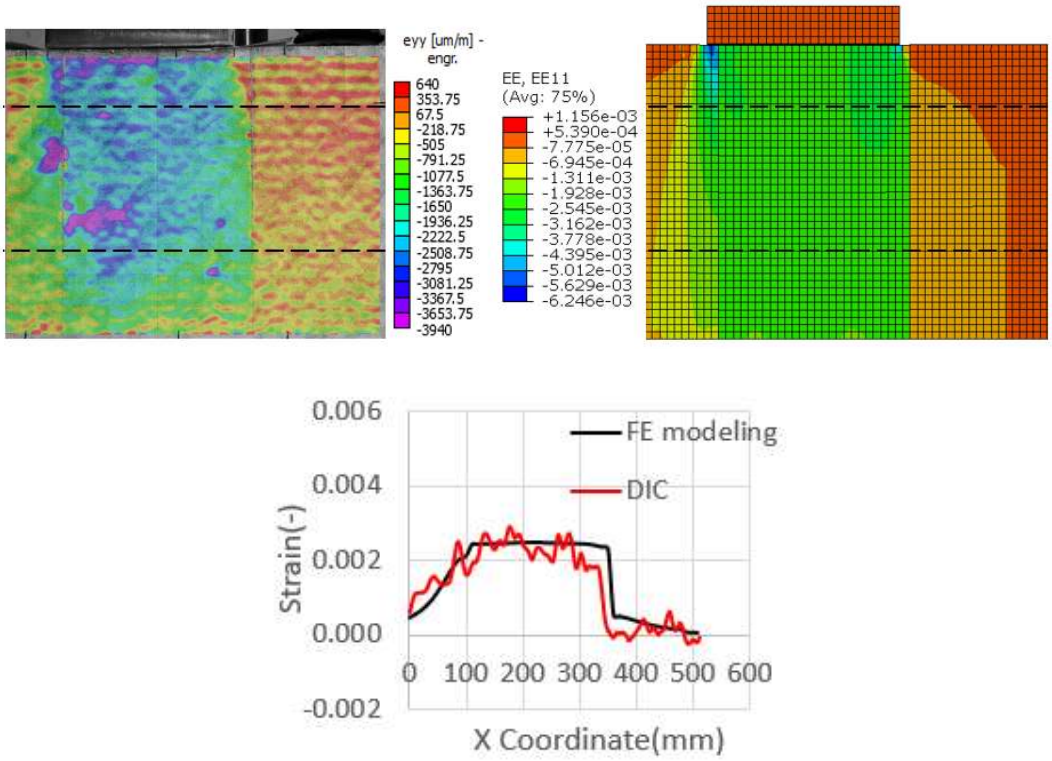

Appendix A.22. Normal strain contour plots and normal strain graph in the y direction from compression test at 80% of failure load for specimen C-3- DIC (left), FE modelling (right)

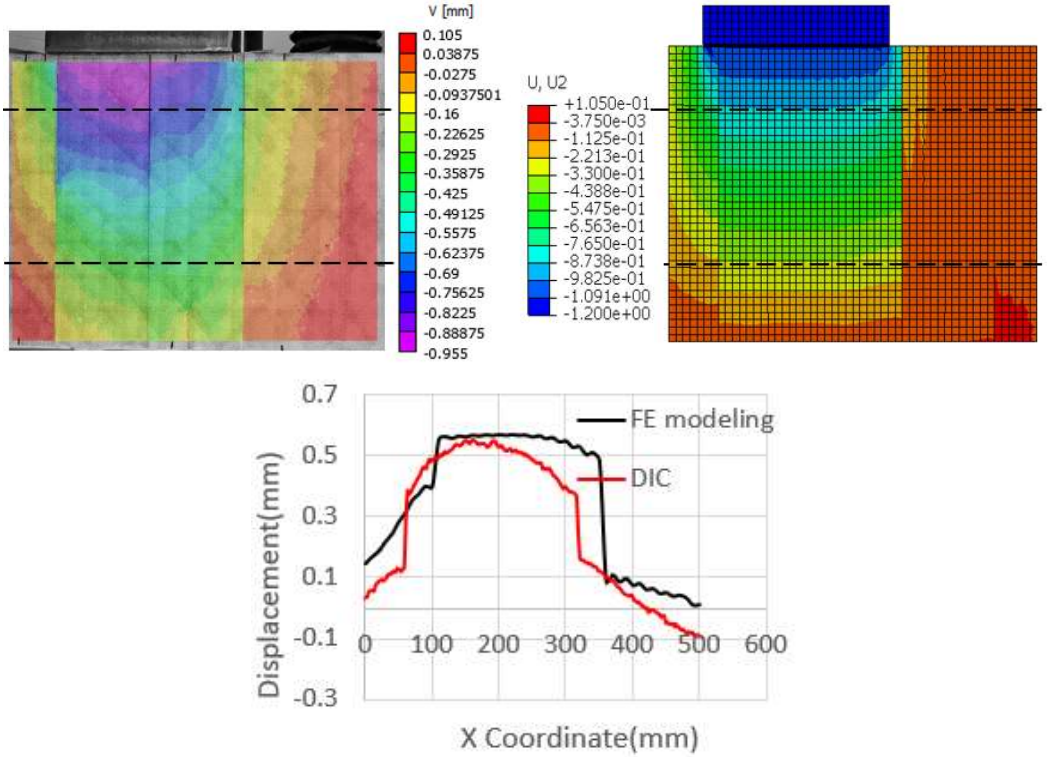

Appendix A.23. Displacement contour plots and displacement graph from compression test at 80% of failure load for specimen C-4- DIC (left), FE modelling (right)

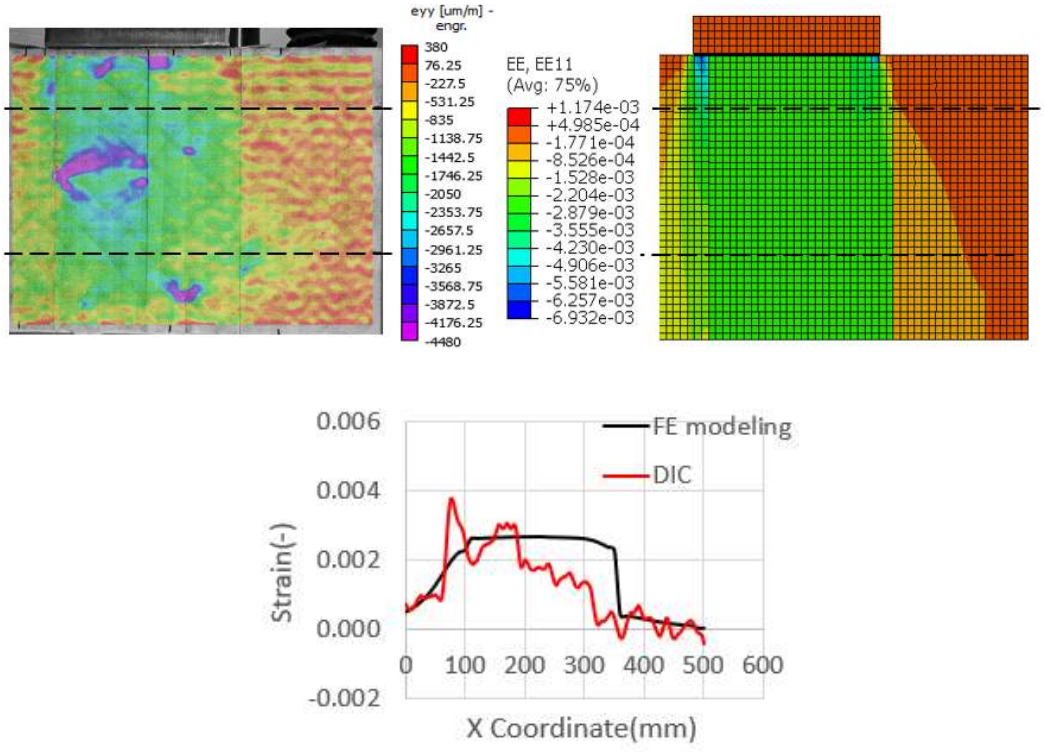

Appendix A.24. Normal strain contour plots and normal strain graph in the y direction from compression test at 80% of failure load for specimen C-4- DIC (left), FE modelling (right)

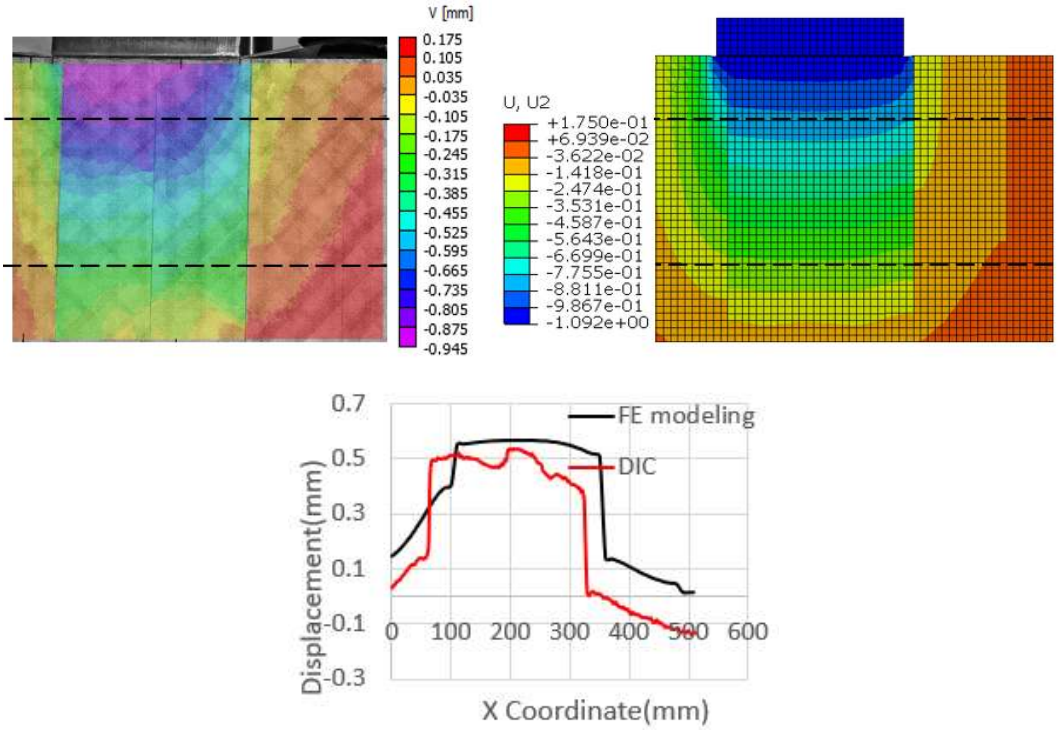

Appendix A.25. Displacement contour plots and displacement graph from compression test at 80% of failure load for specimen C-5- DIC (left), FE modelling (right)

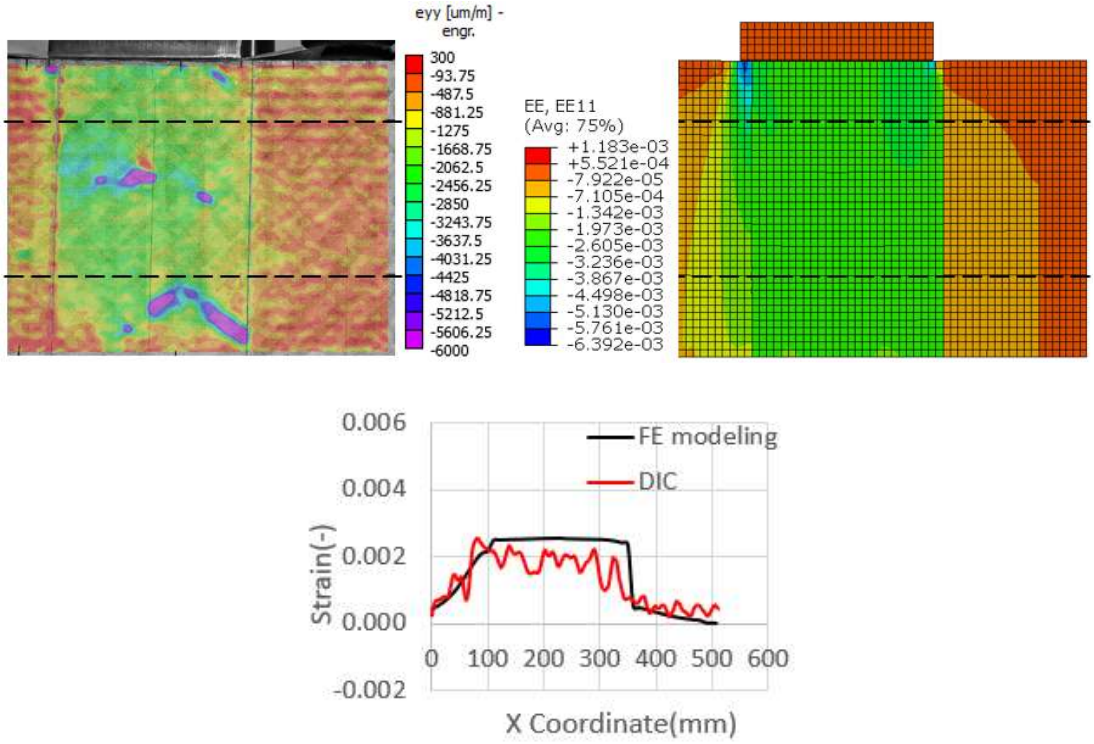

Appendix A.26. Normal strain contour plots and normal strain graph in the y direction from compression test at 80% of failure load for specimen C-5- DIC (left), FE modelling (right)

Appendix B

This Appendix presents the results of the laboratory tests, simulation modeling, and DIC analysis discussed in Chapter 4.

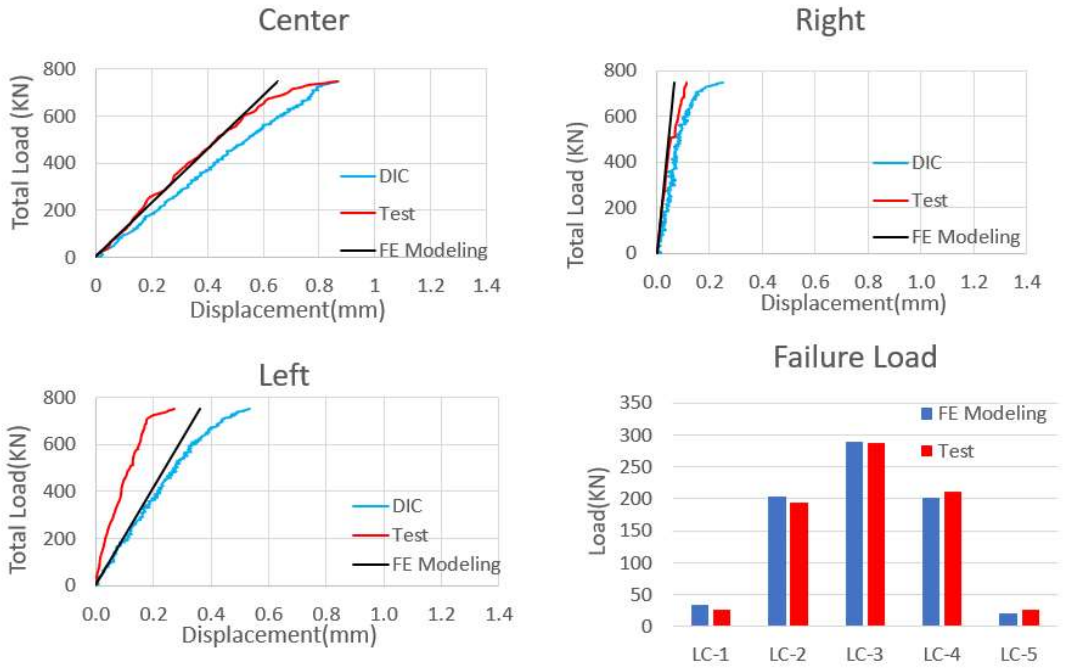

Appendix B.1. DIC, Test and FE modelling results and load distribution results for specimen A-1 until failure

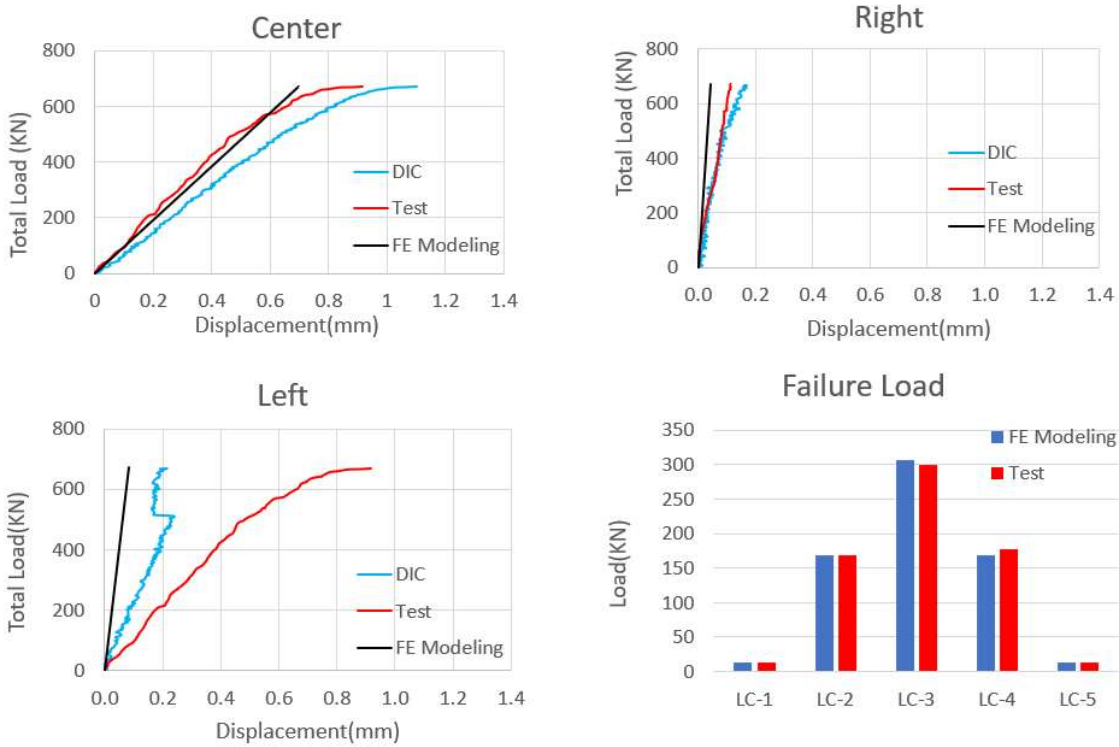

Appendix B.2. DIC, Test and FE modelling results and load distribution results for specimen A-2 until failure

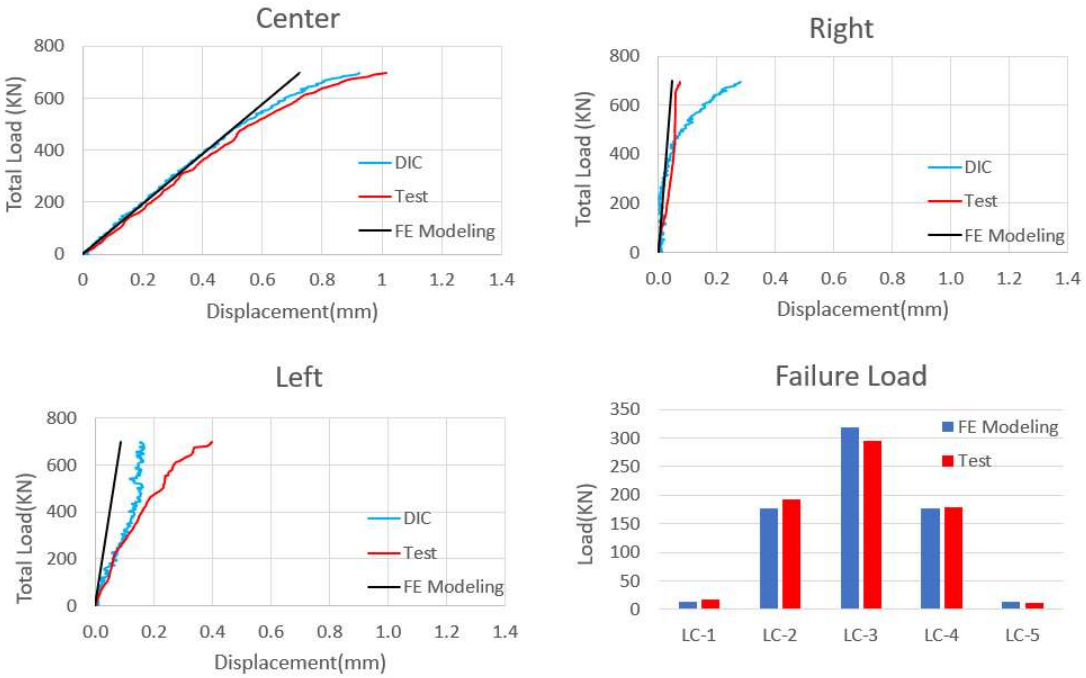

Appendix B.3. DIC, Test and FE modelling results and load distribution results for specimen A-4 until failure

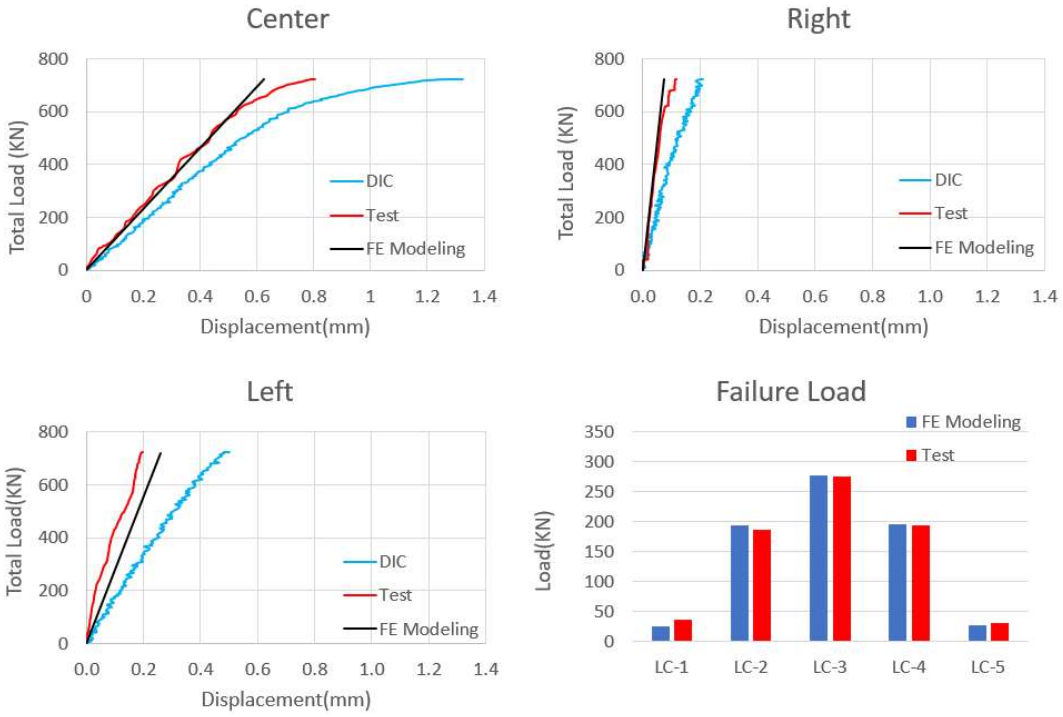

Appendix B.4. DIC, Test and FE modelling results and load distribution results for specimen A-5 until failure

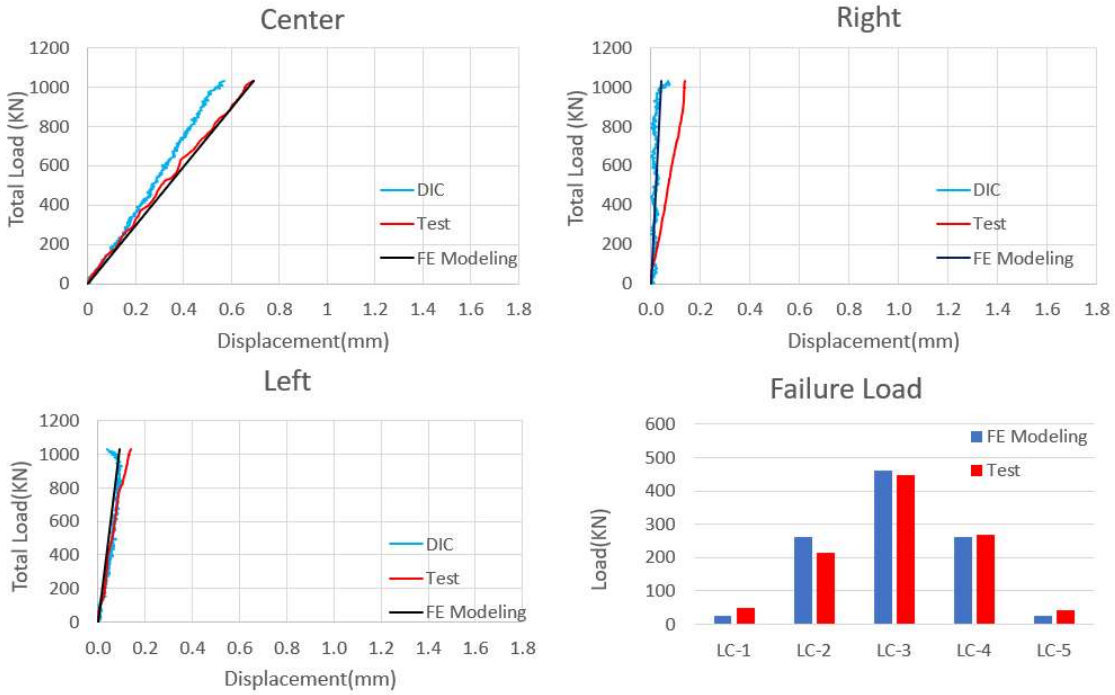

Appendix B.5. DIC, Test and FE modelling results and load distribution results for specimen B-1 until failure

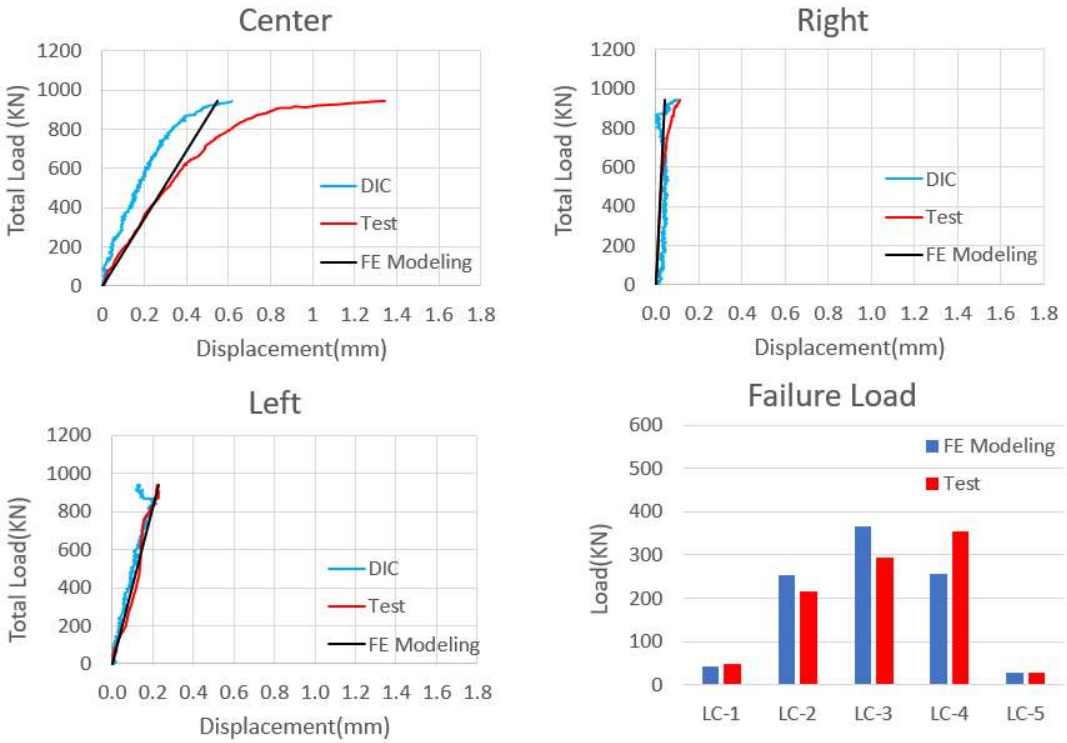

Appendix B.6. DIC, Test and FE modelling results and load distribution results for specimen B-2 until failure

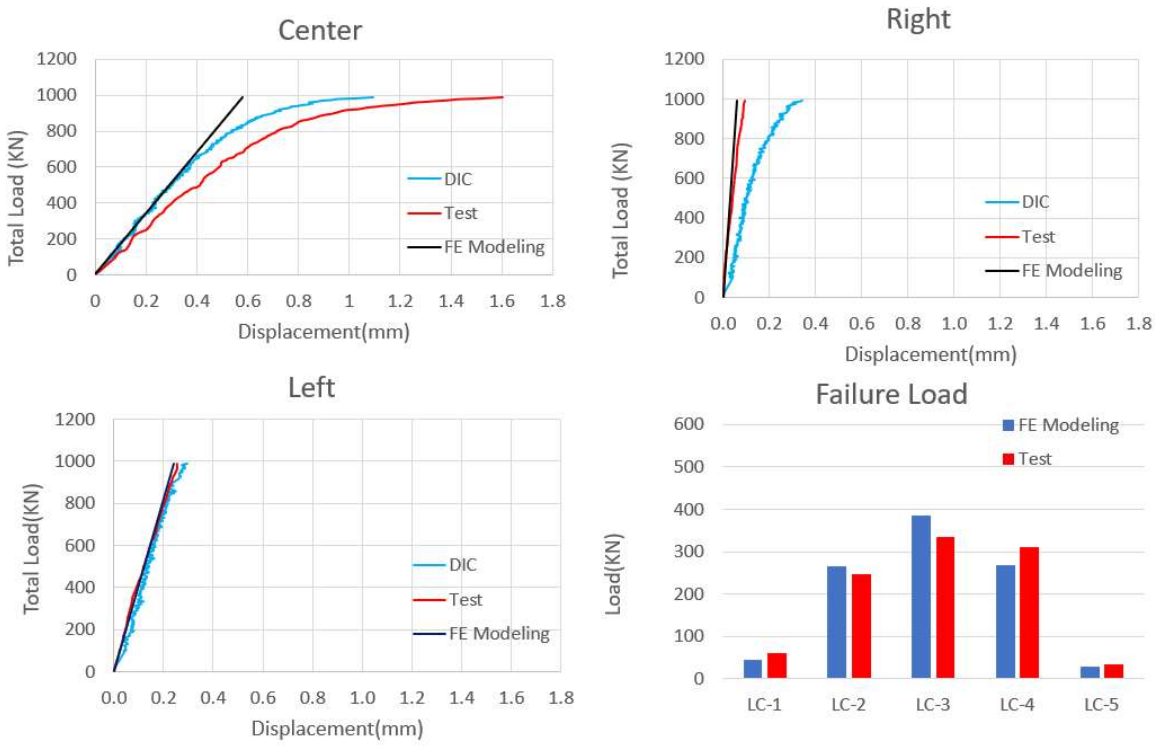

Appendix B.7. DIC, Test and FE modelling results and load distribution results for specimen B-3 until failure

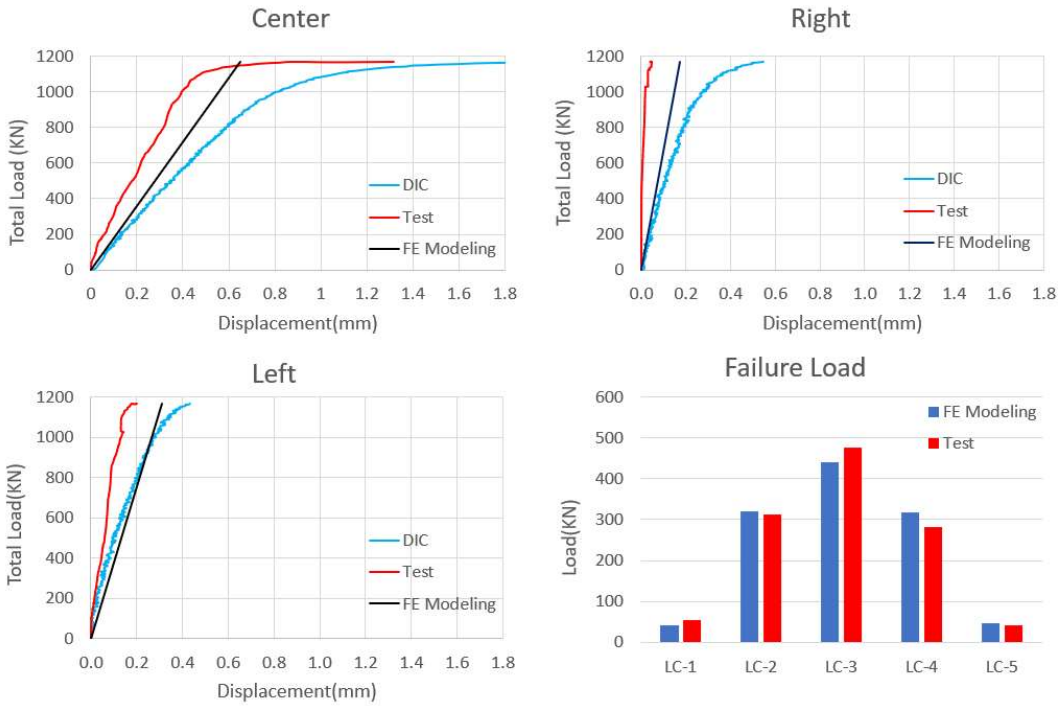

Appendix B.8. DIC, Test and FE modelling results and load distribution results for specimen B-4 until failure

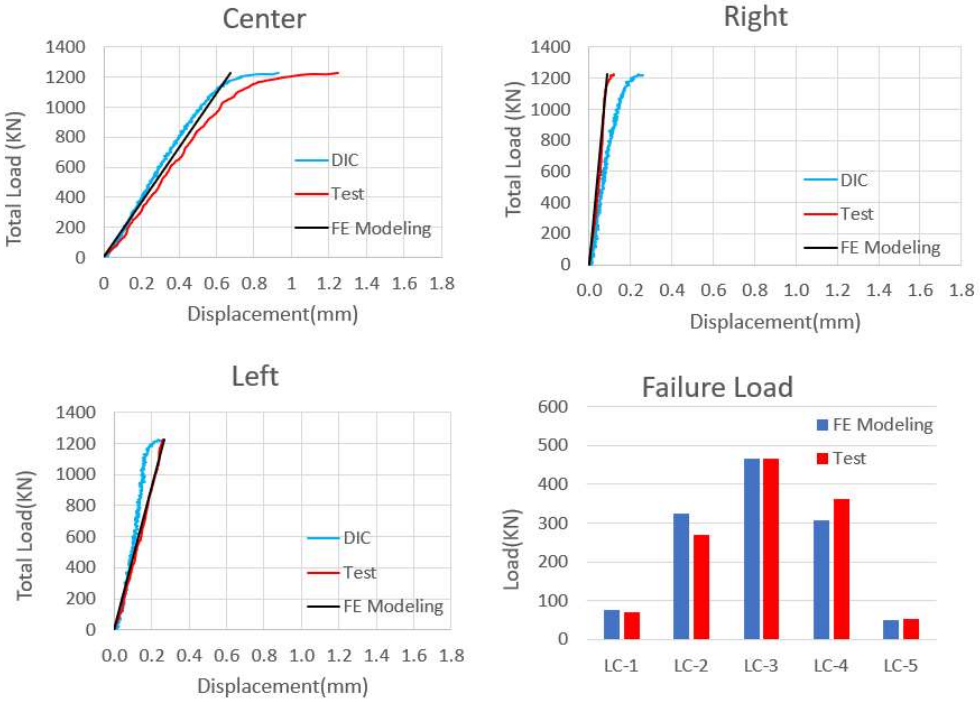

Appendix B.9. DIC, Test and FE modelling results and load distribution results for specimen C-1 until failure

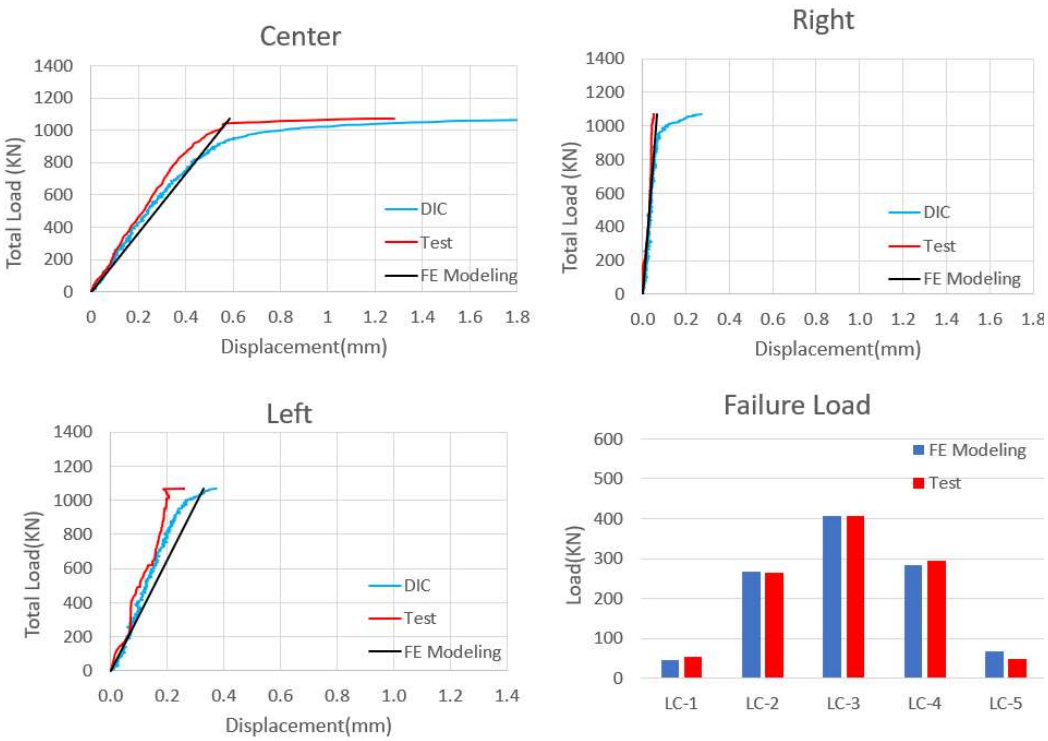

Appendix B.10. DIC, Test and FE modelling results and load distribution results for specimen C-2 until failure

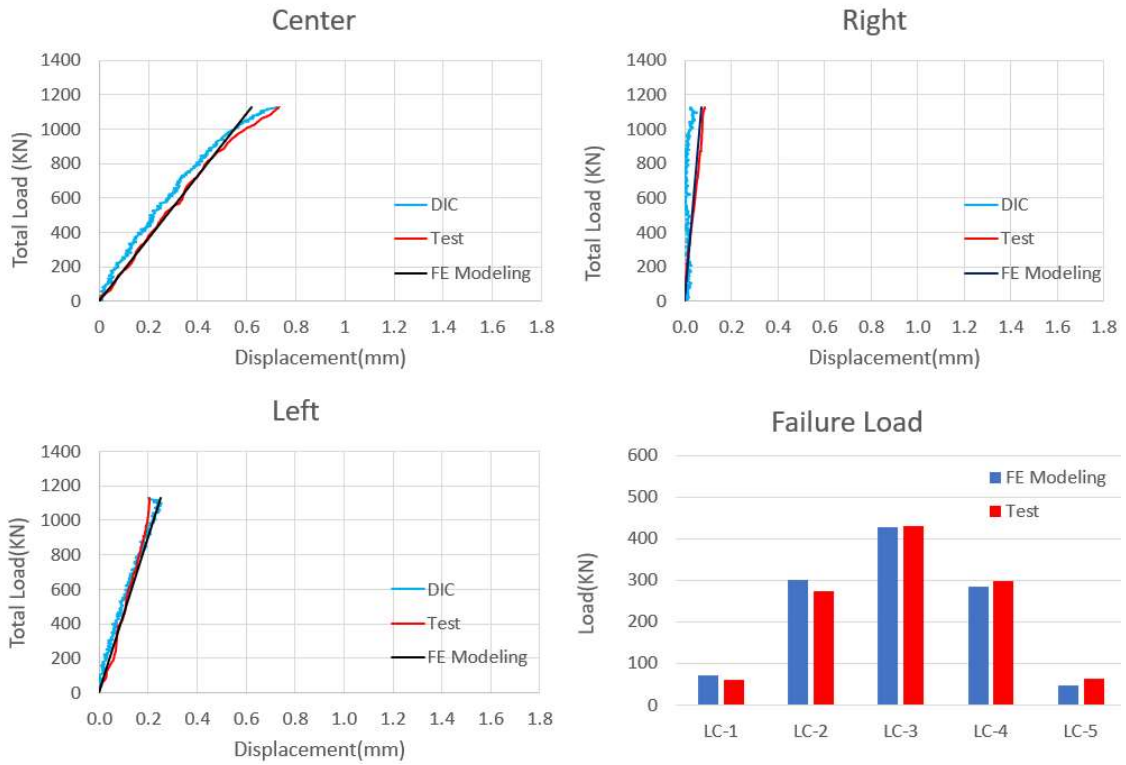

Appendix B.11. DIC, Test and FE modelling results and load distribution results for specimen C-3 until failure

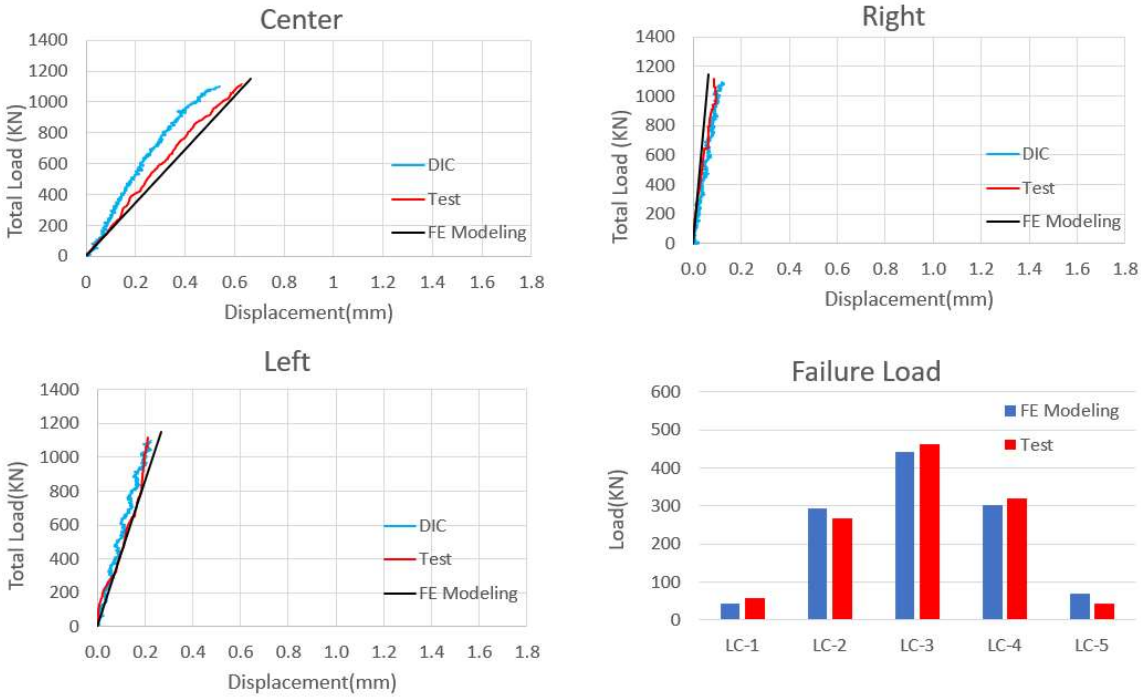

Appendix B.12. DIC, Test and FE modelling results and load distribution results for specimen C-4 until failure

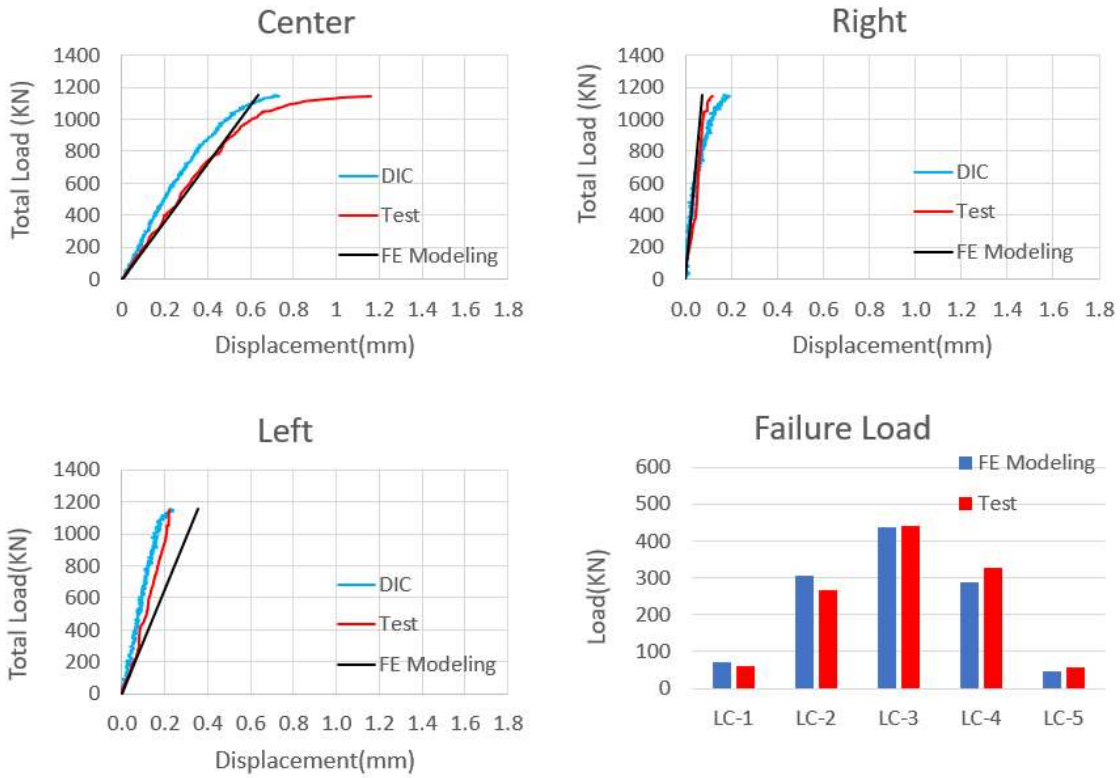

Appendix B.13. DIC, Test and FE modelling results and load distribution results for specimen C-5 until failure

Appendix C

This appendix comprises two examples that illustrate the application of the empirical equations developed in Chapter 5 for load spread angle and K-factors.

Example 1:

A 5-ply CLT wall made of grade 2 lumber subjected to an in-plane concentrated compression load parallel to the grain in the two load application scenarios, as illustrated in Figures C.1 and C.2. If the compression applied load is 500 kN, and the thickness of CLT is 175 mm with similar layer thicknesses, design CLT wall and determine the load-spread angle, the effective length, and maximum compression stress for designing supporting member or assembly.

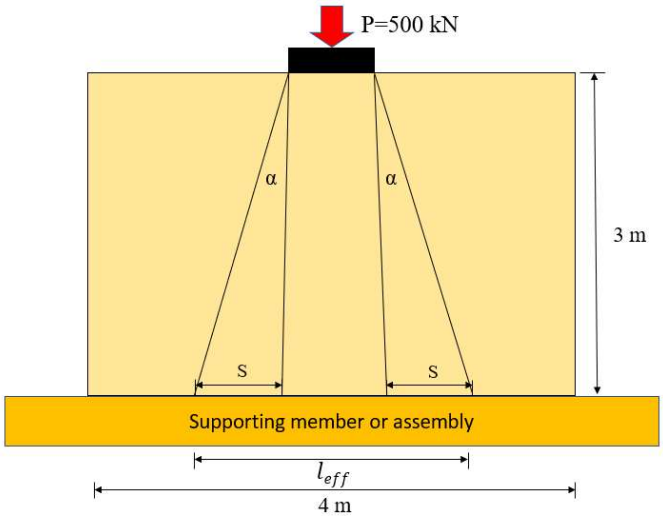

Appendix C.1. Load is applied in the middle of CLT

For designing CLT itself:

Laminate thickness: t =35mm, Laminate width: a= 800mm, Height: h =3000mm

Chracteristic compression strength: $f_C = 11.5$ N/mm^2

Duration factor: $K_D = 1$, System factor: $K_H = 1$, Service factor compression: $K_{SC} = 1$

Treatment factor: $K_T = 1$

Compression strength: $F_C = 11.5$ N/mm^2 > Max stress (under the loading area): 5.95 ok

Effective cross-section in compression: $A_{eff} = 84000$mm^2

Effective moment of inertia: $I_{eff} = 282974999$mm^4

Slenderness radius: $r_{eff} = 58.04$ mm, Slenderness ratio: $C_C = 14.92 \leq 43$ ok

Size factor compression: $K_{ZC} = 1.11 < 1.3$, use 1.11

MOE for compression design: E05 6500 N/mm^2 , Service factor for MOE: $K_{SE} = 1$

Slenderness factor: $K_C = 1$, Resistance factor: $\varphi = 1$

Compression resistance: $P_r = 1078$ kN > P_f

For designing supporting member or assembly:

$\frac{h}{w} = \frac{3}{4} = 0.75 \quad \frac{a}{w} = \frac{0.8}{4} = 0.2$

Assumption: 5-ply CLT with the following layout:

35-35-35-35-35 : $p = 0.4\,, b\ (parallel\ layers\ thickness) = 105mm$

From Equation (5.2): $\alpha = 9.55(\frac{h}{w})^{-0.03}(\frac{a}{w})^{-0.46}p^{0.22}$

α=16.4 ° $\longrightarrow \tan(\alpha) = \frac{S}{h} \longrightarrow S = 0.88m$

l_{eff}= a+2S = 0.8+2× 0.88 = 2.56 m

$k_1 = 1.34(\frac{h}{w})^{0.11}(\frac{a}{w})^{-0.16}p^{0.03}$

k_1 =1.63

$\frac{\sigma_{max}}{\sigma_{mean}} = k_1 \qquad \sigma_{max} = k_1 \frac{p}{bl_{eff}}$

$\sigma_{max} = 1.63\frac{500000}{105 \times 2560} \longrightarrow \sigma_{max} = 3.03$ N/mm^2

The max stress for designing the supporting member or assembly is 3.03 N/mm^2.

Example 2:

Determine the load-spread angle, the effective length, and maximum compression stress for designing supporting member or assembly if the load is located at the edge of CLT wall.

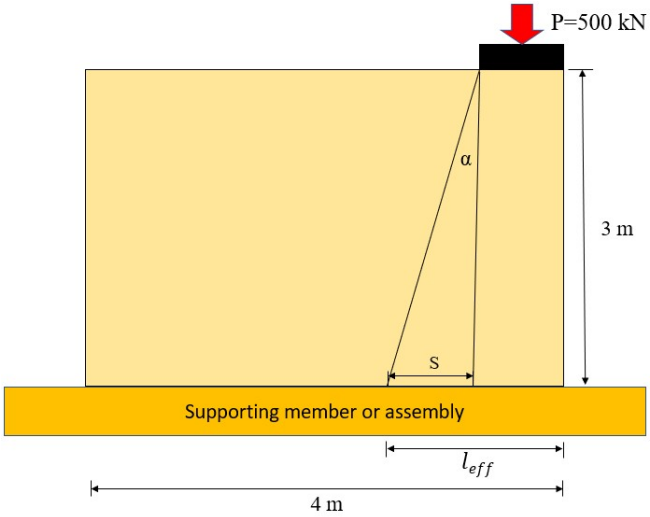

Appendix C.2. Load is applied at the edge of CLT

For designing supporting member or assembly:

$$\frac{h}{w} = \frac{3}{4} = 0.75 \qquad \frac{a}{w} = \frac{0.8}{4} = 0.2$$

Assumption: 5-ply CLT with the following layout:

35-35-35-35-35 : $p = 0.4\,, b\ (parallel\ layers\ thickness) = 105mm$

Grade V2 lumber: (CSA086-19-table 8.2) $f_c = 11.5\ Mpa$

From Equation (5.3): $\alpha = 21.09(\frac{h}{w})^{0.22}(\frac{a}{w})^{0.02}p^{0.28}$

α=14.8 ° $\longrightarrow$ $\tan(\alpha) = \frac{S}{h}$ $\longrightarrow$ $S = 0.78m$

l_{eff}= a+S = 0.8+0.78 = 1.58 m

$k_2 = 0.582(\frac{h}{w})^{0.23}(\frac{a}{w})^{-0.61}p^{0.06}$

k_2 =1.38

$$\frac{\sigma_{max}}{\sigma_{mean}} = k_2 \qquad \sigma_{max} = k_2\frac{p}{bl_{eff}}$$

$$\sigma_{max} = 1.38\frac{500000}{105 \times 1580} \qquad \sigma_{max} = 4.2\ \mathrm{N/mm2}$$

The max stress for designing the supporting member or assembly in this scenario is 4.2 N/mm^2.